ABSTRACT

Title of Dissertation / Thesis: MAGNETIC DOMAIN MEMORY CELL AND MAGNETORESISTIVE THIN FILMS

Li Gan, Ph. D., 2004

Dissertation / Thesis Directed By: Professor R. D. Gomez, Department of Electrical and Computer Engineering

A new generation of electronic devices that use the spin of the electron instead of its charge as a means to manipulate information has recently emerged. These so called “spintronic” devices exploit effects such as giant magneto-resistance (GMR) in magnetic thin-film heterostructures and are already commercialized in today’s high-density hard disk drives. Another potential major economic impact from the discovery of GMR is anticipated to come from nonvolatile magnetic random access memory (MRAM). The keys to next generation devices depend upon the enhancement of magneto-resistive sensitivity and stability of GMR structures, as well as the invention of novel methods to change the magnetizations of one or more ferromagnetic layers. In this dissertation, I have addressed both aspects by improving fabrication processes in various magneto-resistive thin films and developing a novel magnetic memory cell utilizing current pulse induced magnetization switch.

In the study of magnetic multilayer thin films, three advanced process issues have been addressed, these include: (i) the use of exchange coupling as a tool to estimate the critical thickness for the pinhole appearance in ultra-thin Cu films in GMR structures and Al_2O_3 barrier in tunneling magneto-resistance (TMR) structures; (ii) the role of aluminum oxides and metals as barriers against thermal oxidation of ferromagnetic metals in air; (iii) assessments of ballistic magneto-resistance (BMR) effects into practical devices by using electrochemical deposition to fabricate nanometer size contacts in both thin film and wire geometries. In the study of current pulse induced magnetization switch for MRAM, we have demonstrated domain wall motion in patterned ferromagnetic films for the first time and developed selective bi-stable domain configurations controlled by current pulses. Based on these discoveries, we built and successfully implemented a one-byte memory cell, which has far simpler structure than conventional MRAM.

MAGNETIC DOMAIN MEMORY CELL AND MAGNETORESISTIVE THIN FILMS

By

Li Gan

Dissertation submitted to the Faculty of the Graduate School of the
University of Maryland, College Park, in partial fulfillment
of the requirements for the degree of
Doctor of Philosophy
2004

Advisory Committee:
Professor R. D. Gomez, Chair and Advisor
Professor J. Goldhar
Professor A. Iliadis
Professor R. Newcomb
Professor L. G. Salamanca-Riba

Dedication

To Mom and Dad,

who offered me unconditional love

and support throughout my life.

To My wife

any accomplishments of mine are impossible

without your encouragement and sacrifice.

Acknowledgement

It is with utmost sincerity that I express my gratitude to all of those who have supported me throughout my degree commitments. First and foremost, I would like to thank my advisor Prof. Romel Gomez, you have been a great mentor and a great friend. I could not have found someone better for getting me through the graduate experience, both inspiring and guiding me throughout my thesis work. I would also like to thank Dr. William Egelhoff Jr., for giving me the opportunity of working with you at NIST and accomplishing a great amount of my thesis research there. This unique experience also greatly expanded my knowledge and skills for further career development. And last but not least, I would like to thank my colleagues both in University of Maryland and at NIST, Dr. Michael Dreyer, Dr. Hyuncheol Koo, Dr. Seok-Hwan Chung, Herman Pandana, Sylvia Florez, Peijie Chen, and Dr. Erik Svedberg. To each of the above, I like to extend my deepest appreciation.

List of Tables

List of Figures

Table of Contents

Chapter 1: Introduction

1.1 Introduction

Advances in magnetic technology have been more profound in the last ten years than in any other point in the history. This fact is readily obvious for any computer user who has seen the capacity of hard disk drives swell from 10 MB to 100 GB since the early nineties [1]. Magnetics is also rapidly entering the world of solid state memory and magnetic random access memories (MRAMs) are being developed for niche applications such as satellite communications and mobile computing applications [2, 3]. Much of this progress can be attributed to the advances in fabrication technology and the understanding of magnetism at nanometer scales.

Pushing the envelop towards the next generation magnetic sensing and MRAM hinge on the developing of sensors with very high signal to noise ratios and efficient ways to alter magnetic states. A key parameter is sensitivity, which is defined as the resistance change with presence of a magnetic field. A breakthrough occurred with the discovery of so called “giant magnetoresistance” (GMR) in 1988 in multi-layers of ferromagnetic/noble metal/ferromagnetic films [4], as well as the observation of enhanced MR sensitivity in magnetic tunnel junctions (MTJ) comprised ferromagnetic/insulator/ferromagnetic layers [5]. These effects produce MR in range of 15-30%, which is one order of magnitude higher than the traditional anisotropic MR (AMR) in continuous films. From a technical point of view, the challenges are related to the quality of the nonmagnetic/magnetic interfaces and the optimization of the thickness that are devoid detrimental effects due to imperfection.

In MRAM implementation, a crucial step is to develop new ways of changing the magnetization direction of one or more of the active electrodes. The conventional approach that generates a magnetic "write" field from an external wire is dated despite its widespread use in the industry. A drawback is the difficulty in localizing the field to switch one component and not its neighbor.

This thesis is focused on solving some of the most important issues related to magnetic device development. In the area of magnetic sensing for storage applications, I will address the interfacial issues related to the minimization of barrier layers in GMR and TMR devices as well as develop methods for producing ballistic magnetoresistive effect in planar geometry. In the area of magnetic random access memory, I have implemented Prof. Gomez' idea of local magnetization switching without using external fields but rather relying on domain wall motion induced by spin-polarized currents. Finally, I have fabricated a novel MRAM cell based upon current induced magnetization switching and demonstrated its efficacy in a one-byte prototype.

The main contributions of my work are listed below, including my publications on each topic:

1. By measuring exchange coupling, we determined the critical thickness for the pinhole appearance in spacer of GMR and barrier in TMR. "Detection of Pinholes in Ultra-thin Films by Magnetic Coupling", Material Research Society Symposium Proceedings, Vol. 674, 2001.
2. Established the role of aluminum oxides and metals as barriers against thermal oxidation of ferromagnetic metals in air. "Thin Al, Au, Cu, Fe, Ni and Ta Thin Films as Oxidation Barriers for

Co in Air", Journal of Applied Physics, 8731 (93), 2003. "Ultra-thin Aluminum Oxide as a Thermal Oxidation Barrier on Metal Films", Thin Solid Films, 219 (415), 2002.

3. Assessed ballistic magneto-resistance effects in planar geometry. "Magnetoresistance of Ferromagnetic Point Junctions from Tunneling to Direct Contact Regimes", IEEE Trans. on Magnetics, 2004, in press. "Artifacts in Ballistic Magnetoresistance Measurements", Journal of Applied Physics, 2004, in press. "Resistance Changes Similar to Ballistic Magnetoresistance in Electrodeposited Nanocontacts", Applied Physics Letters, 236 (84-2), 2004. "Ballistic Magnetoresistance in a Nanocontact between Ni Cluster and a Magnetic Thin Film", Applied Physics Letters, 79 (18), 2001.

4. Demonstrated, for first time, domain wall motion in patterned film by using current pulse. "Current-Pulse-Induced Domain Wall Motion Observed by MFM", IEEE Trans. on Magnetics, 36 (5), 2000.

5. Developed a new MRAM cell using current induced bi-stable domain configurations and domain wall resistance. "Logic State Reading of a NiFe Magnetic Memory Cell Using Domain Wall Resistance", in preparation.

6. Optimized various thin film processing. "Coercivities above 10 kOe in CoPd Superlattices", Journal of Applied Physics, 2004, in press. "Co Layer Thickness Dependence of Exchange Biasing of IrMn/Co and FeMn/Co", Journal of Applied Physics, 6611

(93), 2003. “Magnetoresistance Magnetometry of $(Ni_{80}Fe_{20})_{1-x}Ir_x$ Wire with Varying Anisotropic Magnetoresistance Ratio”, Journal of Applied Physics, 8104 (93), 2003. “Intermixing of Aluminum-Magnetic Transition-Metal Bilayers”, Journal of Applied Physics, 93 (10), 2003. “Anomalously Large Intermixing in Aluminum-Transition-Metal Bilayers”, Phys. Rev. B, 104427 (66), 2002. “Superconformal Electrodeposition of Silver Ballistic Magnetoresistance like Artifacts in Electrodeposited Nanocontacts in Sub-micron Meter Features”, Journal of The Electrochemical Society, 149 (8), 2002. “Feature of Domain Nucleation and Growth in Co/Cu/Co Synthetic Antiferromagnets Deposited on Obliquely Sputtered Ta Underlayers”, Journal of Magnetism and Magnetic Materials, 240 (70), 2002. “Effect of Argon Gas-Cluster Ion Beam Etching on Surface Roughness, Crystallinity, and GMR Performance of a-Fe_2O_3 Bottom Spin valve”, MMM Conference 2001.

This thesis is organized as follows. In Chapter 1, I will provide a review of the state of the art in GMR, TMR and BMR devices. Chapter 2 discusses my contributions in the area of magnetoresistive devices as well as protection layers against oxidation induced device degradation. In Chapter 3, I will discuss the implementation and design of a new memory cell. Finally, Chapter 4 will provide an overall summary of the results and discuss the future directions based on this work. The Appendix discusses some of the important thin film fabrication and

characterization techniques and a flowchart of 8-bit memory cell Visual Basic control code.

1.2 Phenomenological models of magnetoresistance

Magnetoresistance, defined as the change of resistivity as a function of magnetic field or magnetic state, is a well-known phenomenon, and can be expressed generically as $\Delta\rho/\rho$, where $\Delta\rho$ is the resistivity change under the magnetic field. Giant magnetoresistance (GMR) effect was first reported in Fe/Cr/Fe multilayers by Baibich [4], which demonstrated over ten times the magnetoresistance values in GMR than anisotropic magnetoresistance (AMR). AMR is due to the difference in resistivity with current flowing parallel and perpendicular to the magnetization. Another major advance was the successful fabrication of magnetic tunneling junction (MTJ) by Moodera [5] in 1995, where over 10% value of tunneling magnetoresistance (TMR) was observed when current flowed from one ferromagnetic layer across an insulating barrier to another ferromagnetic layer. In contrast to the conventional AMR in homogeneous ferromagnetic metals, GMR is present only in heterogeneous multi-layer magnetic systems and arises due to interface scattering of the spin current. Recently, in 1999 magnetoresistance over 200% was experimentally discovered by Garcia et al. in Ni-Ni wires joined by a nanocontact [6]. In this case the electrons are believed to transverse the junction without loss of spin polarization and no scattering, the effect is labeled as “ballistic magnetoresistance”.

1.2.1 Giant magnetoresistance

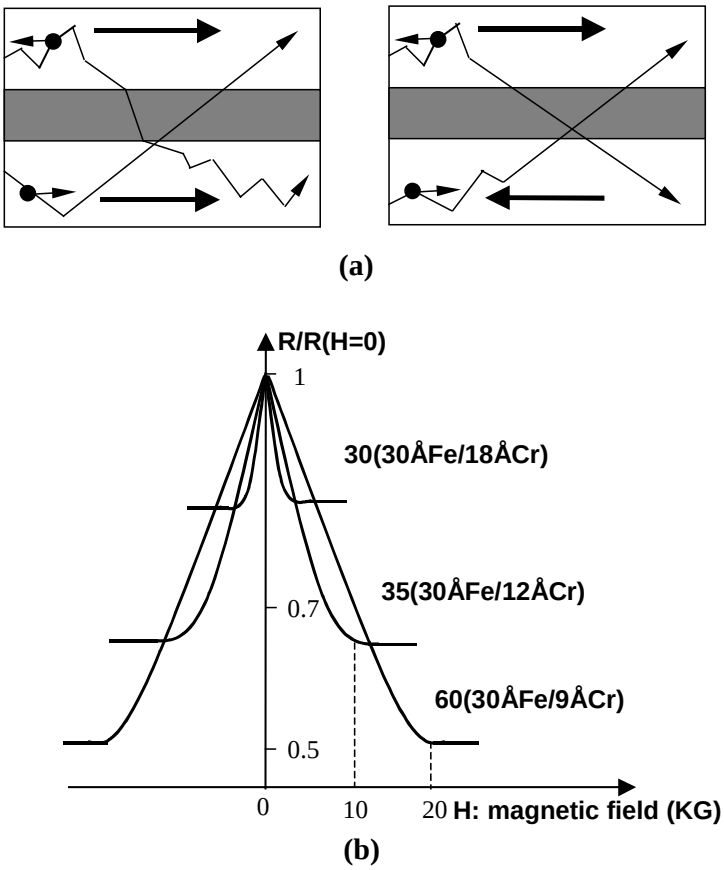

Figure 1 (a) A schematic drawing of the current-in-plane (CIP) GMR effect in two magnetic layers separated by a nonmagnetic spacer layer with parallel and antiparallel magnetizations. (b) The first observed GMR effect in Fe/Cr super lattice structure.

The origin of GMR effect lies in the spin dependent transmission of conduction electron between the magnetic layers through nonmagnetic space layer and depends on the relative orientation of the magnetic moments of the magnetic layers. This is so called “spin valve effect”. In ferromagnetic transition metals, the electrons are distinguished according to the projection of their spins along local magnetization: spin up or spin down electrons, which are parallel or antiparallel to

the local magnetization, respectively. These two types of electron have quite different scattering rates because of the difference in density of empty states at the Fermi level. Generally an electron will have a higher scattering rate when its spin direction is opposite to local magnetization. Consider the Fe/Cr/Fe structure in Fig. 1(a) and assume that the mean free paths of the electrons are much longer than the thickness of the multi-layers. Define R_1 and R_2 as the resistivity of the spin up and spin down electrons. If the magnetizations of both Fe layers are parallel (FM1//FM2) (resulting from an applied field), then resistivity of this multilayer system can be estimated as:

$$R_p = R_1 R_2 / (R_1 + R_2) \qquad (1\text{-}1)$$

Further assuming that an antiferromagnetic (AFM) RKKY-like interaction exists at zero field at the given Cr thickness, then the magnetizations of the two Fe layers will be antiparallel, and the resistivity of this system then becomes

$$R_{ap} = (R_1 + R_2)/4 \qquad (1\text{-}2)$$

The GMR value is therefore given by [14]:

$$\Delta R / R_p = (R_{ap} - R_p) / R_p = (R_1 - R_2)^2 / 4R_1 R_2 \qquad (1\text{-}3)$$

Note $R_p < R_{ap}$ so that $\Delta R / R_p$ can have a value of >100%. An alternative definition is $MR = \frac{\Delta R}{R_{ap}}$. The alignment of the multi-layer is a function of the applied field so that $\Delta R = \Delta R(H)$.

To date, there are three categories of GMR structures that have been invented: AFM coupled multilayers, multilayers with different FM layer, and exchange-biased spin valves. Antiferromagnetic (AFM) coupled multilayers structures have the form B/n*(F/S)/C, where B and C refer to buffer and cap layer, F is a transition ferromagnetic metal layer (Fe, Co, Ni and their alloys), and S is a

space layer (non-ferromagnetic transition metal or noble metal Cr, Cu, Ag, Au, Ru, etc.). At zero field the neighboring ferromagnetic layers display a spontaneous antiparallel magnetization alignment, arising from antiferromagnetic interlayer exchange coupling. The problem in maintaining antiferromagnetic coupling is the spacer layer, which has to be 1 to 20 mono-layers thick, is susceptible to pinhole formation, causing direct ferromagnetic coupling. This major technological challenge was addressed in 1986 when deposition techniques had improved to be capable of producing high quality thin films [1]. GMR of over 25% and 70% have been observed for Fe/Cr and Co/Cu respectively, with corresponding saturation fields of 25kOe and 10kOe at room temperature. The resistance of this type of structure is shown in Fig. 1b. At 4.2K the GMR values increase to over 100% [7]. These high GMR values partly result from good interface crystallographic matching between the ferromagnetic layers, or "super lattice structure." In magnetic recording, large changes in resistance are required at low fields of 5 Oe to 10 Oe, which means AFM multilayers are at a disadvantage for this application because the required saturation fields are too high. An alternative technique which yields similar MR value at lower field has been accomplished using the so-called "pseudo spin valve" structures. These are formed by using two ferromagnetic materials with different coercivities and without antiferromagnetic coupling, which can be used to produce a change in the relative orientation of the magnetization in the successive ferromagnetic layers. One example is NiFe/Cu/Co. At a very low field, the low coercivity layer (NiFe) rotates. At higher field, the high coervicity layer (Co) rotates. The magnetization changes from parallel to antiparallel at the low field, thus the field required to obtain full GMR amplitude are much lower than in antiferromagnetic-coupled layers. The field is

on the order of the coercivity of the softer ferromagnetic material, which is only a few or tens of Oe. Another important structure is the exchange-biased spin valve (EBS). It consists of a ferromagnetic layer (F) in contact with an antiferromagnetic layer (AF). A unidirectional anisotropy along the field direction is established in the ferromagnetic layer either by cooling in a field through Neel temperature of the antiferromagnet, or by depositing in an external field. This results in a shift of the magnetization loop of the ferromagnet, where the field is applied along the anisotropy axis. This method is known as “exchange biasing” and it determines the relative orientation of the magnetization of two ferromagnetic layers used in GMR structures. The basic structure of EBS is substrate/AF/F/S/F. The space layer must be thick enough to magnetically separate the two ferromagnetic layers. When the applied field is along the anisotropy axis and is lower than the exchange bias field, only the uncoupled layer (free layer) changes its magnetization direction. When the field is increased to exceed the bias field, the biased layer (pinned layer) also reverses its magnetization. Hence, the relative magnetization orientation of the two ferromagnetic layers changes from parallel to antiparallel then back to parallel when the fields are swept from positive to negative saturation.

An MR versus field curve for a typical exchange-biased spin valve prepared in our lab is shown in Fig. 2, which was obtained from the stack structure in Fig. 3. From the data, we can extract the coercivities of two ferromagnetic layers, the coupling between two ferromagnetic layers, and the exchange bias field.

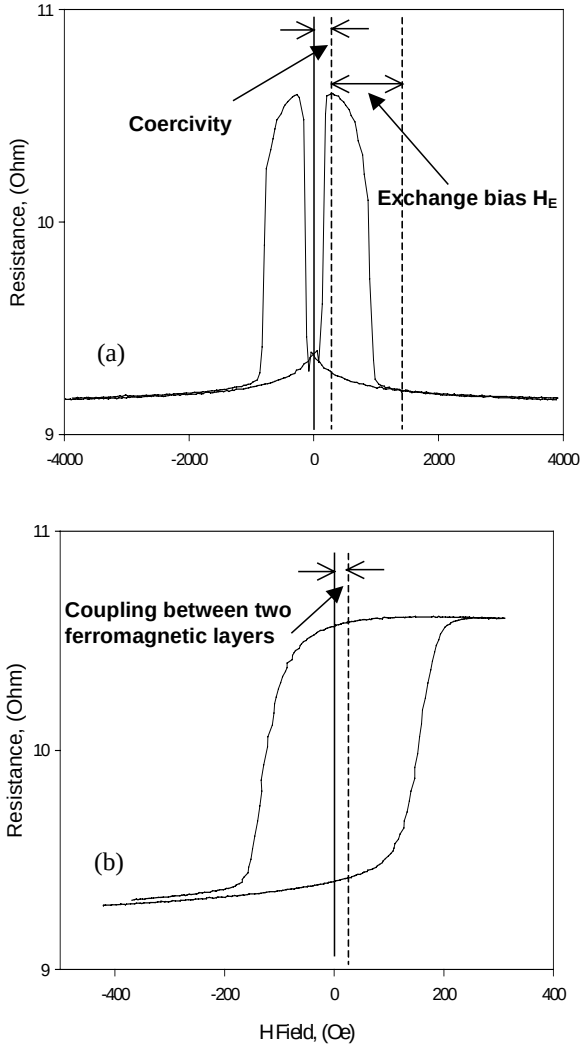

Figure 2 Plots of GMR loops of an exchange biased spin-valve (EBS) with (a) high magnetic field sweep and (b) low magnetic field sweep.

3 nm Co
2 nm Cu
2.5 nm Co
NiO substrate

Figure 3 The stack structure of a bottom spin valve with transfer curves shown in Fig. 2.

1.2.2 Tunneling magnetoresistance

Tunneling magnetoresistance occurs when current flows from one ferromagnetic layer across an insulting barrier to another ferromagnetic layer in a tunnel junction. Like the GMR effect, a considerable change in resistance is observed when relative orientation of the two magnetic layers changes from antiparallel to parallel. Because of the difficulty of making pinhole free insulating barrier layers of only a few monolayers thick, it was only in 1995 that first reproducible magnetic tunnel junction (MTJ) was published [5].

The origin of the TMR effect lies in the spin dependent tunneling probability of electrons from one magnetic electrode across the insulating layer to the other electrode. This is shown schematically in Fig. 4(a). The tunneling probability of the electrons depends on the density of states of spin up and spin down electrons (N_1 and N_2) for both electrodes (F_1 and F_2) at Fermi level. Fig. 4(b) shows the approximate spin up and spin down band structures for parallel and antiparallel magnetizations. The Fermi levels of the bottom and top electrodes are slightly shifted due to the application of a voltage V, which gives rise to a tunneling current from F_1 to F_2. It is assumed that the spin of electron is conserved during tunneling. In case of parallel magnetization the total current is:

$$I_p \propto N_1 N_1 + N_2 N_2 \qquad (1\text{-}3)$$

In case of antiparallel magnetizations the total current is expressed as:

$$I_{ap} \propto N_1 N_2 + N_2 N_1 \qquad (1\text{-}4)$$

For magnetic materials with $N_1 \neq N_2$, the parallel case will produce higher current than in the antiparallel case. The tunneling magnetoresistance is defined as: $TMR = (I_p - I_{ap}) \Big/ I_{ap} = \dfrac{2p_1 p_2}{1 - 2p_1 p_2}$ (1-5)

where p_i is the polarization $\left(\frac{N_1 - N_2}{N_1 + N_2}\right)$ of F_i. This expression is known as Julliere model [8].

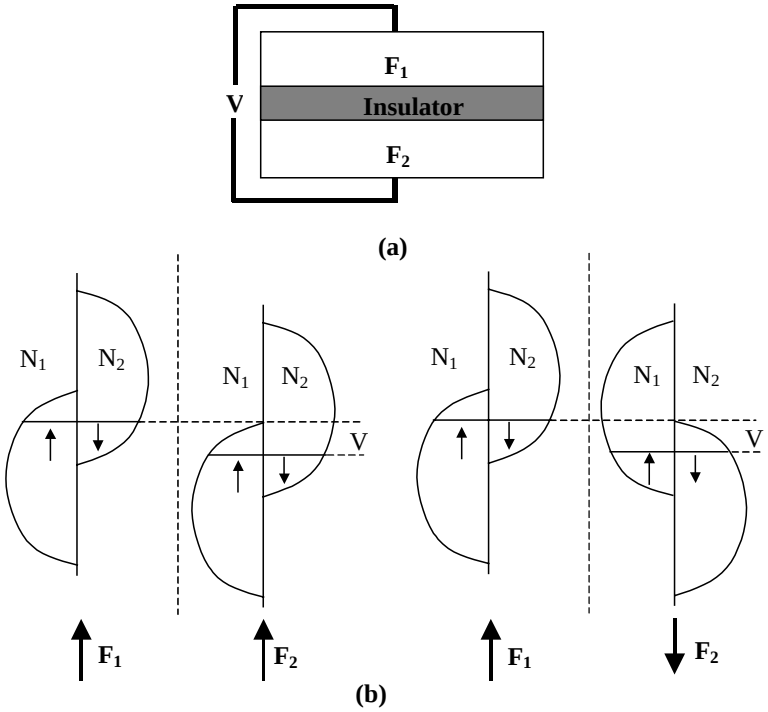

Figure 4. (a) Schematic drawing of a MTJ in which electrons tunnel from one ferromagnetic electrode F1 to another F2 across an insulating barrier. (b) Density of states of both electrodes for parallel and antiparallel magnetizations respectively.

This model is somewhat simplified, as the barrier material also plays a role in both the magnitude and sign of this phenomenon [9]. However, this simple two-band model is sufficient for understanding the MR of the AlOx-based junctions considered here. The most critical layer in the MTJ stack is the AlOx tunnel barrier. The tunnel barrier is very thin, ≤ 20 Å, and the tunneling resistance is exponentially dependent on its thickness. In addition to being free of pinholes and very smooth, it must be extremely uniform over the wafer, since small variations

in the AlOx thickness result in large variations in the resistance. Because the conduction path is perpendicular to the layers, the device resistance scales as the inverse of the in-plane area, and its Resistance-Area (RA) product characterizes the barrier. For a submicron meter patterned MTJ device suitable for application as a magnetic recording reader or in MRAM, MR values above 20% and RA in the 1-100 $\Omega\mu m^2$ range are desired. These values have been obtained by optimizing aluminum thickness and oxidation time [10].

The layers of the MTJ stack are formed by sputter-deposition techniques with deposition rates in the Angstrom-per-second range. The best methods for producing the insulating tunnel barrier are not yet clear, but various techniques are currently under study throughout the world. The best results to date are for AlOx tunnel-barrier layers made by depositing a metallic aluminum layer, between 5 Å and 15 Å thick, and then oxidizing it by one of several methods [11]: plasma oxidation, oxidation in air ("natural oxidation"), ion-beam oxidation, oxidation by glow-discharge plasma, atomic-oxygen exposure, and ultraviolet-stimulated O_2 exposure. Fabricating MTJ with good resistance uniformity over an entire wafer is challenging. However, with excellent aluminum thickness uniformity, RA uniformity of 10% 1-sigma over a 150 mm wafer can be routinely obtained.

1.2.3 Ballistic magnetoresistance

A particularly intriguing MR effect arises when the spin electrons are made to flow through a 1D-like channels formed by introducing atomic size constrictions as barriers. Recently, an MR value > 200% has been achieved in Ni-Ni and Co-Co nanocontacts in room temperature [6]. In the nanocontacts the electron mean free path is assumed to be longer than the size of nanocontact size

The regime of electron transport is considered ballistic, thus the MR names "Ballistic Magnetoresistance" (BMR).

The BMR can be explained in terms of domain wall scattering [12]:

$$BMR = \frac{\pi^2}{4}\frac{\zeta^2}{1-\zeta^2}F(\zeta,\lambda) \qquad (1\text{-}6)$$

where $\zeta = (D_1 / D_2 - 1)/(D_1 D_2 + 1)$ represents the spin polarization. The function F describes the non-conservation spin and is dependent on ζ and λ (the domain width). Larger BMR effect is achieved with higher D_1 / D_2 ratio (density of states condition) and smaller λ / l (ballistic condition), where l is the mean free path.

In a nano-constriction, the electron transport mechanism can be explained by a simple 1-dimensional quantum mechanical model. For one atomic transport channel, this model gives one resistance quantum

$$R_0 = G_0^{-1} = \left(\frac{2e^2}{h}\right)^{-1} = 12.9k\Omega \qquad (1\text{-}7)$$

where G_0 is one conductance quantum.

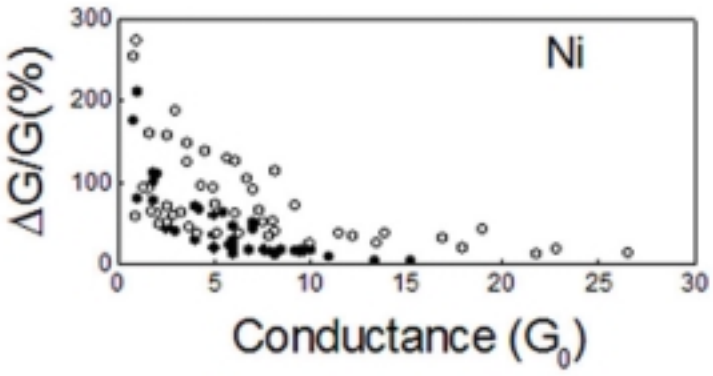

Figure 5 presents the experimental values in form of plots of magnetic conductance versus the nanocontact conductance for Ni-Ni nanocontacts [13].

Chapter 2: Multi-layer magnetic thin films

2.1 Exchange coupling effects and detection of pinholes in ultra-thin films by magnetic coupling

2.1.1 Background on exchange coupling

An important issue in GMR is the exchange coupling which was first discovered by Meiklejohn and Bean in ferromagentic-antiferromagnetic Co-CoO powder compacts [14]. Exchange coupling or biasing manifests itself as a unidirectional anisotropy rather than uniaxial anisotropy in the magnetic layer. The simplest EB system is comprised of an antiferromagnet in atomic contact with a ferromagnet grown in an external field as it is cooled below the Neel temperature. The center of magnetic hysteresis loop of the system will shift from zero to H_{EX}, and this is referred to as exchange biasing (EB) field. The applications of EB have been developed recently when Dieny proposed the exchange-biased spin-valve structure [15], which led IBM to market the first high-density hard disk drive (5 Gb/in^2) using spin valve read heads [1].

The exact mechanism for exchange bias in real systems is quite complicated because the dynamics of interface spins involves several competing interactions and highly dependent upon the atomic arrangement and morphology in the vicinity of the interface. The early models [16] have in common the assumption of collinear magnetic structures on the F and AF sides of the interface (Fig. 6(a), (b)). The energy can be expressed as:

$$E = -HMt_f \cos\theta - J\cos\theta + K_f \sin^2\theta \qquad (2\text{-}1)$$

where H is the applied field, M is the saturation magnetization of ferromagnetic film, J is interlayer exchange between ferromagnet and antiferromagnet, and θ is the angel between M and uniaxial anisotropy easy axis. A stable configuration is achieved when θ=0 and π, and the coercive fields are $H_{c1} = -\dfrac{2K_f + J}{Mt_f}$ and $H_{c2} = \dfrac{2K_f - J}{Mt_f}$. Because $H_{c1} \neq H_{c2}$, the hysteresis is biased and the exchange coupling is given by

$$H_{EX} = \frac{J}{Mt_f} \qquad (2\text{-}2)$$

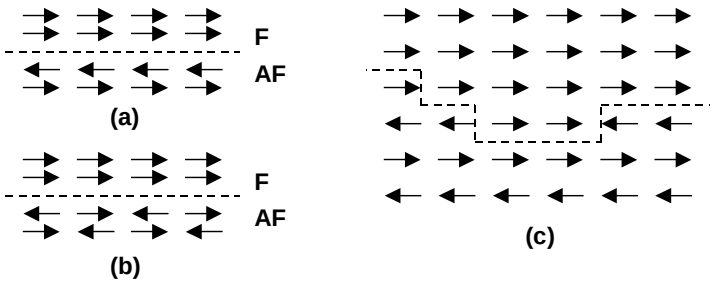

Figure 6 Magnetic collinear interface configurations. The dashed line marks the boundary between the F and the AF. (a) Fully compensated interface. (b) Uncompensated interface. (c) Rough interface.

This term (Eqn. 2-2) is considered as a unidirectional anisotropy. However, the predicted value of exchange bias from this model is much larger than observed experimentally.

Observing that the energy minimization of a long chain of magnetic moments favors some type of twist configuration more than a uniform configuration, Neel

derived the magnetization profiles at the interface that develop domains both in F and AF layers [17]. A random interface model [18] based on the assumption of random rough F/AF interface (Fig. 6(c)) and Neel's results gave the expression of exchange bias as:

$$H_{EX} = \frac{J}{Mt_f \sqrt{1+\left(\frac{J}{2\sigma}\right)^2}} \qquad (2\text{-}3)$$

where σ is the domain wall energy. This is essentially Eq. (2-2) with the addition of $\frac{J}{\sigma}$ term, giving a reasonable estimate for exchange bias.

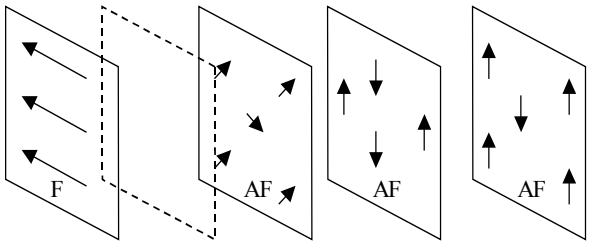

Figure 7 Illustration of the perpendicular F and AF magnetic interface configuration with spin canting in the first AF layer. Dashed line marks the boundary.

Recent micromagnetic calculations by Koon [19] showed that at the F/AF interface, F moments are perpendicular to AF easy axis direction and the AF interface layer moments exhibit canting (Fig. 7). It is now apparent that in idealized systems, a combination of random interface and orthogonal magnetic arrangement provides a more realistic model [20]. Furthermore, because of the complexity of interface crystallography and magnetic structure even in an ideal system, several other models

based on additional assumptions have been proposed to explain some other experimental results such as the “Frozen interface model” and “Local pinning field and domains” [21].

In real films, various exchange coupling interactions including direct effects such as exchange anisotropy and indirect effects like magnetostatic coupling could simultaneously make contributions to magnetic properties. Apart from exchange anisotropy (coupling between the antiferromagnetic layer and the pinned ferromagnetic layer), coupling between free and pinned layers of spin valve may arise due to:

Oscillatory exchange coupling

Stray field/demagnetization coupling

Neel “orange peel” coupling

Magnetostatic coupling due to domain walls

Pinhole coupling

Oscillatory exchange coupling is an interlayer coupling (either positive or negative) of ferromagnetic layers separated by nonmagnetic layers. The sign oscillates as a function of the thickness of the nonmagnetic layer and the oscillation period is normally around 1 to 2 nm. This has consequences on the GMR effect in the geometry shown in Fig. 8.

This effect was first reported by Parkin et al. [22], which showed that the strength of GMR in a Co/Cu superlattice oscillates as a function of Cu spacer thickness. Since no GMR effect is expected when the adjacent ferromagnetic layer are positively coupled, the minimum in GMR versus Cu spacer thickness

corresponded to the ferromagnetic coupled state of the multilayers. In contrast, the maximum correspond to the antiferromagnetic-coupled state for those given Cu thicknesses. As the thickness of the spacer is varied, the report points out that the magnetization vector in adjacent ferromagnetic layers switch between parallel and antiparallel configurations. This oscillatory coupling was suggested to be similar in characteristics to the Ruderman-Kittel-Kasuya-Yosida (RKKY) type exchange oscillations that are generally observed as a function of distance between two magnetic ions that are embedded in a non-magnetic metallic medium. However, the oscillation period is much larger than in RKKY. It is believed that RKKY oscillation is consistent with models including space quantization of the electrons in the nonmagnetic spacer layer, though the precise nature of these oscillations remains unclear. The energy of an oscillatory exchange coupling could be expressed as a sine wave function:

$$J = \frac{J_0}{t_{Cu}^2}\sin(\frac{2\pi t_{Cu}}{\Lambda} + \varphi) \qquad (2\text{-}4)$$

where Λ and φ are the wavelength and phase of the coupling, which are dependent on the crystal orientation. This model assumes perfectly smooth interfaces and attributes the coupling to the overlap of atomic orbits between the ferromagnetic layers. From this equation, the exchange coupling strength could be calculated as:

$$H_E = J/(\mu_0 M_S t) \qquad (2\text{-}5)$$

where H_E is the coupling strength, and M_S and $\boldsymbol{t}$ are the magnetization and thickness of ferromagnetic layer respectively. It is clear that the strength of coupling decreases sharply with increase of spacer thickness.

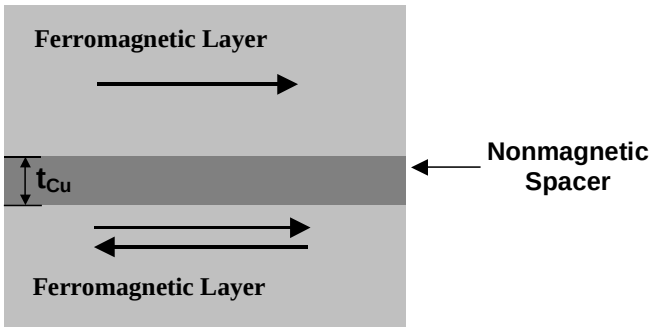

Figure 8 A schematic of GMR structure with two ferromagnetic layers separated by a nonmagnetic spacer with thickness of t_{Cu}.

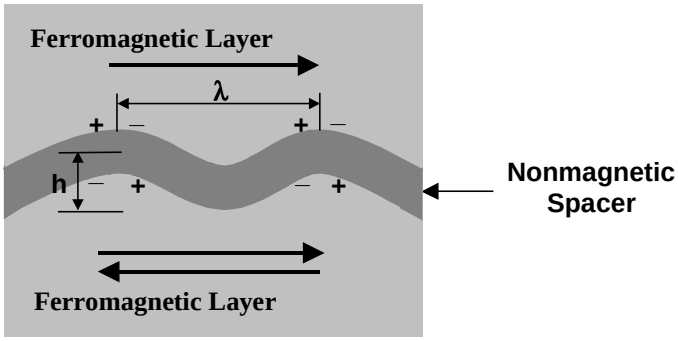

Figure 9 A schematic a GMR structure with correlated interface between ferromagnetic layers and nonmagnetic spacer.

The Neel model can also describe the magnetostatic coupling caused by correlated oscillations of the magnetic layers in non-ideal films ("orange-peel" coupling, or topological coupling). These oscillations originate from the topographical roughness of the films. If the interface between the ferromagnetic layer and nonmagnetic spacer has correlated roughness, dipoles are set up across the nonmagnetic layer. Fig. 9 shows a schematic of such as orange-peel coupling. Each pair of protrusions introduces an extra energy term that tends to align the

magnetization in the two ferromagnetic layers. Neel further showed that if the correlated roughness has in-plane anisotropy, then the coupled energy between two adjacent ferromagnetic layers could be expressed as:

$$J = \frac{\pi^2}{\sqrt{2}} \cdot \frac{h^2}{\lambda} \cdot (\mu_0 MM') \exp(\frac{-2\pi\sqrt{2}t_{Cu}}{\lambda}) \qquad (2\text{-}6)$$

where t_{Cu} is the Cu spacer thickness, M and M' are the saturation magnetizations of the two ferromagnetic layers, h is the interface amplitude, and λ is the interface wavelength. From the Eq. (2-6), the exchange coupling is given by [23]:

$$H_E = \frac{\pi^2}{\sqrt{2}} \cdot \frac{h^2}{\lambda t} \cdot M \exp(\frac{-2\pi\sqrt{2}t_{Cu}}{\lambda}) \qquad (2\text{-}7)$$

where t is the thickness of magnetic layer. The "orange peel coupling" strength is mainly determined by the amplitude h and wavelength λ of the correlated interface. It increases quickly as a function of the square of amplitude, while it saturates when t_{Cu}/λ is equal to a critical value.

Ideally, the free layer and pinned layer are magnetically decoupled. However in practice some residual coupling exists between them. Both RKKY model and Neel model can be used to describe the mechanism. The respective strength or contribution of the two models depends on the configurations of the spin valves and their microstructures.

2.1.2 Effect of pinhole coupling and pinhole detection by using low field MR curve

Pinhole coupling is the caused by discontinuities in the nonmagnetic layer. The ferromagnetic bridge connecting the two magnetic layers could be shown

schematically in Fig. 10. The coupling energy associated with pinholes is positive in nature, so that it tends to align the magnetization in two ferromagnetic layers in the same direction. The "free" layer becomes partially pinned by this coupling mode, which might decrease, even annihilate the GMR effect. In a typical NiO-Co-Cu-Co bottom spin valve, the Cu spacer thickness is normally around 2 nm. At an extreme case, the two Co interfaces are assumed to be sine waves with opposite signs of amplitude, and at 0.7 nm mean roughness probability for pinholes are raised. The lattice constant of Co (111) is 0.204 nm, the roughness which is required for pinhole formation is thus only 3 to 5 monolayers. Most importantly, a microscopically very small number of pinholes, each with a very small cross-section area, may build up into a macroscopically, very large, positive coupling, which could eliminated the ability of the free layer to switch with respect to the pinned layer.

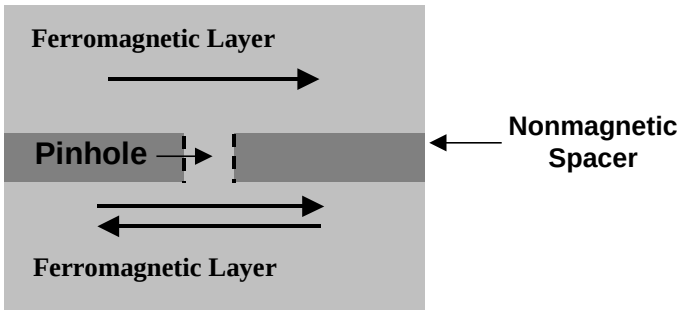

Figure 10 A schematic of GMR structure with a pinhole in the spacer layer. The two ferromagnetic layers have direct contact.

Pinholes are believed to play a key role in limiting the performance of both GMR spin valves and MTJs [24]. It is generally believed that as the spacer layer (Cu for spin valves and Al_2O_3 for MTJs) is made thinner, the magnetoresistance (MR)

increases until pinholes occur. Pinholes couple the two magnetic layers ferromagnetically, making it difficult to achieve antiparallel alignment, and thereby limiting the MR.

Despite its profound effect on MR, pinholes are not easy to observe. There is some evidence from transmission electron microscopy (TEM) on the existence of pinholes, but in systems such as Co/Cu/Co the low electron-scattering contrast between elements of similar atomic number makes conclusive identification of pinholes difficult. Another problem is that the thickness of the Cu layer is typically much smaller (~2 nm) than the depth of the TEM sample in the beam direction (~20 nm). If the diameter of a pinhole in the Cu film is similar to the thickness of the Cu film, it would be only ~10 % of the sample depth, exacerbating the contrast problem. In systems such as Al_2O_3/Co, there is some evidence that electrochemical deposition of Cu clusters can identify pinholes, although the applied potential may also create pinholes.

Two groups have recently reported the use of magnetic hysteresis loops to study coupling between magnetic films of different coercivity separated by an insulating film [25]. Their method appears to have much promise and we extend their approach. The present work has two aims. One is to develop an improved method for observing the onset of pinholes as the spacer layer is made thinner, and the other is to develop an improved method for distinguishing the regime of spacer-layer thickness in which pinhole coupling dominates from the one in which orange-peel coupling dominates.

2.1.2.1 Pinhole detection: experimental details

The NiO substrates used were polycrystalline films ~50 nm thick, deposited on 4" Si wafers by reactive magnetron sputtering at the University of California at San Diego. At the National Institute of Standards and Technology (NIST), the wafers were cleaved into ~1 cm^2 squares, cleaned ultrasonically in a detergent solution, rinsed in distilled water, blown dry, and installed in the deposition chamber. After bakeout, the deposition chamber has a base pressure of $3x10^{-8}$ Pa ($2x10^{-10}$ Torr), of which 90% is H_2. The metal films were deposited at room temperature by dc-magnetron sputtering in 0.3 Pa (2 mTorr) Ar at a typical rate of ~0.05 nm/s. Oxide films are deposited by reactive sputtering, adding 0.01 Pa (10^{-4} Torr) O_2 to the Ar. Magnetoresistance (MR) measurements were made at NIST with a 4-point probe in a direct current mode. The values of the coupling reported have an estimated uncertainty of $\pm$ 5 % due to the slight skew in the hysteresis loop of the free Co layer. The calibration of the Hall probe used for measurement of the applied field during MR measurements has an uncertainty of $\pm$ 2 %. The measurements at 77 K were performed with the sample immersed in liquid nitrogen. Additional experimental details may be found in Ref. [26].

2.1.2.2 Pinhole detection: on-set of the pinhole formation in GMR and MTJ structures

Structures of the type illustrated in Fig. 11 were used to investigate the magnetic coupling between two ferromagnetic layers. The concept behind the structure in Fig. 11 is to have two Co films separated by a non-magnetic spacer layer.

The upper Co film is magnetically pinned by the synthetic antiferromagnet (SAF) Co/Ru/Co and the natural antiferromagnet $Ir_{20}Mn_{80}$. The Co film below the non-magnetic spacer layer is free to switch at low field if the spacer layer is thick enough to prevent magnetic coupling.

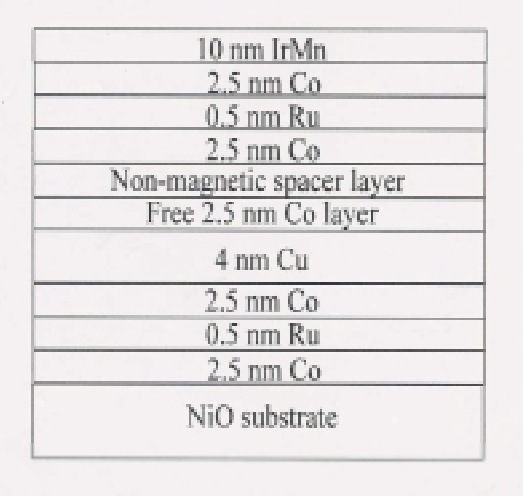

Figure 11 An illustration of the stack detail of the synthetic spin valve structure used in this study.

The lower parts of the structure constitute a GMR spin valve. GMR measurements are used to observe the hysteresis loop of the free Co layer. The synthetic antiferromagnet Co/Ru/Co and the natural antiferromagnet NiO substrate serve to pin the Co layer that is under the Cu. The Cu layer thickness in the spin valve is chosen to be 4 nm to ensure that the contribution to the coupling is insignificant from the Co layer below the Cu.

The coupling is observed as a shift from zero field in the center of the GMR hysteresis loop of the "free" Co. Figure 12 presents the coupling data for Al_2O_3 as the non-magnetic spacer layer. With no spacer layer, the two Co films form a single

layer 5 nm thick and the hysteresis loop center is shifted ≈30 mT (300 Oe) from zero field. At 77 K this shift increases to ≈60 mT (600 Oe) as the synthetic antiferromagnet Co/Ru/Co becomes stronger.

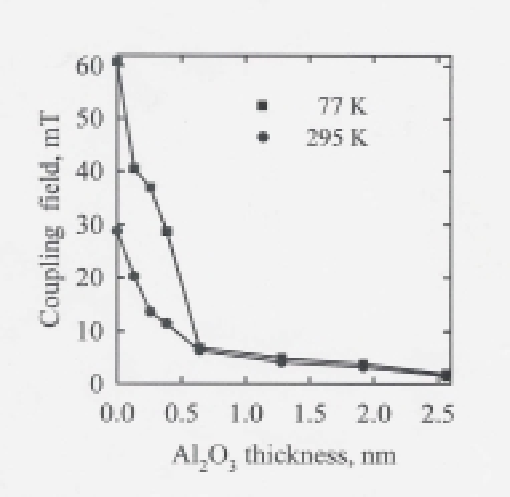

Figure 12 The coupling field observed in the GMR hysteresis loop of the free Co layer when the non-magnetic spacer layer is Al_2O_3, as a function of the spacer layer thickness.

In Fig. 12 a spacer layer of 0.6 nm Al_2O_3 is sufficient to suppress any significant temperature dependence in the coupling field. This is the apparent thickness at which magnetic pinholes cease to be significant. The coupling that is observed for 0.6 nm or more of Al_2O_3 is probably magnetostatic and comes from the orange-peel effect [27]. Only a very slight increase in orange-peel coupling would be expected since the magnetization of Co increases by less than 1 % from 295 K to 77K.

It is significant that the magnetic pinholes appear to close up at an Al_2O_3

thickness of 0.6 nm. In studies of magnetic tunnel junctions, it is generally found that this is the practical limit on how thin the Al_2O_3 barrier can be made. Thinner Al_2O_3 layers yield drastic reductions in tunneling MR [28]. The results of Fig. 12 suggest that, in this thickness regime, magnetic pinholes would make it difficult to achieve the antiparallel magnetic state. Moreover, as it is likely the magnetic pinholes represent direct Co-Co contacts and these pinholes may be expected to act as current short circuits as well.

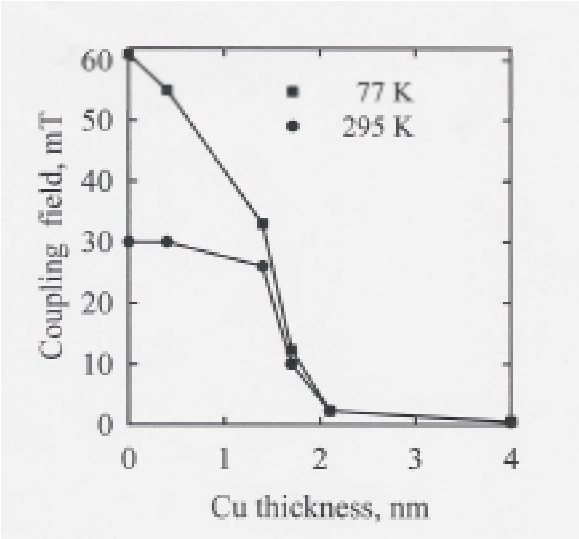

Figure 13 The coupling field observed in the GMR hysteresis loop of the free Co layer when the non-magnetic spacer layer is Cu, as a function of the spacer layer thickness.

Figure 13 presents the coupling results for Cu as the non-magnetic spacer layer. Note that this choice of spacer layer turns the structure into a dual spin valve. As a result, there will be a contribution to the GMR from the top half of the dual spin valve. However, this effect does not detract from the validity of the measured

coupling. The bottom Cu film is fixed at a thickness of 4 nm to make any contribution to the coupling from that side negligible. Only the upper Cu layer thickness is varied, and its thickness alone is responsible for the observed coupling.

The temperature dependence observed in Fig. 13 suggests that the magnetic pinholes dominate the coupling for Cu thicknesses from 0 nm to ≈ 1.5 nm and become insignificant when the Cu is thicker than ≈ 2 nm. Not surprisingly, this thickness corresponds well with what is generally used in GMR spin valves. It is commonly observed in GMR spin valves when Cu is thinner than 2 nm the coupling rises steeply [29].

2.1.2.3 Pinhole detection: conclusions

In summary, the temperature dependence of the magnetic coupling is found to be a useful approach to separating the effects of magnetic pinholes in non-magnetic spacer layers from the effects of magnetostatic coupling, such as the orange-peel effect. Test structures based on GMR spin valves are convenient for investigations of such phenomena. We find that, for Cu films of ≈ 2 nm or more and for Al_2O_3 films of ≈ 0.6 nm or more, magnetic pinholes do not make a significant contribution to the coupling.

2.2 Electrical properties of metallic electrodes separated by Al_2O_3 layer and ultra-thin aluminum oxide as thermal oxidation barrier on metal films

Magnetic tunnel junctions (MTJs), owing to the discovery of large MR, have attracted a lot of interest [30]. For high quality MTJs the tunnel junction is

made by exposing an Al film to O_2, a process referred as natural oxidation [31]. An important fabrication issue is the quality of the Al_2O_3 barrier [32]. Our experiments include two stages: the first is to investigate the proper oxidation condition and the thickness dependence of the tunneling property of Al_2O_3 barriers, and second, since to date all experimental work appears to have used Al oxidation at room temperature and annealing often smoothes the surface of a film and makes its thickness more uniform, the experiment is intended to determine the maximum annealing temperature possible without oxidation of the underlying metal. Although Mn, Ta, Cu and Cr are unrelated to magnetic tunnel junctions, they were included in this study because there is surprisingly little data in the literature on the high temperature oxidation of ultrathin metal films in air.

The sample structure for first experiment is shown in Fig. 14. The sample was masked between the deposition of two 5 nm Co layers, the junction area is ~ 1cm x 1mm. Two methods were used to fabricate Al_2O_3. One is by deposition of Al followed by exposure to pure O_2. Only 10% of samples produced demonstrated tunneling properties. The other method is to deposit Al in 1 x 10^{-3} mT O_2 and 3 x 10^{-3} mT Ar, which produced 50% success rate. Samples with different thickness of Al_2O_3 were made and I-V curves were measured to determine tunneling property.

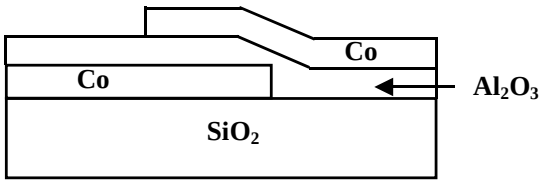

Figure 14 Magnetic tunneling junction experimental structure.

The tunneling current density transmitted through a rectangular potential barrier with height $\bar{\phi}$ and thickness t_{bar} is represented by the following equation derived by Simmons [33].

$$J(V) = \frac{6.17x10^{10}xA}{t_{bar}^2}\left[\left(\bar{\phi} - V/2\right)\exp\left(-1.025\sqrt{\bar{\phi} - V/2}\, t_{bar}\right) - \left(\bar{\phi} + V/2\right)\exp\left(-1.025\sqrt{\bar{\phi} + V/2}\, t_{bar}\right)\right] \quad (2\text{-}8)$$

In order to evaluate the electrical quality of the Al_2O_3 thin films grown under the second methods, the I-V characteristics of Co/ Al_2O_3 /Co junction were measured and compared to the theoretical calculation results from Simmons model. The experiment is in good agreement with the calculation as shown in Fig. 15.

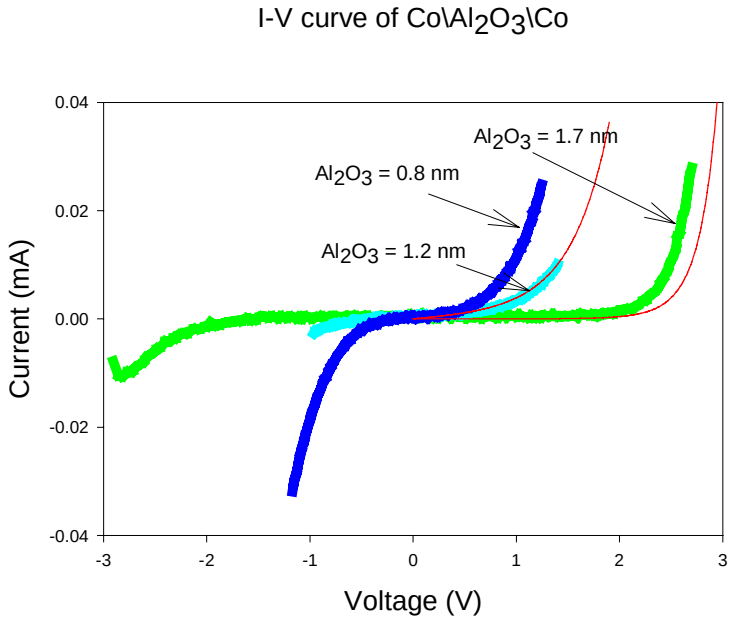

Figure 15 I-V curves of Al_2O_3. The thick solid lines are experimental results for 0.8nm, 1.2nm and 1.7nm thick barriers, and the thin red solid lines are theoretical calculated results for 1.2nm and 1.7nm barrier.

2.2.1 Ultra-thin aluminum oxide as thermal oxidation barrier on metal films: experimental set-up

The Si(100) wafers with a 350 nm thermal oxide at the surface were cleaved into 1 cm x 1.5 cm rectangular pieces, cleaned ultrasonically in detergent solution, rinsed in distilled water, blown dry, and installed in the deposition chamber. After using ion milling to ablate ≈ 2 nm of the surface to remove any contamination, metal films were deposited at room temperature by dc-magnetron sputtering. The base pressure of the system is about $3x10^{-8}$ Pa ($2x10^{-10}$ Torr) and 0.3 Pa ($2x10^{-3}$ Torr) Ar was used for sputtering.

Because some metals tend to agglomerate on the SiO_2 surface, 1 nm Ta was first deposited as the seed layer to promote better adhesion for the metal films. Next a 10nm metal film was deposited on Ta. Identical samples were prepared with the addition of 0.3 nm Al and 1 nm Al. Eight different metals were studied: Co, Ni, Fe, NiFe, Mn, Ta, Cu and Cr. Also, a sample with 11nm Al was investigated for comparison. The study of metal oxidation by the measurement of the resistance change is a well-established technique [34]. In our work, 4-wire resistance measurements were performed at room temperature after annealing the samples in air. The ohmmeter had a NIST traceable calibration with a quoted accuracy of ± 1%. The samples were placed in an oven with a digital temperature control calibrated to ± 10^{o}C for approximately 30 seconds, which allowed them to reach the reported temperatures, and cooled by quenching in water.

2.2.2 Ultra-thin aluminum oxide as thermal oxidation barrier on metal films: results and discussions

The measured resistances versus annealing temperature are presented in Fig. 16 to Fig. 24. Some samples showed slight decrease in resistance with increasing temperature, probably due to annealing out the defects. All samples were heated until the resistance exceeded the 20 MΩ limit of the Ohmmeter.

The largest effects of the Al protecting layer are found for Co in Fig. 16 and Ni in Fig. 17. The onset of oxidation is increased to ≈ 300^{o}C for 1 nm Al. The smallest effect is found for Fe, ≈ 100^{o}C, in Fig. 18. Permalloy ($Ni_{80}Fe_{20}$) is an intermediate case, in Fig. 19. The Co, Fe and Permalloy cases are of the most interest for MTJ studies. The implication of these results is that a naturally oxidized MTJ tunnel barrier can be annealed to temperatures several hundred degrees without significant oxidation of the underlying magnetic metals. Perhaps the most surprising result of the study is that a mere 1 nm Al (which becomes 1.3 nm Al_2O_3 in air) can protect Co and Ni films from oxidation in air at temperatures of over 600^{o}C and 700^{o}C, respectively. This result was most unexpected and is an indication that how smoothing of the Al_2O_3 surface by annealing might be possible.

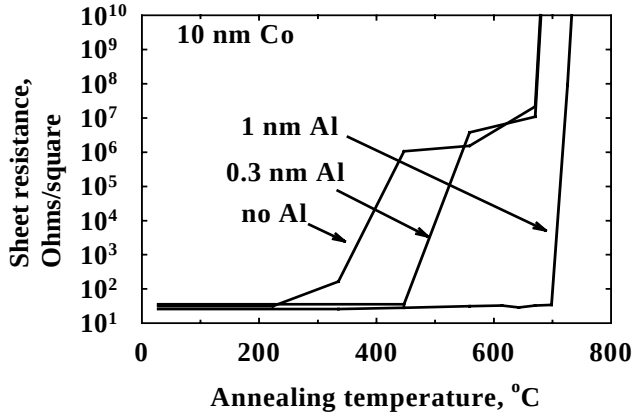

Figure 16 The room temperature resistance of Co film with Al protection layer of different thickness following annealing for 30 seconds at the indicated temperatures.

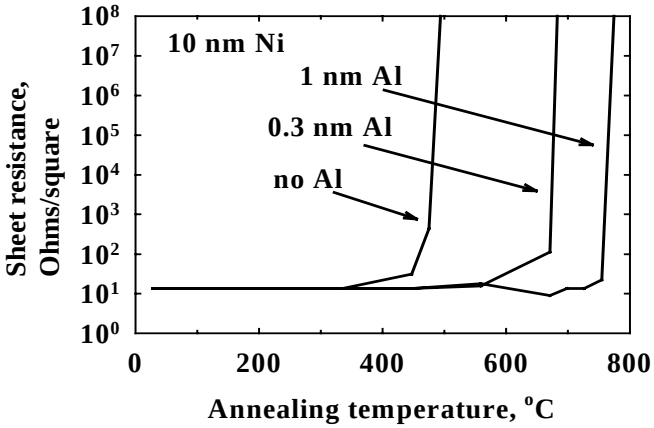

Figure 17 The room temperature resistance of Ni film with Al protection layer of different thickness following annealing for 30 seconds at the indicated temperatures.

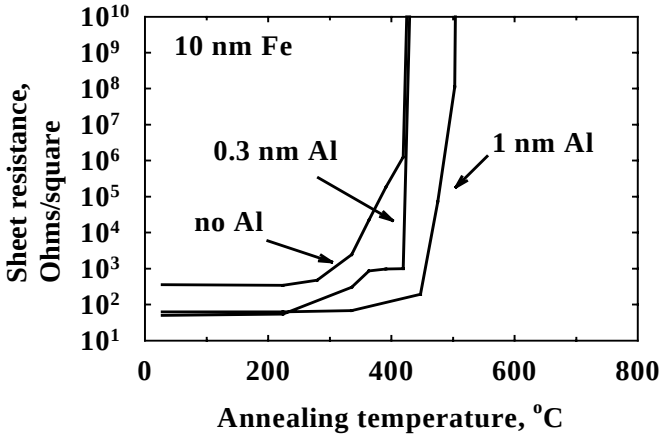

Figure 18 The room temperature resistance of Fe film with Al protection layer of different thickness following annealing for 30 seconds at the indicated temperatures.

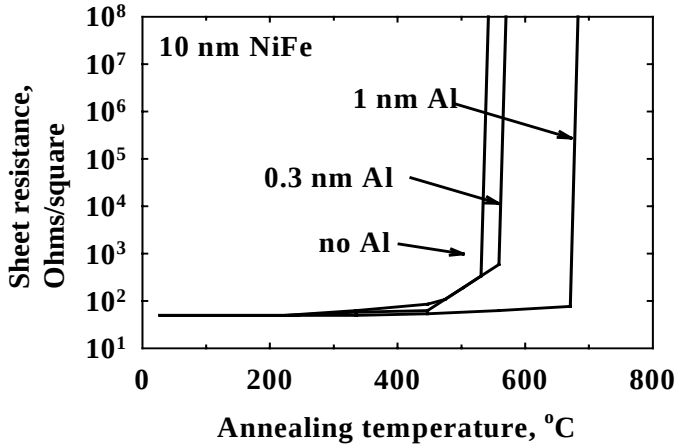

Figure 19 The room temperature resistance of NiFe film with Al protection layer of different thickness following annealing for 30 seconds at the indicated temperatures.

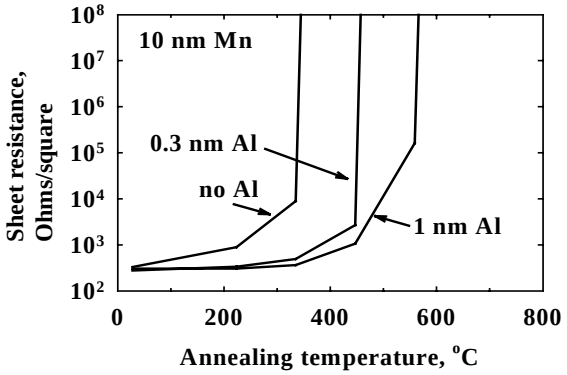

Figure 20 The room temperature resistance of Mn film with Al protection layer of different thickness following annealing for 30 seconds at the indicated temperatures.

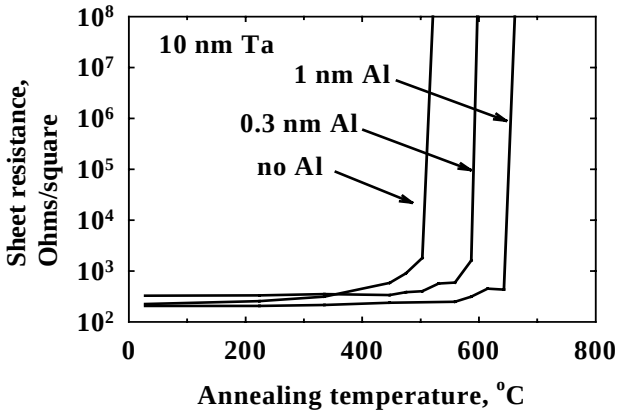

Figure 21 The room temperature resistance of Ta film with Al protection layer of different thickness following annealing for 30 seconds at the indicated temperatures.

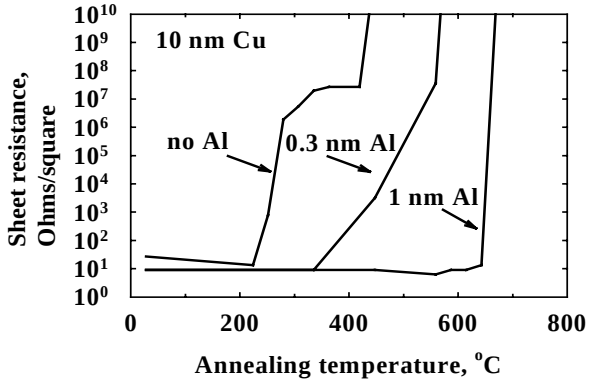

Figure 22 The room temperature resistance of Cu film with Al protection layer of different thickness following annealing for 30 seconds at the indicated temperatures.

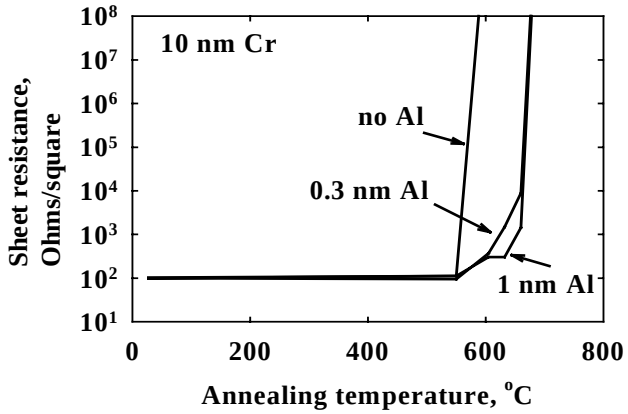

Figure 23 The room temperature resistance of Cr film with Al protection layer of different thickness following annealing for 30 seconds at the indicated temperatures.

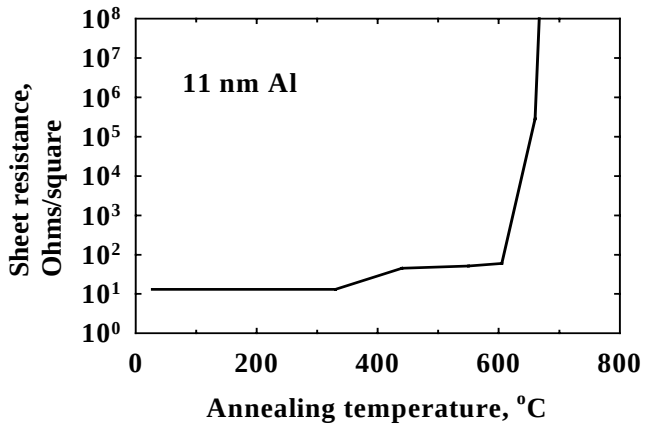

Figure 24 The room temperature resistance of 11 nm Al layer following annealing for 30 seconds at the indicated temperatures.

Four other metals were also investigated primarily out of curiosity. They were Mn, Ta, Cu, and Cr, in Fig. 20 to Fig. 23. In the case of Cu, the flat region around 400°C for the "No Al" sample is quite reproducible and seems to reflect a semi-conducting oxide, probably Cu_2O. The same phenomenon seemed to occur for Co.

In some cases, we can use published data to estimate the temperatures needed to oxidize 10 nm of a metal in air in a few seconds. The oxide growth law is shown below:

$$\Delta M / A = K_p t \qquad (2\text{-}9)$$

where ΔM is change of mass, A is area unit, t is oxidizing time, and K_p is the parabolic rate constant which is a function of temperature. Using the K_p value from Ref. [35] for the oxidation of macroscopic Ni films, the temperature needed to oxidize 10 nm Ni in a few seconds is estimated to be ~600°C. In Fig. 17, the

temperature is observed to be ~500^{o}C. It is likely that our samples have a smaller grain size and more readily oxidized.

In order to clarify the results of Fig. 16 and Fig. 17, X-ray photoelectron spectroscopy (XPS) was used to study the oxidation process. Fig. 25 indicated that without an Al overlayer, the Co 2p peaks shifted to larger binding energy after annealing at 300°C indicating that CoO is formed, as expected. For comparison the intensity of oxygen 1s peak is also reported (The width was approximately constant in these data).

For a Co film with 1 nm Al on top, Fig. 26 shows that the peaks did not shift to the CoO binding energy until the samples were annealed at 800°C. This result supported the implication of Fig. 16 that the 1 nm thin Al film not only protects the underlying Co from air oxidation, but also increases the onset oxidation temperature of Co by ≈ 300°C. At 800°C, inter-diffusion between Al_2O_3 and CoO appear to have taken place since the Al peak disappeared. An interesting feature of the data is that after annealing at 700°C, the Co 2p peaks are quite small, although they are still at the binding energy for metallic Co. The reason for this is unclear, but may be related to some structural rearrangement due to the softening of the thermal oxide substrate. Thermal oxide is quite similar to glass, and while both are amorphous and thus do not have a melting point, both are quite fluid at 700°C. It is remarkable the Co does not oxidize and maintains a constant resistance after apparently floating on liquid thermal oxide during anneal.

The XPS results in Fig. 27 and Fig. 28 for Ni films and the interpretation of them are quite similar to those of Co, with one clear exception. When Al is deposited

on Ni surface a strong interfacial reaction occurs leading to the formation of ≈ 2 nm of NiAl alloy [36]. In this alloy the Ni 2p peaks are shifted to a binding energy ≈1eV larger than in pure Ni [37]. What is apparent in Fig. 28 is that upon oxidation of the surface the Ni 2p peaks shifted from the alloy binding energy to smaller pure metal binding energy. The large heat of oxidation of Al provides the thermodynamic driving force for this de-alloying of Al and Ni. The drop in intensity of the Ni peaks from the as deposited state to the 300°C anneal may be attributed to the de-alloying reaction. As deposited, the top 1 and 2 nm of the sample will be roughly $Ni_{50}Al_{50}$. The Ni peak intensity drops as the Al diffuses to the surface to from an overlayer of ≈1.3 nm Al_2O_3. A similar de-alloying very likely occurs in the Co and Fe samples although it is more difficult to observe since there is no corresponding shift in Co and Fe core-level binding energies and the extent of alloying is less.

In the case of Co and Ni samples, additional evidence for de-alloying process comes from the Al 2p and 2s core-level peaks which appear at the binding energy for Al_2O_3 after annealing in air with no detected intensity at the binding energy of metallic Al. Apparently, the de-alloying process runs to completion.

As in the case of Co, the Ni peaks remain at the pure-metal binding energy until oxidation finally occurs during the annealing at ≈ 770°C. This result is consistent with stable resistance observed in Fig. 17. Also as in the case of Co, there is a drop in the core-level intensities as the thermal oxide reaching fluid temperature, e.g. 600°C. The explanation for the drop and the absence of any corresponding resistance change are not apparent.

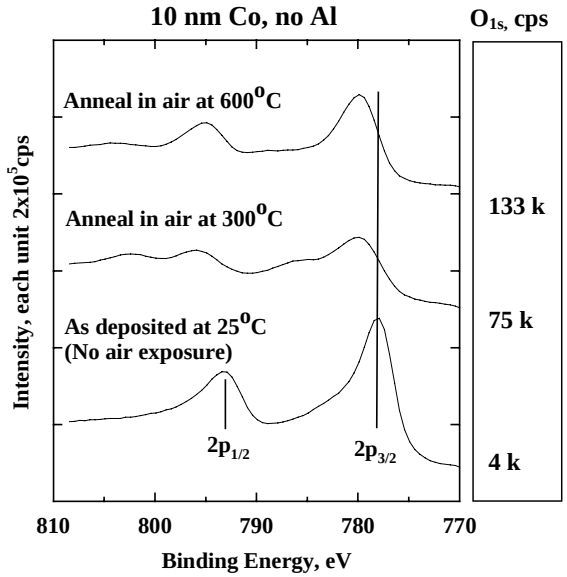

Figure 25 XPS data on the pure Co film after annealing at different temperatures. Also reported are the corresponding O 1s core level intensities.

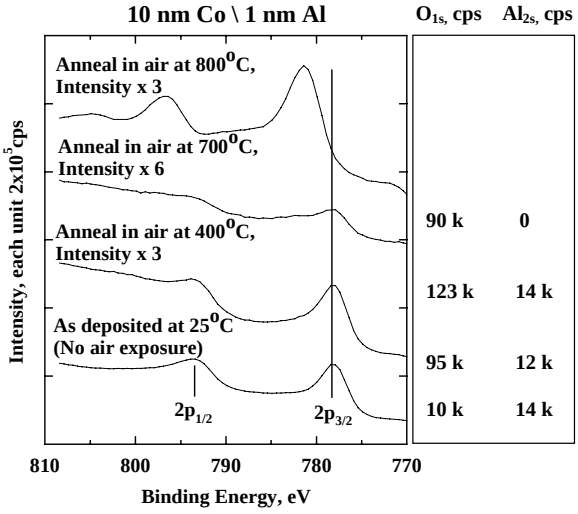

Figure 26 XPS data on the Co film with Al protection layer after annealing at different temperatures. Also reported are the corresponding O 1s core level intensities.

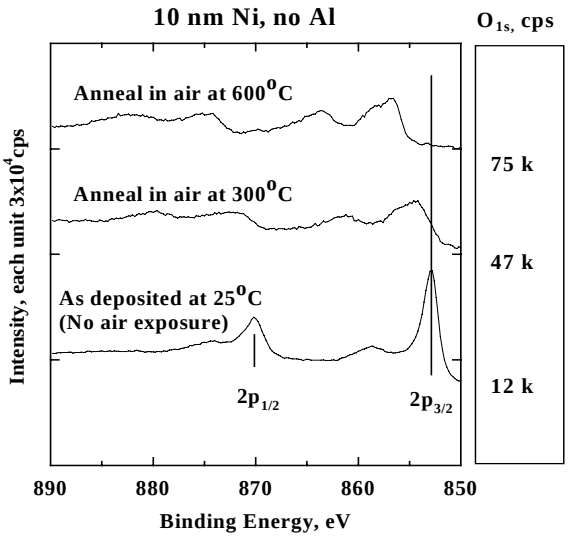

Figure 27 XPS data on the pure Ni film after annealing at different temperatures. Also reported are the corresponding O 1s core level intensities.

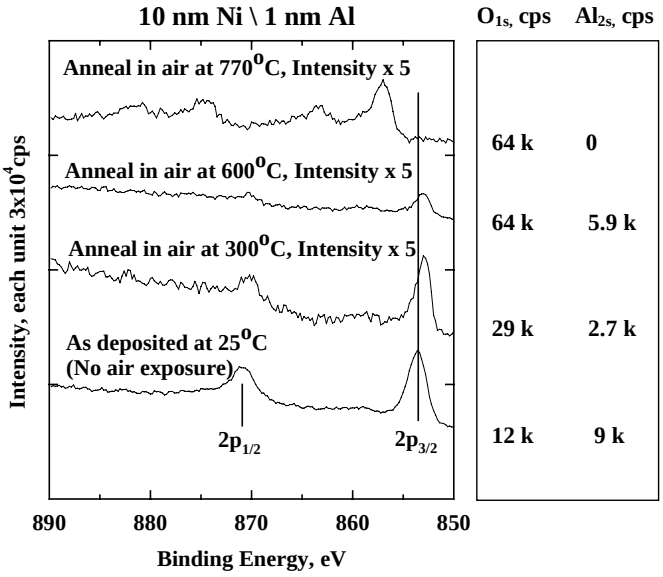

Figure 28 XPS data on the Ni film with Al protection layer after annealing at different temperatures. Also reported are the corresponding O 1s core level intensities.

2.2.3 Ultra-thin aluminum oxide as thermal oxidation barrier on metal films: conclusions

To recall, the main conclusions of our findings are:

1) Layer of Al as thin as 0.3 nm and 1 nm provide significant protection against thermal oxidation in air at elevated temperatures for a variety of metals.
2) For Co\Al and Ni\Al samples annealing in air promotes a de-alloying process in which the Al intermixes with the Co or Ni upon deposition, then diffuses to the surface to form an Al_2O_3 layer.
3) It is likely that annealing these samples in air promotes a smoother Al_2O_3 film of more uniform thickness and with sharper metal\Al_2O_3 interface. If so, this approach might be useful in achieving improved magnetic tunnel junctions.

2.3 Thin Al, Au, Cu, and Ta Films as Oxidation Barriers for Co in Air

In the field of magnetic thin films, it is often necessary to transport films through air for certain measurements or tests to be made. Very often some protecting overlayer is needed to prevent oxidation of the magnetic thin film and any possible modification of the film properties. The motivation of the present work is to help provide a scientific basis for such choices.

In prior work, capping layers of Ag, Au, Al_2O_3 and metal silicides were investigated with varying degree of success [38-41]. Ag provided the poorest protection and silicides the best protection. However, the silicides had to be grown at elevated temperature in SiH_4 gas, a procedure that is rarely compatible with magnetic

thin-film deposition equipment. Our aim is to assess the degree of protection provided to magnetic thin films by metals that are likely to be readily available in a deposition system. In this work, we investigated capping layers of Al, Au, Cu, and Ta with thicknesses up to 4 nm.

2.3.1 Thin Al, Au, Cu, and Ta films as oxidation barriers for Co in air: experimental set-up

The substrates used in this experiment are 1 cm x 2 cm Si(100) with a 350 nm thermal oxide on the surface. The cleaning procedure was to immerse the substrate in detergent solution in an ultrasonic bath for a few seconds, rinse it with distilled water, blow it dry, introduce it into our vacuum chamber, and remove ~ 2 nm of the surface by ion milling. Next, a structure of 1 nm Ta, 5 nm Co, and a capping layer of the selected material was deposited at room temperature by DC magnetron sputtering in 0.4 Pa Ar. The structure is shown in Fig. 29. The base pressure of the system is ~ 10^{-6} Pa of which 90 % is H_2. The Ta seed layer provides better adhesion for the Co films. Different thicknesses of six metals, Al, Au, Cu, and Ta, were deposited as capping layers to protect against oxidation of Co in air. The films were investigated by x-ray photoelectron spectroscopy (XPS) using Al Kα x-rays immediately after deposition and again after exposure to air for varying lengths of time. To obtain XPS data on CoO films of varying thickness, we reactively sputtered Co in 10^{-2} Pa O_2 on the thermal oxide. The thickness of deposited films was determined by two quartz-crystal oscillators adjacent to the substrate, and their estimated accuracy was $\pm$ 10 %.

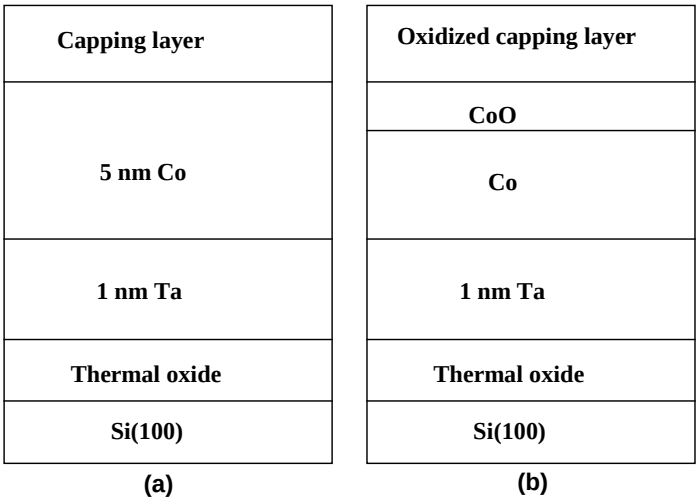

Figure 29 The multi-layer structure used in this experiment. The structure before exposure to air is shown in (a), and the structure after oxidation by air is shown in (b).

2.3.2 Thin Al, Au, Cu, and Ta films as oxidation barriers for Co in air: Results and discussion

Our analysis of the oxidation of Co is based on the very different Co $2p_{3/2}$ core-level lineshapes for metallic Co and CoO. This difference is illustrated in Fig. 30. Although the core-level intensity is attenuated by the capping layer, we found that we can collect useable spectra with capping layers as thick as 4 nm.

When the surface layers of a Co film are oxidized, the $2p_{3/2}$ core level has a characteristic lineshape that can easily be resolved into metallic and oxidized components. Figure 31 illustrates our approach. The Co $2p_{3/2}$ core-level line shape for metallic Co is scaled and subtracted from the total signal to leave the line shape of

the oxidized Co. The scaling is subject to little ambiguity because only minor changes in the optimum scaling leave a lineshape that does not closely resemble the CoO line shape of Fig. 30 (b). We estimate the uncertainties of the peak areas of Co and CoO determined in this manner to be $\pm$ 10 %.

In order to determine the thickness of CoO in a particular sample we deposited CoO films of different thicknesses on Co, recorded the $2p_{3/2}$ lineshapes, and resolved the spectra into the metallic and oxidized components. With such data as a reference, we can determine the thickness of CoO in an unknown sample to an estimated uncertainty of $\pm$ 20 %.

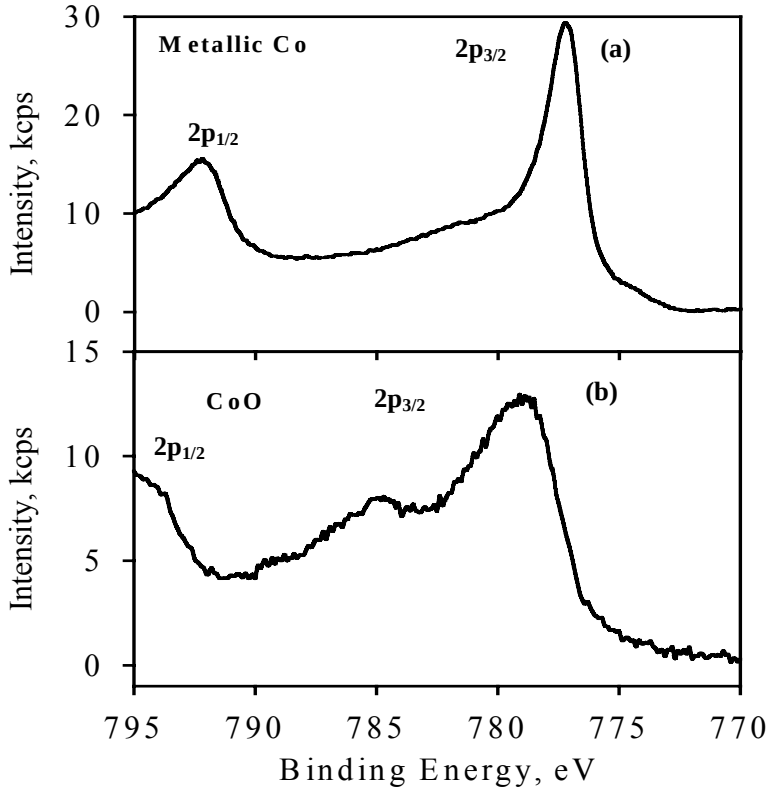

Figure 30 The Co $2p_{3/2}$ core-level lineshape for (a) 5 nm of Co and (b) 5 nm of CoO.

The relative intensities of the metallic and oxidized components in Fig. 31 (a) correspond to an oxide thickness of 1.1 nm. While a more detailed analysis could improve our accuracy, our goal is not to obtain highly accurate estimates of the CoO thickness. Instead, our goal is to establish the onset of Co oxidation so that we know how effectively the capping layer protects the Co, and this simple approach seems adequate to meet our needs.

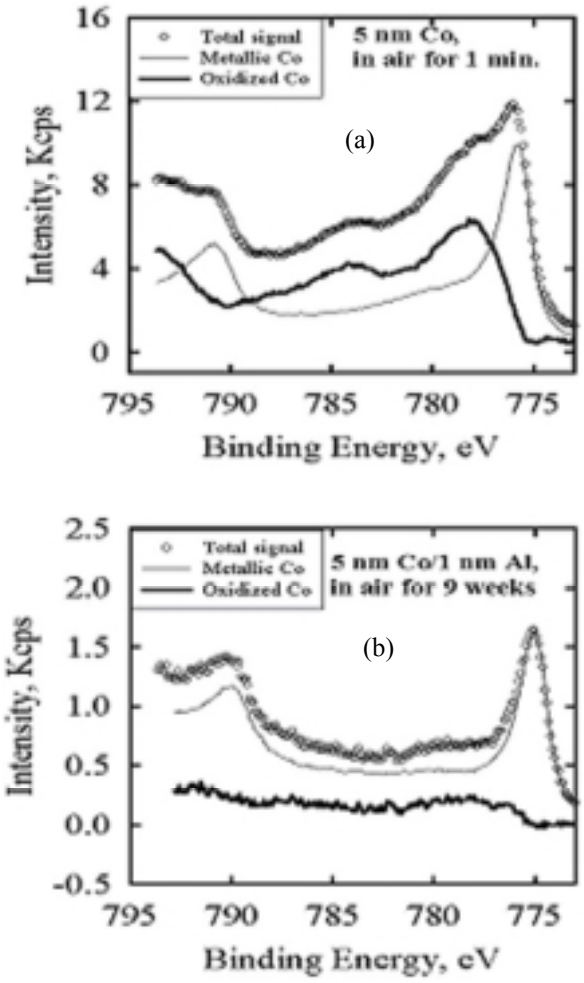

Figure 31 Illustration of separation of the metallic Co and the CoO components of the Co $2p_{3/2}$ core-level signal (a) a 5 nm Co film exposed to air for 1 minute, and (b) a 1 nm Al capping layer on 5 nm Co exposed to air for 9 weeks.

An underlying assumption in our analysis is that the CoO/Co interface is atomically flat and sharp. Support for this assumption comes from the well-known phenomenon in giant magnetoresistance samples that Co films scatter electrons more specularly after oxidization of the surface. Apparently, Co tends to oxidize in a layer-by-layer manner [29, 42].

The only capping layer for which the above assumptions do not work extremely well is Al. In that case, just before the onset of the characteristic CoO lineshape in the spectra a weak feature with a distinctly different line shape appears. Figure 31 (b) illustrates this case. Instead of the characteristic two-peak lineshape of oxidized Co in Figs. 30 (b) and 31 (a), a single peak is observed at 779 eV. It is possible that this peak may represent Co atoms that are not fully oxidized, but share O ions with Al ions. Support for this view comes from the fact that whenever the single-peak state is observed, the characteristic two-peak CoO lineshape is also observed. It seems that the oxidation front is moving steadily deeper into the sample. It is also possible that the one-peak state may be connected with the intermixing at the interface that occurs when Al is deposited on Co [36]. The oxidation of this alloyed region may somehow be connected with the single-peak state.

Fig. 32 (a) to (f) presents plots of the CoO thickness versus time-in-air for six different capping layers. For an uncapped Co film, 1 nm of CoO forms immediately in air (in fact, even 10^{-2} Pa O_2 forms 1 nm of CoO almost immediately). Subsequent oxidation proceeds at an exponentially slower rate. In most cases, sub-nanometer films of the capping layer significantly reduce the Co oxidation rate. However, more

than 1 nm is required for most capping layers to provide protection for any significant length of time, i.e., one day.

Surprisingly, Au is not a particularly good capping layer. Its inertness to oxygen would suggest it might be the best. Although we could not find any published references to its use as a capping layer, we know from informal survey that it is a common choice in protecting magnetic thin films. One advantage of using Au as a capping layer is that it does not intermix extensively with the magnetic metal on which it is deposited, unlike Al capping layers. Cu also has the advantage of not intermixing extensively with magnetic thin films, but as seen in Fig. 32 (c) it is even less successful in protecting the Co than Au. Perhaps Au layers thicker than 4 nm would be successful, but 4 nm is about the upper limit of what we can use in an XPS study. Nevertheless, an extrapolation from our data gives an important suggestion for cases in which Au cap layers are highly desirable. As seen in Fig. 32 (b), there is a 20-fold increase in the time to the onset of Co oxidation in going from 1 nm to 2 nm Au and also in going from 2 nm to 4 nm Au. This result suggests that if 10,000 hours of protection were needed, a plausible guess at the Au thickness required would be 8 nm.

Although Al and Ta seem to give the best protection from oxidation, they are not entirely benign as capping layers. In other studies, we have found that an Al capping layer form an intermixed layer with approximate thicknesses of 0.6 nm on Fe, 0.9 nm on Co, and 2 nm on Ni. We have not performed a thorough study of intermixing with Ta capping layers, but our studies of magnetization versus Co thickness indicate that when a Ta capping layer is deposited on Co, the top 0.5 nm to

1 nm of the Co is no longer ferromagnetic [43]. Thus, it seems likely that Al and Ta intermix to similar extents on magnetic thin films.

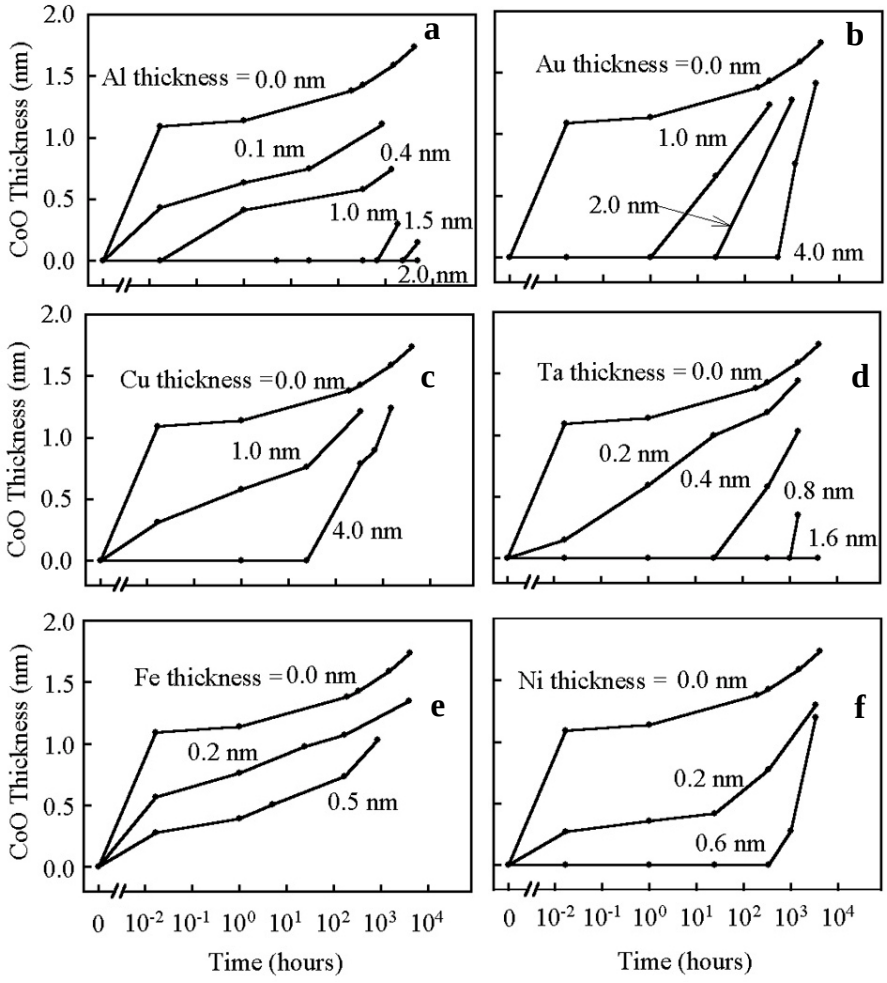

Figure 32 Plots of the thickness of CoO versus time in air for the indicated thickness of (a) Al, (b) Au, (c) Cu, (d) Ta, (e) Fe and (f) Ni.

2.3.3 Thin Al, Au, Cu, and Ta films as oxidation barriers for Co in air: conclusions

The major conclusions of this work are:

1) XPS is a useful method of observing the onset of oxidation of Co films that are protected by thin capping layers.
2) Al and Ta capping layers provide the best long-term protection from oxidation in air, but suffer from the disadvantage that they intermix with the Co to a depth on the order of 1 nm.
3) Au and Cu capping layers do not intermix extensively with Co but only provide rather short-term protection from oxidation in air.

2.4 Ballistic Magnetoresistance in nanocontacts through various fabrication methods

2.4.1 Introduction

Over the past several years reports of extremely large values for the magnetoresistance in ferromagnetic nanocontacts when a magnetic domain wall is presumed to lie in the nanocontact have been published [44-54]. The key idea is that if the spatial extent of the domain wall is less than the spin-flip mean-free-path of electrons, the electrons trying to cross the wall would have a high reflection probability due to poor matching of the Fermi surfaces of spin-up and spin-down electrons. This reflection manifests as a higher electrical resistance than when both sides of the nanocontact are magnetized in parallel. This is schematically illustrated in Fig. 33.

The recent work by S. H. Chung, et al. [13] showed BMR effects in Ni, CrO_2 and Fe nanocontacts using the break junction and in the process demonstrated the universality of the effect in various spin polarized systems. The experimental set-up is

shown in Fig. 34. A junction is built by placing two Ni rods of 1mm diameter with rounded tips into contact. The rods are tightly bound to a Teflon tube by a resin to tightly secure the junction. Using piezocontrolled micrometers, an axial force is applied at the end of one of the rods until nanocontact is formed, i.e., a few conductance quanta. Additionally, each rod is equipped with electromagnet coils that can independently establish the magnetization of the rods. Both resistance and the driving current on the rods are measured and recorded using a digital oscilloscope.

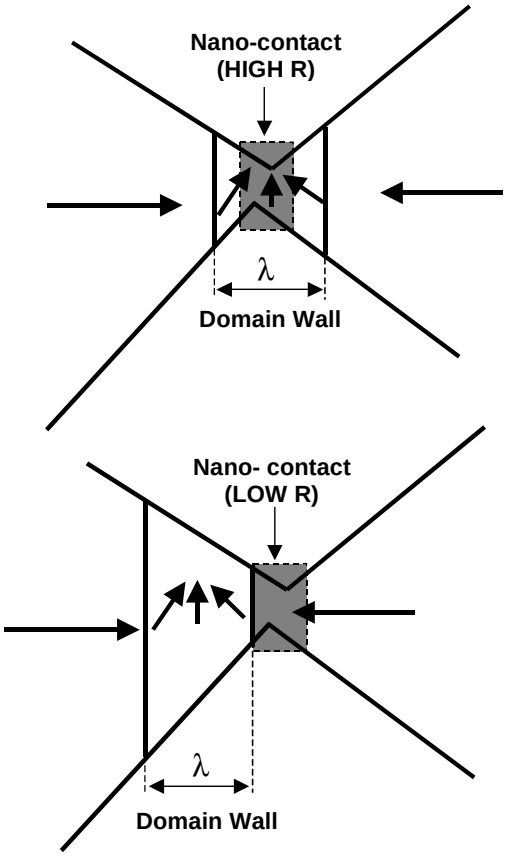

Figure 33 Two-resistance states at a nanocontact when λ width domain wall locates inside and outside of the nanocontact. The arrows indicate the magnetization directions.

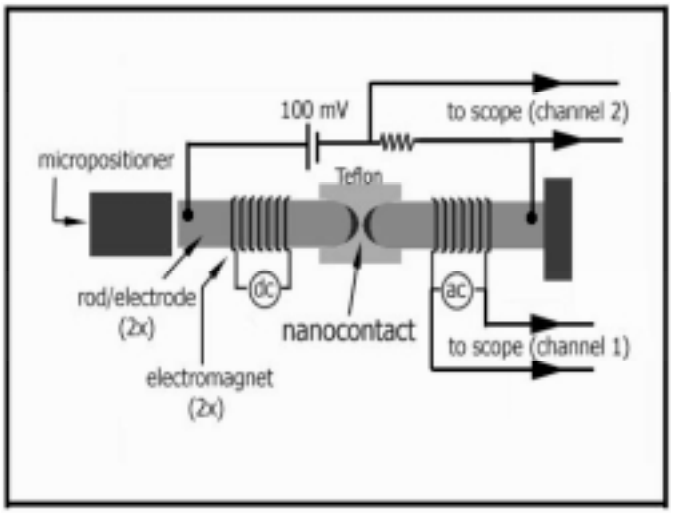

Figure 34 A schematic drawing of the set-up break junction nanocontact system.

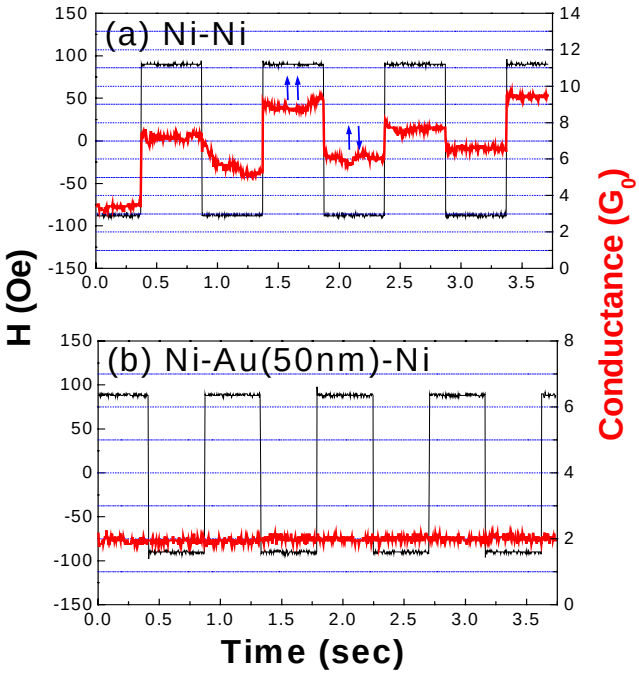

Figure 35 Typical magnetoconductance response of (a) Ni-Ni and (b) Ni-50nm thick Au-Ni nanocontact. Black and red lines represent applied ac magnetic field and conductance through nanocontact respectively.

A typical magnetoconductance response of a metallic nanocontact as acquired by the digital oscilloscope is shown in Fig. 35. In these traces the square current pattern, corresponding to amplitude of approximately ±90 Oe at the junction, was applied on one of the ferromagnetic electrodes. The voltage on the I/V converter, and hence the current across the junction was recorded at fixed bias voltage of 100 mV.

The current and the corresponding magnetoconductance show that, provided that one of the electrodes was saturated by the dc electromagnet, the resistance of the junction followed the square wave of the ac magnetic field of the other electrode at the same phase and frequency. Furthermore, succeeding experiments where one of the electrodes was coated with non-magnetic material (500 nm of Au) showed a complete suppression of the effect. These results imply that the magnetoresistance response comes from the spin-dependent transport and eliminate the possibility that they are caused by mechanical motion due to magnetostrictive or magnetostatic forces. Chung further showed the universality of the BMR effect and found it to be consistent with the theoretical model of Tatara [12]. More recent reports by H. Pandana [55] using a STM set-up have investigated the point junction resistance spacing from 1KΩ to 1MΩ. An enhanced MR effect appears at one resistance quanta 12.9KΩ for NiFe-NiFe nanocontact. Thus, in these experiments using mechanical break junctions, BMR effect is well established.

2.4.2 Planar BMR Structures

While BMR appears to be a highly sensitive magnetic sensor, practical applications require nanocontacts to be fabricated into a planar geometry. This fact is well recognized in the community and much work has recently been done on

magnetic nanocontacts, particularly electrodeposited contacts of Ni, Fe and Co [44-54]. Unfortunately, the claims of sensational MR ratios (more than 10000%!) that are attributed to ballistic magnetoresistance (BMR) are controversial. Alternative mechanisms involving magneto-mechanical effects that could lead to similar results have been overlooked, which casts a shadow of doubt on the veracity of BMR in planar structures.

In this part of my effort, the main goal is systematically elucidate the nature of BMR in planar systems and to dispel the common oversights that have unfortunately proliferated in the literature. I will revisit the experiments conducted by various groups [44-54], and systematically address how magnetomechanical effects can be the source of large MR changes in their results/

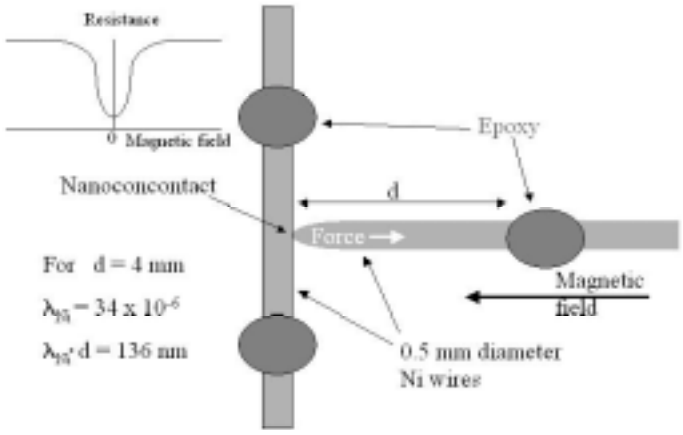

Figure 36 An illustration of a common geometry for BMR measurements and how it is subject to the artifact that magnetostriction will shorten the axial wire in an applied field. A resulting force will tend to stretch the nanocontact and if upon stretching it becomes smaller the resistance change will have the general features of the inset.

2.4.2.1 Electrodeposited ferromagnetic materials between two wires

We begin by replicating the experiments of Garcia [44]. The wires used in this work had a purity of 99.9% or better and were mounted on glass slides with epoxy. This is similar to the setup reported in Ref. 49. Except where otherwise noted, all electro deposition of Ni and Fe nanocontacts was carried out between -1.0 V and -1.5 volts versus a standard calomel electrode. A detailed account of the electrodeposition may be found in Refs. [56, 57]. Resistivity measurements were made either by 2-point or by 4-point techniques with an estimated accuracy of $\pm$ 0.01% of the measured value.

Figure 36 illustrates the "T"-structure geometry for BMR measurements. Not surprisingly, in this geometry the device shows low resistance at low field and a constant higher resistance at high field as shown in Fig. 36 inset. As in previous reports, we observed that the value of the low and high resistance states could vary by several order of magnitudes. Fig. 37 shows typical results obtained from the contacts using the geometry of Fig. 36 (as Fig. 37a) and illustrates the variation in the MR behavior due to slight inadvertent differences in mounting and electroplating conditions (as Fig. 37b and 37c). More importantly, we also obtained data shown Fig. 38a, showing what appears to be an infinite BMR effect!

However, BMR may not be responsible for the effect. Indeed, careful analysis suggests that this geometry is highly susceptible to magnetostriction and magnetostatic forces. When the applied field magnetizes the axial wire, magnetostriction will shorten wire and the resulting force can break the nanocontact or at least diminish the contact. For a 4 mm long Ni wire used in this experiment, the contraction due to magnetostriction is 136 nm, which far more than is needed to

deform a nanocontact. This breakage is not surprising in light of the 136 nm displacement. The conclusion to be drawn is that the geometry of Fig. 36 is so vulnerable to artifacts that it cannot be used to establish the validity of BMR.

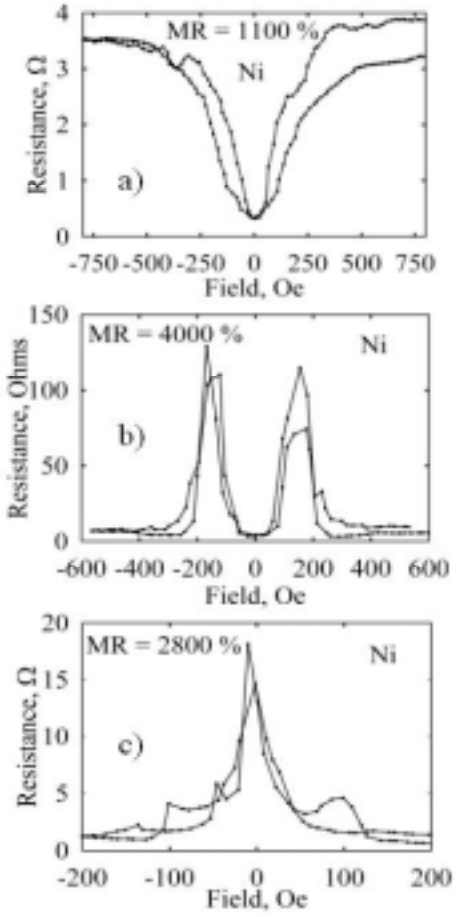

Figure 37 Three different generic types of data obtained on Ni samples in the geometry of Fig. 36, illustrating how inadvertent differences in sample mounting can lead to quite different artifacts dominating the data.

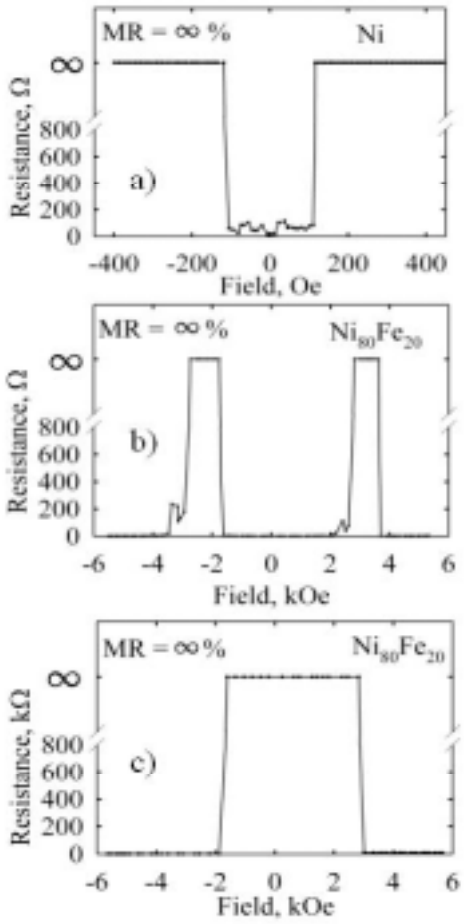

Figure 38 Magnetoresistance data on a) Ni wires in the geometry of Fig. 36, b) Permalloy wires in the geometry of Fig. 39a, and c) Permalloy wire in geometry of Fig. 39b.

There are additional factors at work to cause the emergence of artifacts in experiments using the geometry of Fig. 36. Fig. 37b and 37c illustrate our results obtained with Permalloy ($Ni_{80}Fe_{20}$) wires in the geometry of Fig. 36. Permalloy has almost no magnetostriction, which is ideal in negating the artifacts due to magnetostriction. Nevertheless even with this setup, we obtained results shown in

Fig. 38b and 38c with infinite MR! The effect can be explained by considering magnetostatic forces. The heavy arrows in Fig. 39a indicate the magnetostatic force that the transverse wire experiences from the field gradient of the magnet. This force would tend to break the contact. Using this concept, along with the electrostatic interaction at the junction, we can explain the features of Fig. 38b. As the field is increased, the transverse wire experiences an attraction towards the pole face, breaking the nanocontact. However at higher field the magnetization of the transverse wire follows the direction of the field that subsequently establishes a strong magnetostatic attraction, which takes over and re-establishes the contact.

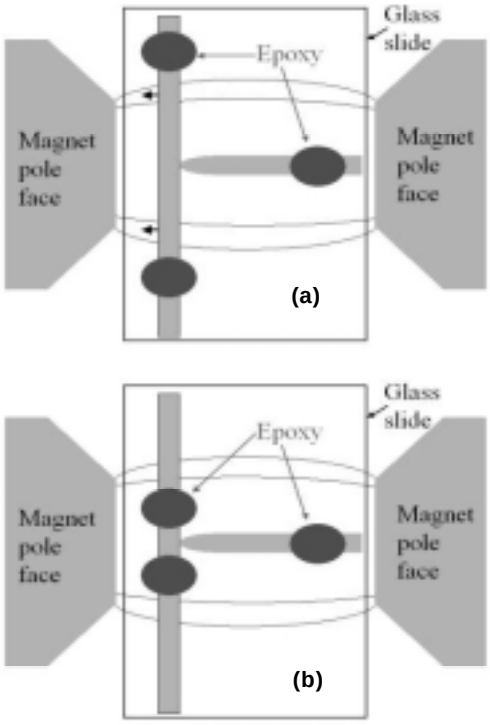

Figure 39 An illustration of two different geometries for permalloy wires that can give differently shaped MR plots due to different artifacts being present.

We note that the magnetostatic force on the transverse wire has the potential to deflect the transverse wire with a far greater distance than the magnetostriction described in Fig. 36 using Ni. To test this idea, measurements were made on Permally samples using the geometry of Fig. 39b, where the transverse wire is mounted in the region of homogeneous field. The resulting data resembles Fig. 37c most of the time and Fig. 38c in certain cases. The infinite MR in Fig. 38c can be explained by elementary magnetostatic and magneto mechanical effects, and not by infinite BMR. The data in Figure 37 and Fig 38 represent three common geometries used in previous reports [44, 49]. Given the similar shapes between Fig. 37 and Fig. 38, it seems that the same forces are at work in both data sets. The principal difference is that in the samples of Fig. 37 the forces were not sufficient to break the nanocontacts, but only sufficient to deform it. In general, the great bulk of our data is more complicated than the representative curves shown. However, it often seems to be combinations of the three generic MR types shown in Fig. 37. It is easy to imagine that subtle differences in sample geometries could produce a wide range of mixtures of the artifacts that produce the three generic curves of Fig. 37. Thus, the conclusion to be drawn from the qualitative similarity of Figs. 37 and 38 is that forces are at work in the geometry of Fig. 36 that can easily mask any true BMR effect, thus making this geometry incapable of providing credible evidence for a real BMR effect.

2.4.2.2 Electrodeposited Fe between thin film patterns

In seeking to design artifact-free experiments that can identify a real BMR effect and potential devices that are feasible to be fabricated, we have investigated ferromagnetic nanocontacts electrodeposited between ferromagnetic and Cu films

anchored on wafers, in which the physical displacement of wires due to the magnetostatic force may be suppressed.

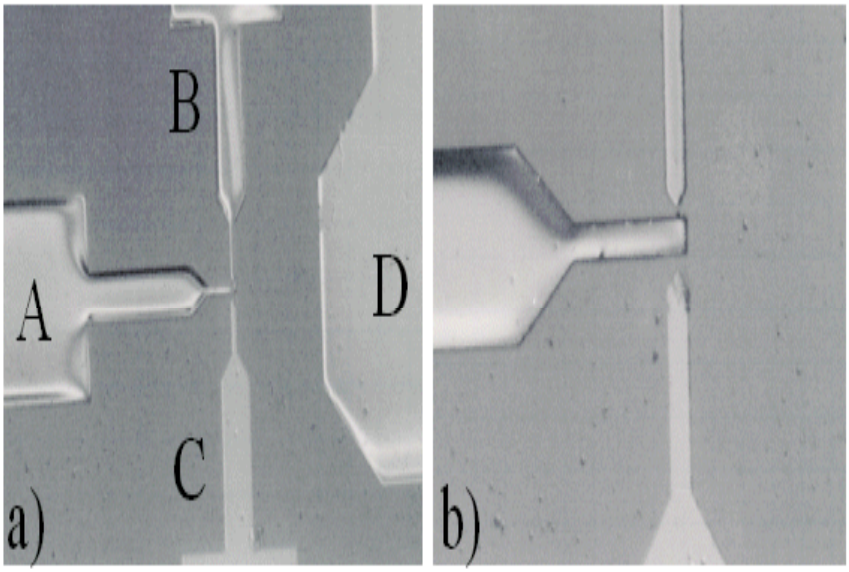

Figure 40 Electrode setup for plating of smooth Ni and Fe contacts are shown in figure a). Electrode A and B are used to form a nanocontact, while electrode C is the reference electrode for the potentiostat. Area D acts as a "bulk" source of metal during the plating process. Figure b) shows a close up of electrodes A, B and C, the gap between the A and B electrodes were varied from 50 to 0.5 μm.

The plating bath for Ni contacts was 1.4 M $(H_2NSO_3)_2Ni$ and 0.5 M H_3BO_3 at pH 3.5 while the plating bath for Fe was; 0.8 M $FeSO_4$ and 0.37 M Na_2SO_4. The contacts were deposited at such plating potential that either a "smooth" continuous film of Ni or Fe was created (1.0-1.5V), Fig. 40, or in the case of Fe, a rather aggregate like Fe film was produced at an elevated potential of –4.0V, Fig 41. Approximately 200 smooth Ni and Fe contacts were made with an initial

photolithograpically defined electrode spacing ranging from 50 to 0.5μm. Figure 42 shows a typical response from a smooth Ni contact exhibiting a ΔR/R of 0.1%. With the Fe solution and the higher plating potential the aggregate like deposits, as seen in Fig. 41, shows ΔR/R values of 10-80% in most cases. The heavy lines in Fig. 41 show the shape of the Cu films underlying a granular deposit of Fe produced with a deposition voltage of -3.8V. Mossbauer spectroscopy shows that the Fe particles are metallic and ferromagnetic. Figure 43 shows a typical MR curve for an aggregate like contact with a ΔR/R of 46%, this curve could be repeated several times with only small variations in ΔR/R between runs. However, upon observing these deposits under an optical microscope it was noted that the Fe particles move as a field is applied.

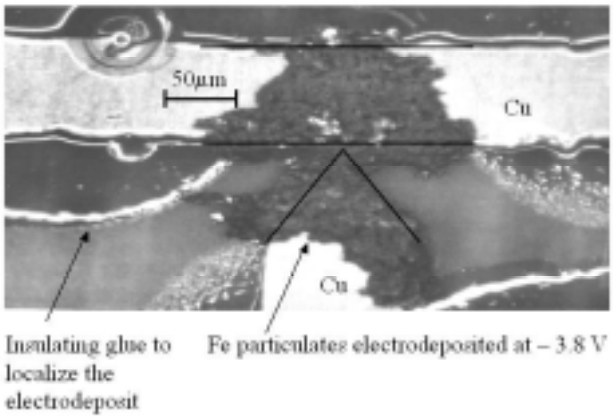

Figure 41 An optical image of the Fe particulate deposit that is found when Fe is electrodeposited at the unusually high potential of -4 V on a gap between Cu films.

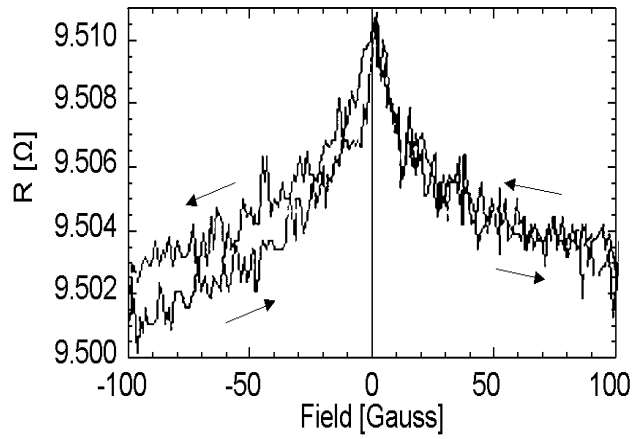

Figure 42 Magnetic field vs. resistivity measurement for a nanocontact formed from a continuous Ni plated film. The field was applied from +1000 to –1000 Gauss, and then in the reversed direction. The change in resistivity is ~0.1%.

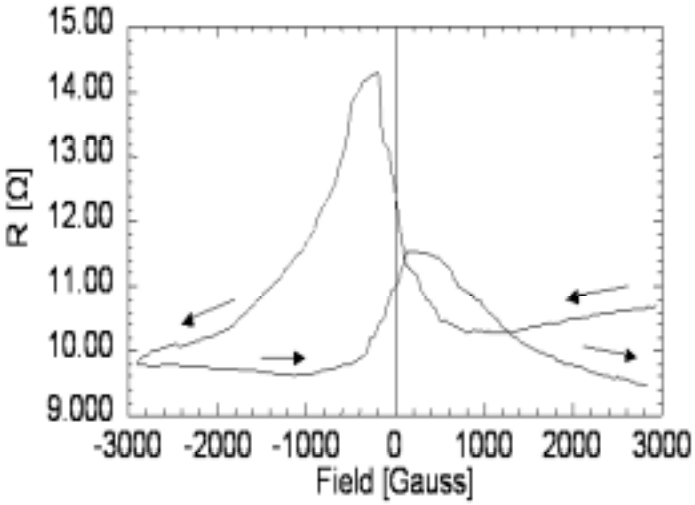

Figure 43 Magnetic field vs. resistivity measurement for a Fe plated aggregate like nanocontact. The field was applied from +3000 to –3000 Gauss, and then in the reversed direction. The change in resistivity is ~46%.

To immobilize the particles in one sample we used a drop of varnish nail polish. Upon hardening, the MR in this sample dropped from 46% to 0.3%. The artifact at work here is illustrated in Fig. 44. When the field is applied and the Fe particles are magnetized in the same direction they clump together like simple bar magnets to create new conducting paths and lower the resistance. Thus, we conclude that the claims of Ref. 49 of tremendous BMR are highly questionable.

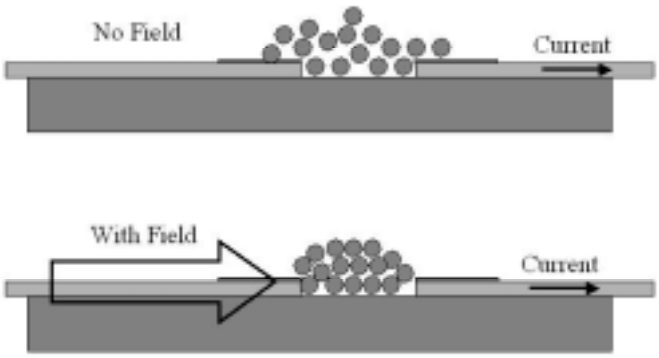

Figure 44 An illustration of the artifact manifest in data on samples like the one in Fig. 41 showing how magnetostatic forces cause Fe particles to clump together creating new conducting paths, lowering the resistance, and producing data qualitatively similar to that in Fig. 43.

2.4.3 Electro-deposition of Ni nano-cluster through pinhole between multi-layer thin films

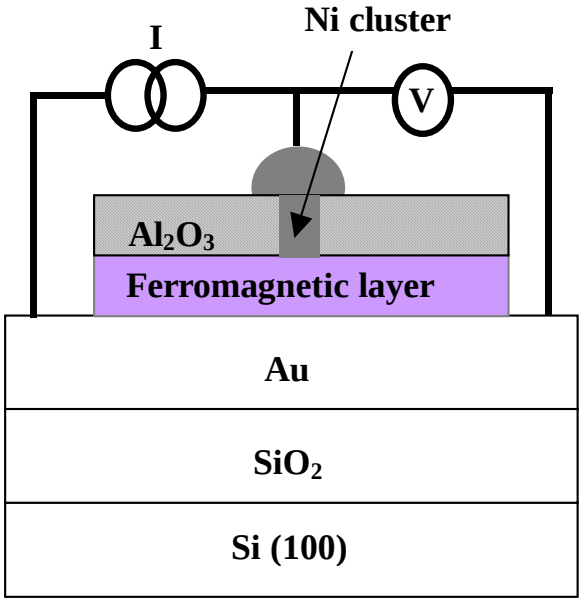

Figure 45 Experimental structure stack and measurement set-up of the pinhole nanocontact.

Having established that the electrodeposition techniques developed by other researchers are prone to artifacts, we proceeded to develop a more sophisticated approach of forming nano-sized metallic junction. In our scheme, we exploit the naturally occurring atomic size pinholes in oxides as the precursors to forming nanocontacts.

Schad et al. [58] have showed that it is possible to grow Cu clusters by electrodeposition on top of aluminum oxide layers deposited on a magnetic thin film (MTF). Their approach is to apply a potential in the electrolyte solution between the electrode and the MTF. The potential causes an electrical arc or breakdown in the

oxide. The breakdown appears to create a pinhole in the oxide, probably in pre-existing thin spots or partial pinholes, and a Cu cluster electrodeposits on the underlying exposed MTF. In the present work, we have used this effect to make pinhole nanocontacts [59], between magnetic metals with the aim of making nanocontacts that exhibit the BMR effect.

The best substrates for the electrodeposition of Ni BMR nanocontacts consist of metallic multilayers such as: Si(100)\thermal oxide\1 nm Ta\100 nm Au\10 nm Ni or Co\ 1 nm Al, with the metallic films deposited in a UHV magnetron sputtering system. The experimental structure is shown in Fig. 45. The purpose of the Au layer is to reduce the lead resistance to a negligible value compared to the nanocontact resistance. The best results are obtained when the Al is oxidized by exposure to air. The electrodeposition is carried out in a solution of 1.5 M $Ni(SO_3NH_2)_2$ and 0.5 M H_3BO_3 at a pH of 3.5. The potential, referenced to a saturated calomel electrode, was -1.5 V for times varying from 5 s to 60 s.

The resistance observed for contact to a single cluster ranges from 0.2Ω to 80 Ω, essentially all of which is attributable to the nanocontact since the lead and contact resistances are negligible. We estimate the cross-section of the contact by assuming that an atom occupies 0.1 nm^2 and that this has a quantum of resistance 12.9KΩ. We obtain values of the contact size between 3.5 and 75nm.

The Ni clusters are randomly distributed on the substrate surface with a mean separation on the order of tens of microns. The close spacing of Ni clusters makes it difficult to make electrical contact to a single cluster. Fig. 46 shows the field-emission scanning electron microscope (FESEM) images of two single Ni clusters.

To assist in making electrical contact to a single cluster we have patterned a photoresist on some samples to open a regular array of holes 5 to 20 micrometer in diameter spaced several mm apart. This way only one Ni cluster is likely to be deposited in the exposed area of the sample at the bottom of each hole in the photoresist. No deposition occurs on the insulating photoresist. Electrical contact to the Ni cluster electrodeposited in the hole is made by attaching a Cu wire to it with silver paint. This method avoids any mechanical stress, which could damage the nanocontact.

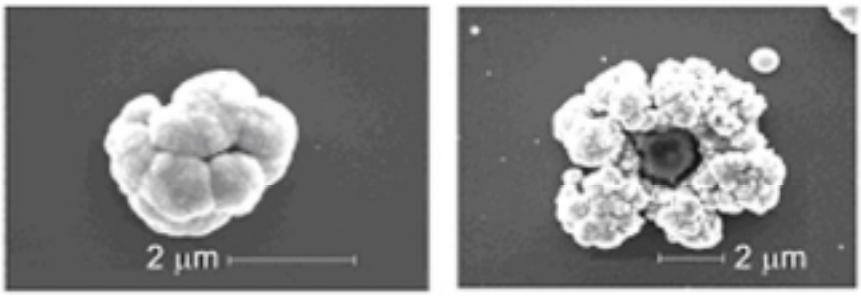

Figure 46 SEM images of two single Ni clusters.

Fig. 47 presents a typical MR loop of Ni cluster nanocontacts. The plot is the magnetoresistance versus magnetic field, which is showing a MR of 14%. The MR effects are similar to the results obtained earlier for nanocontacts electrodeposited between macroscopic Ni wires, shown in Fig. 37a. But in the present geometry, the very small volume of magnetic metal in the present samples could rule out magnetostriction and the thin film structure could rule out the magnetostatic effect. The small MR (compared to BMR) is consistent with the measurements of Pandana et

al. [55], which could be from tunneling magnetic resistance effect when considering the resistance of $Ni/Al_2O_3/Ni$ parallel to the cluster nanocontacts. Because we do not have the information of the actual size, shape and stability of the contact, there is a possible artificial effect arising from instability of pinholes that seem to be concomitant with the oxide thin layers.

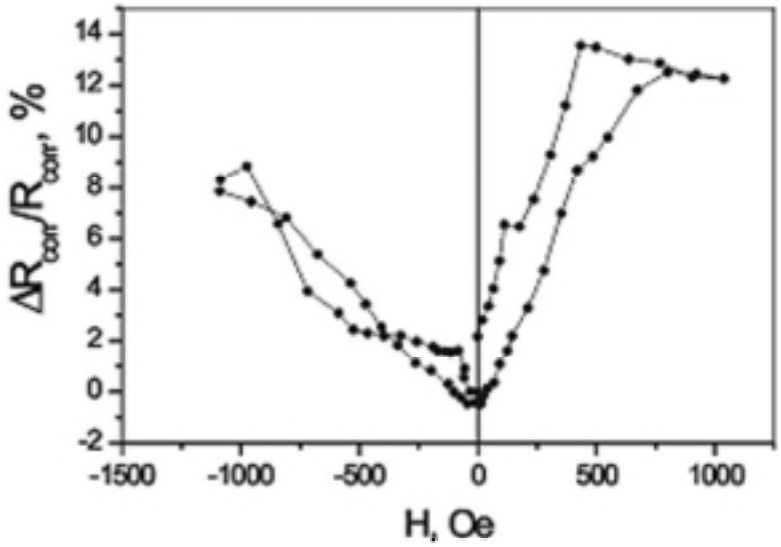

Figure 47 Magnetoresistance versus applied magnetic field curves of a pinhole cluster nanocontact.

2.4.4 Conclusions

To summarize the results of our BMR experiments, we offer the following conclusions:

1) BMR effects could be established between two ferromagnetic wires by using break junction and point contact set-up.
2) Previous attempts to observe BMR effects in electrodeposited nanocontacts have been subject to various artifacts that can mimic BMR effect.

3) For planar experiments with both in-plane and perpendicular electrodeposited nanocontacts, we only found small MR responses when comparing to BMR. This is due to the contact sizes in these experiments that are not small enough to produce atomic contact as achieved in break junction experiments. It requires significant technology advancement to fabricate stable atomic junctions with conductance at a few quanta.

All is not lost, however, as recent reports by Yu and Natelson [60] showed that atomic nancontacts of Au can be produced by confining electrodeposition through an e-beam patterned alumina mask. Unfortunately, this technique requires another set of skills, which are beyond the scope of my work.

Chapter 3: Current-pulse-induced magnetization reversal and domain wall resistance magnetic memory cell

3.1 Conventional MRAM

Magnetic Random Access Memories, MRAM's, are data storage devices that contain a ferromagnetic component that can switch between two stable magnetic states, and retain the state when power is removed. The main advantage over semiconductor RAM is non-volatility, writing speed, low power consumption, radiation/EMI resistance, and manufacturability. Table 1 shows how MRAM compares with various semiconductor memory types in commonly used metrics.

Table 1 Competitive nonvolatile RAM

Memory	MRAM	FERAM	FLASH
Access time (ns)	<60 (TMR)	~40 (TMR)	50
Write time (ns)	<10	$\sim 10^2$	$\sim 10^4$
Repetition circle	$>10^{15}$	10^{12}	10^5
Capacity (bit/Tip)	>1 Gb	<10 Mb	>1 Gb
Power (mW)	<10	>10	~100

MRAM's were pioneered by Daughton [61] at NVE, but IBM and Motorola are currently leading the research in MTJ-based MRAM. Their efforts differ in design and

implementation, but the fundamental governing principles are essentially the same. MRAM may be grouped according to the physics of their operation into three main categories [62]: spin-valves and all metal spin transistors, magnetic tunnel junctions and hybrid ferromagnetic-semiconductor structures. The process of writing data into a cell is the same in all approaches, but reading the cell's contents utilize different magnetoresistance (MR) mechanisms that determine the magnetization state in the ferromagnetic storage element. The choice of reading scheme has profound consequences in manufacturability and reliability.

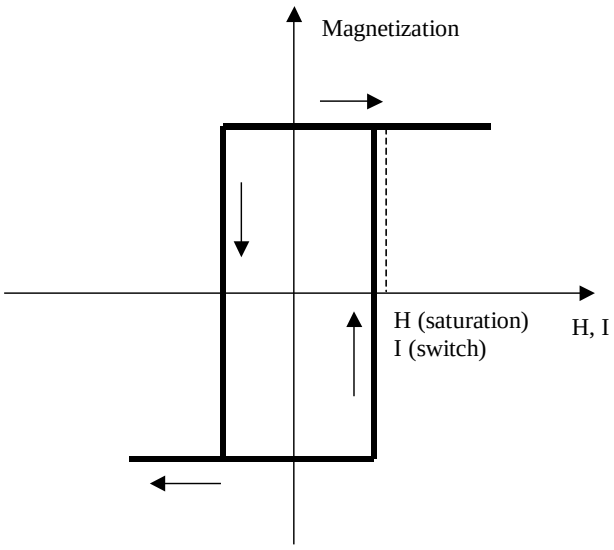

Figure 48 Illustration of the bistable states in a hysteresis loop.

The bi-stable orientation of their magnetic state is a defining characteristic of ferromagnetic (FM) materials and a natural basis for nonvolatile bit storage. For a properly fabricated thin FM film, the two possible states of magnetization can be described by an ideal hysteresis loop shown in Fig. 48. If an external magnetic field greater than the coercivity of the ferromagnetic material is applied, the magnetization will

saturate in the direction of the field. The square shape of the hysteresis loop reflects the "non-volatile" characteristic as the magnetization retains its orientation even if the field is removed. As long as the thermal energy is lower than the stored magnetic energy, the system will persist indefinitely in its state.

Fig. 49(a) is a schematic of an MRAM architecture. Wires fabricated directly over and under the magnetic element perform the writing and reading tasks. Two-dimensional banks of memory cells is created by using a 2-D array of rows (bit line) and columns (word line) of write wires, with each cell inductively coupled to a specific bit-word line combination. To switch a given cell, both wires are energized so that each line creates a field half the coercivity of the element. Only the cell defined by the bit-word lines is affected while leaving the other cells unperturbed. Fig. 49(b) illustrates the reading process of a typical MTJ based MRAM cell. The bottom ferromagnetic film is constructed to have a larger value of switching field than the top film, and it is the orientation of this film that encodes a '1' or '0'. Reading the stored value in a cell is done by interrogating the cell with a sequence of low power pulses, sufficient only to switch the state of the top FM layer. The resistance of the cell is monitored by measuring the voltage across the element in a fixed sensing current. A sequence consisting of first a positive and then a negative current pulse is transmitted to the word line. The associated magnetic field flips the magnetization of the upper magnetic film, first to the left and then to the right. For a stored binary "0" this corresponds to a sequence where the relative orientation of the top and bottom FM layers switch from antiparallel to parallel during the pulse. The voltage waveform in this case will be a relatively high positive voltage

followed by a relatively low negative voltage as drawn in the figure. If the bit stored is a "1", the response waveform is reversed.

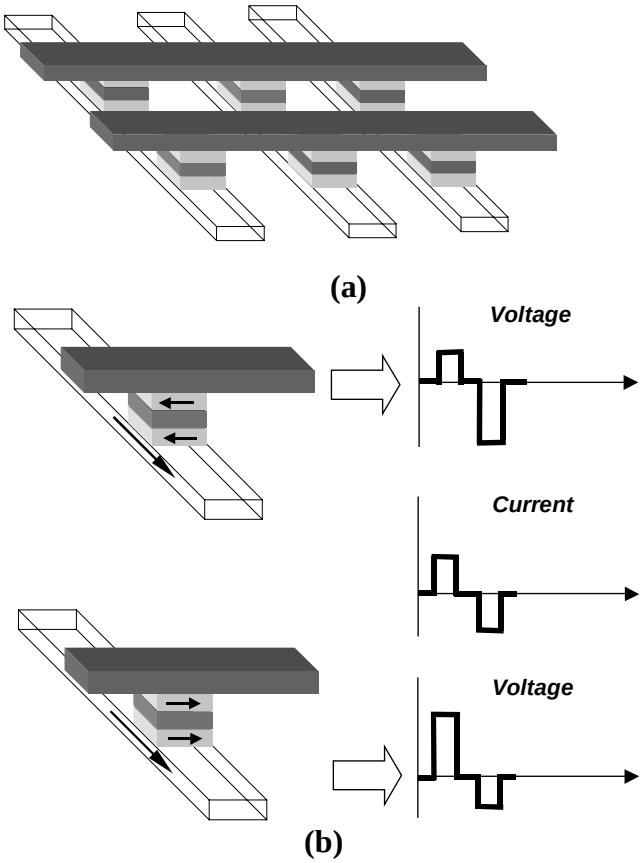

Figure 49 (a) MTJ memory cell design architecture. (b) An illustration of reading process in an MRAM cell.

3.2 Novel effects for new MRAM implementation: current-domain wall interactions models

In the previous section, we saw that the orientation of the storage layer is defined by an external field from an ancillary current wire. Unfortunately, the switching field distribution ΔH_{SW}, i.e. the spread of coercivity fields across the device, is difficult to

control. As the switching often involves domain nucleation, it is sensitive to variations in morphology and chemistry at the atomic length scales. Thus, an ensemble of islands could have very broad switching fields, which presents a formidable design problem in ensuring that only the intended cell is affected by the write current. For this reason, a great deal of work is being done on developing alternative schemes to switch the magnetic states of memory elements. One approach is the recently proposed voltage controlled rotation (VCR) [63] in a ferromagnetic/spacer/insulator/ferromagnetic multi-layer system. The magnetic coupling between two ferromagnetic layers oscillate from antiferromagnetic to ferromagnetic by an applied bias voltage, and by a judicious application of voltage across the insulating gap, the magnetization direction of the system can be switched and rotated. While theoretically plausible and experimentally appealing, the fabrication requirements appear to be quite stringent. Alternative methods tat hav been proposed of late employ passing an electrical current through one or both FM layers. One method was developed for sub-micron size dots, where the magnetization reversal by spin-transfer was predicted by Slonczewski [64] and Berger [65], and was confirmed by experiments on multilayered pillar structures [66]. It involves direct spin injection perpendicular to a multilayer film to produce a "spin-torque" to locally switch the magnetization of one of the layers. The other approach is for single layer magnetic thin film patterns consisting of domain patterns which can be moved to wards specific directions by current pulse, and subsequently impart a pattern reconfiguration. In this work, we are interested in studying the latter method and demonstrating its efficacy in storing data.

To appreciate the principles of current-induced magnetization reversal, we briefly review some concepts in domain-drag theory. We recall that magnetic domains, i.e., areas of constant magnetization, form in FM films in order to reduce the total magnetostatic energy. Within the domain walls, the region that separate neighboring domains, the spins change gradually over a number of lattice sites. When an external field is applied to the material, a non-zero torque is exerted on the wall spins. This tends to align the magnetic moments of the wall spins with the applied field, which is equivalent to a translation of the wall center along the direction normal to the wall plane. This is the classic mechanism that governs magnetization reversal and saturation. However, a somewhat arcane but nevertheless interesting way to move domain walls is a process known as "domain drag." In this approach, current through the ferromagnetic material exerts an electron pressure on the domain walls which leads to domain wall translation. This is independent from the "global" magnetic field generated by the current, and domain wall translations are accomplished at far lower currents than required to generate fields above the local domain coercivity [67]. The exact nature of the electron pressure can be understood by two models of interaction between an electric current and a domain wall which we discuss below, which for completeness, also includes the force associated with the global field.

(a) s-d Exchange Force [68]

The s-d exchange force is associated with the interaction between the 3d electrons in the metallic ferromagnetic materials and 4s electrons in the conduction band of the material. When the 4s electrons travel across a domain wall, the spins flip 180 degrees to align with the local exchange field. As a result of momentum exchange, the spins of the

3d electrons inside the domain walls are canted leading to the displacement of domain wall. Thus the domain wall displacement is always in the direction of charge carriers, i.e., in the opposite sense of the current. See Fig. 50. The s-d exchange force per unit area of wall by normal current is

$$F_x = 2M_s \mu_i^{-1} (\beta_1 R_0 j - v_w) \qquad (3\text{-}1)$$

where M_s is the saturation magnetization, R_0 the ordinary Hall coefficient, j the current density and v_w the wall speed. μ_i is the intrinsic wall mobility and β_1 is a dimensionless correction factor of order unity.

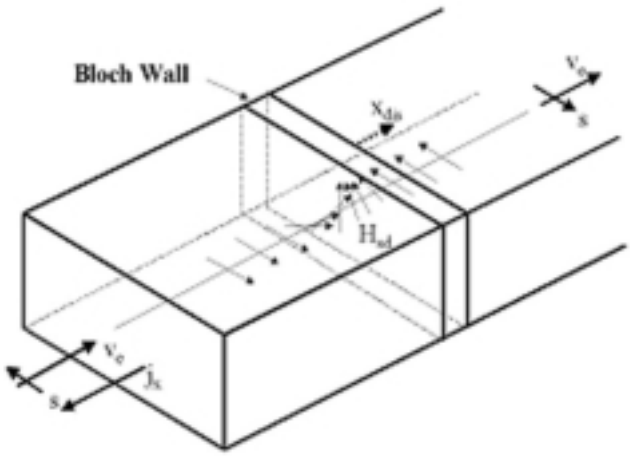

Figure 50 Illustration of s-d exchange model: the spins of 4s electrons flip to align with the local exchange field. As a result of momentum exchange, the spins of 3d electrons inside of domain walls are canted leading to the displacement of domain walls.

(b) Hydromagnetic Domain Drag Force

Hydromagnetic domain drag force is based on Hall effect and magnetoresistance within magnetic domain. A DC Eddy current loop caused by the Hall effect runs around each wall. The induced magnetic field by these loops tends to drag the whole domain in the same direction regardless of the direction of in-plane magnetization. See Fig. 51. The domain drag force per unit area of wall by normal current is

$$F_x = 2M_s\mu_e^{-1}(R_1 j - v_w) \qquad (3\text{-}2)$$

where M_s is the saturation magnetization, R_1 the anomalous Hall coefficient, j the current density and v_w the wall speed. μ_e is the eddy current limited wall mobility, which is expressed as $\mu_e = \pi^3\rho/8.4wM_s$ when the sample thickness is much smaller than the wall spacing.

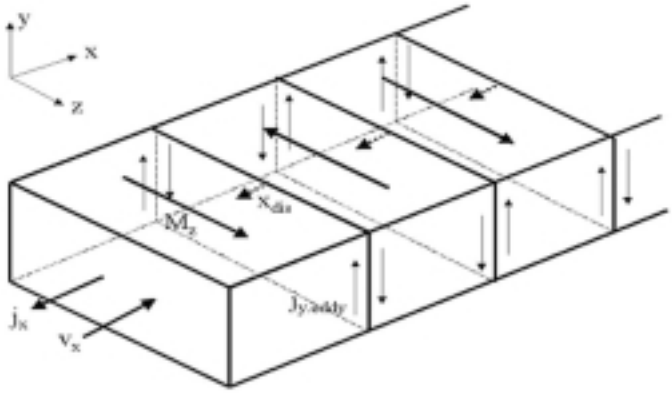

Figure 51 Illustration of domain drag force model: The sample with rectangular cross section, where domain walls normal to the current. When the current crossing the wall, a component in *y* direction is generated because of the Hall effect.

(c) Global Field Force

The electric current through the sample produces a circumferential magnetic field, which runs in closed loops perpendicular to the direction of current. The magnetic field component along the loop has opposite signs at the top and bottom of the film and its magnitude is proportional to the distance from the center of cross section of the sample. The global field thus exerts torque on the wall causing an S-shaped distortion of a Bloch wall. During the process, the current accumulates kinetic energy and momentum into the wall and the kinetic energy is dissipated during ballistic wall motion after the end of pulse. The global field force makes adjacent walls move in opposite directions. We note that the walls do not move when the current density is uniform because the net force on the walls vanishes. See Fig. 52.

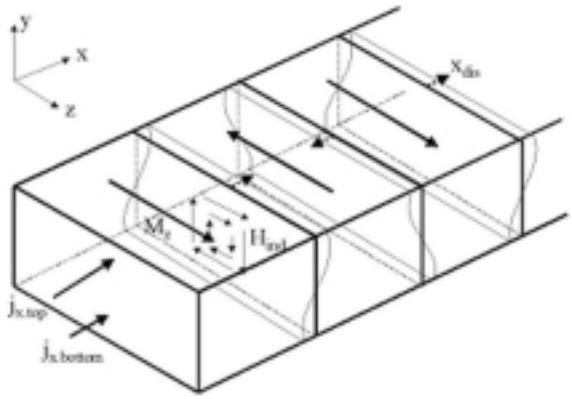

Figure 52 Illustration of global field model: the global magnetic field exerts torque on the wall causing S- shaped distortion of Bloch walls.

3.3 Current-pulse induced domain wall motion observed by MFM

Extensive investigations of domain drag phenomena have been carried out in the 70's and 80's [69]. These were motivated by technologically important issues of that time, namely, Bloch line memories, electromigration in ferromagnetic films, and AMR sensors. The domains were observed using Bitter powder and magneto-optical imaging techniques. However, because of the lack of a high resolution imaging technique and partly due to the rarity of photolithographic and sophisticated sample preparation techniques for patterning, those experiments were confined to large continuous films. Thus, those previous studies ignored size effects and the results were validated only for bulk systems. Furthermore, since the current density required to induce wall motion is so high (10^{11} A/m^2), the experiments needed high current power supplies that were deemed impractical for device applications.

As dimensions shrink, the intrinsic magnetization pattern dramatically changes. The domain configuration is established by the minimum of the total energy of the system. Hence, the domain patterns of bulk continuous films, which ignore the magnetostatic energy contribution from the edges, is expected to be quite different from that of a small lithographically-defined magnetic structure.

3.3.1 Experimental set-up

To investigate domain drag phenomena, structures were fabricated by using conventional photolithography. Positive photoresist was spin-coated on Si substrates (with native oxide) and exposed using a contact mask aligner. One set of patterns were 20 μm wide rectangular strips with variable length from 100 μm to 300 μm, and a second set

had a "bow-tie" geometry with the same interior geometry but with large flared ends. After development, the substrates were placed in a high vacuum system and evacuated at 1 x 10^{-5} Torr. NiFe films were deposited by thermally evaporating $Ni_{84}Fe_{16}$ pellets on a resistively heated tungsten boat. The background pressure was $3x10^{-5}$ Torr and the deposition rate was kept at 10Å/s. No external magnetic field was applied during deposition process. The film thickness varied from 100-160nm. The photoresist was subsequently lifted-off, leaving behind the NiFe structures. Thin (~25 μm) gold wires were connected on both ends of the islands using silver paint, which provided the electrical connection to our pulse generator (seen Fig. 53) The nominal DC electrical resistance of the pattern is about 40-70Ω. The current pulses were generated by a 5nF capacitor charged up to 100V and switched to discharge through the sample. The pulse shape, as monitored using a storage oscilloscope, had better than 10ns rise time and an exponential decay on the order of 1 μs. The magnetic domains were imaged after every pulse by using a large platform magnetic force microscope. We discovered that the reliability against electrical breakdown during pulse experiments was greatly improved by going to the bow-tie structure. Presumably, the contact area is much larger in this case, which reduced the mechanical stress due to the paint and consequently enabled larger current densities to be applied.

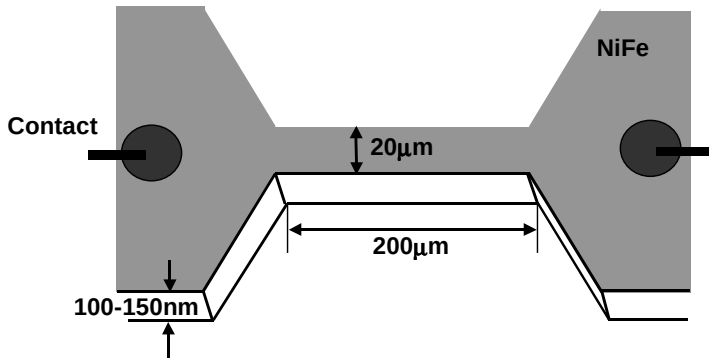

Figure 53 The dimensions of NiFe patterns in the experiment.

3.3.2 Current-induced domain wall motion: Results and discussion

Figure 54 shows a sequence of MFM images of the same area of the strip. Also shown is a high-resolution detail of a domain wall (Fig. 54 d). The domain walls are clearly visible in all the islands, and from which we can deduce the magnetization of the domains. The interior regions are comprised of alternating magnetization patterns oriented nominally at 20^{o} to the strip. The triangular features near the edges are the ubiquitous closure domains whose magnetizations are parallel to the edges to reduce magnetostatic energy. The film's thickness ranged from 100nm to 160nm so that the walls are expected to be Bloch or asymmetric Bloch walls, rather than Neel walls. This is confirmed by considering the zoomed image in Fig. 54(d). The contrast changes polarity twice along the wall without crossties, which precludes the possibility of Neel type wall. Additionally, the contrast variation [70] and line profiles are consistent with those expected for 180^{o} Bloch walls [71].

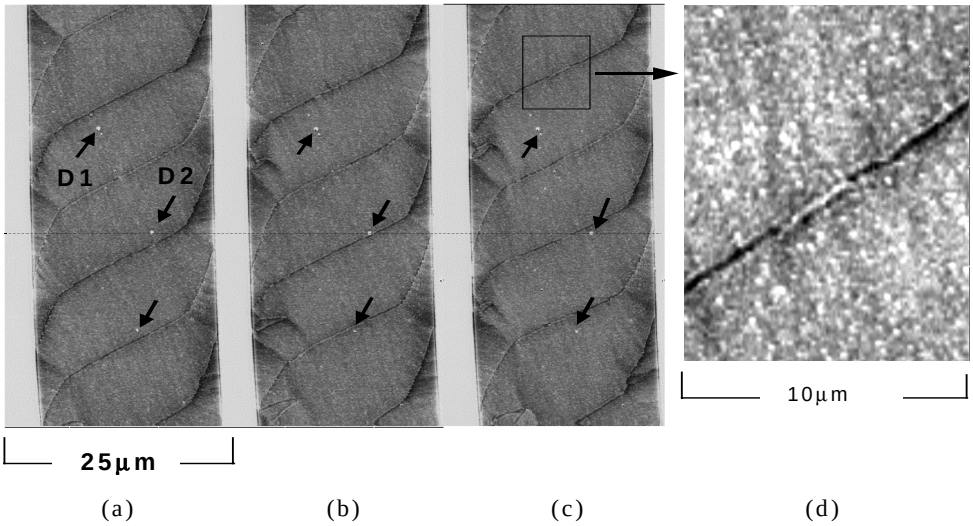

Figure 54 A sequence of magnetic domain propagation with successive current pulses. 40µm x 25µm MFM scans of the same area of the surface at (a) the initial states, (b) after one pulse and (c) after two pulses. Arrows are drawn to highlight topographic defects to serve reference points for domain motion. The current direction is down and the domain walls move in the opposite direction. (d) zoom-in image of a segment of a Bloch wall.

Figures 54(a) to (c) were selected from a series of numerous successive images of the same area, with one pulse applied between each consecutive image. The motion of the walls is best seen by noting the relative displacements with respect to the fixed topographical defects. As a guide to the eye, we placed arrows on three topographical defects as reference points. A line is drawn to connect the middle defect on the three images. It is clear that all walls are displaced by an average distance of 0.85 µm in the same direction. Moreover, the triangular edge domains themselves move in concert with

the interior walls, suggesting that the effect of the current pulse is to propagate entire domains. In this particular sample, a current density of $2.5x10^{11}A/m^2$ was used and the current flows from top to bottom. Hence, the direction of the wall motion is opposite to the conventional current direction, or the same as the drift velocity of the conduction electrons. More importantly, we established that the direction of domain wall motion can be reversed by switching the current polarity. These observations are true for all samples investigated, despite some differences in the critical current density. In general, wall displacement occurs when a critical current density at the order of $10^{11}A/m^2$ is reached.

Neglecting eddy currents, viscous, pinning and other hysteretic effects, there are three major theories for magnetic domain wall displacement by current pulses. The first mechanism is hydromagnetic “domain drag force”, based on Hall effect and magnetoresistance within magnetic domain [69]. The force is expected to push walls in the same sense as the conventional current if the anomalous Hall coefficient of the ferromagnetic material is positive, and vice versa. Furthermore, it is proportional to the sample thickness and tends to zero with decreasing sample thickness. The second mechanism is the "s-d exchange force", associated with the interaction between the 3d electrons in the metallic ferromagnetic materials and 4s electrons in the conduction band of the material [67]. The domain wall displacement is always in the direction of motion of charge carriers, i.e., in the opposite sense as the conventional current. Unlike the domain drag, the exchange force is independent of the sample thickness. The third mechanism is caused by the “global field” [72]. The global field exerts torque on the wall, causing an S-shaped distortion of a Bloch wall and making adjacent walls move in opposite directions. In our experiments, the nominal direction of motion relative to the

current is contrary to the predictions of the global field theory. Both the "hydromagnetic domain-drag" and the "s-d exchange" models predict motion in one direction. The direction of the wall motion due to domain drag is dependent upon the anomalous Hall coefficient, R_1. The only possibility for domain drag to be consistent with the sense of the observed wall motion is for R_1 to be negative. If R_1 is negative and the hydromagnetic drag is dominant, then the theory predicts that the force is dependent on the sample thickness vanishing for zero thickness. However, we find that experimentally, the thinner films exhibit larger displacements for similar currents, which is opposite to the effect predicted by the domain drag. Therefore, we must conclude that, in our films, the s-d exchange is the dominant mechanism. Using the established models [67, 69], we can calculate the critical thickness beyond which the domain drag will become dominant.

$$w_c = \frac{\pi^3 \rho \beta_1}{8.4 M_s \mu_i} \times \frac{R_0}{R_1} \qquad (3\text{-}3)$$

where ρ and M_s are electrical resistively and saturation magnetization of Permalloy sample, μ_i the intrinsic wall mobility and β_1 a dimensionless correction coefficient of order unity. R_0 and R_1 are normal Hall constant and anomalous Hall constant respectively. Using the typical material data in [73] and [74], we find that the critical thickness is ~1μm for our Permalloy sample. This implies that s-d exchange is expected to be dominant for very thick samples. Establishing that the mechanism is s-d exchange is quite important for device applications. Since the force is independent of the sample thickness, it is possible, and in fact easier, to move domain wall for very thin samples. The thickness dependence of the s-d exchange force and hydromagnetic drag force was illustrated in Fig. 55.

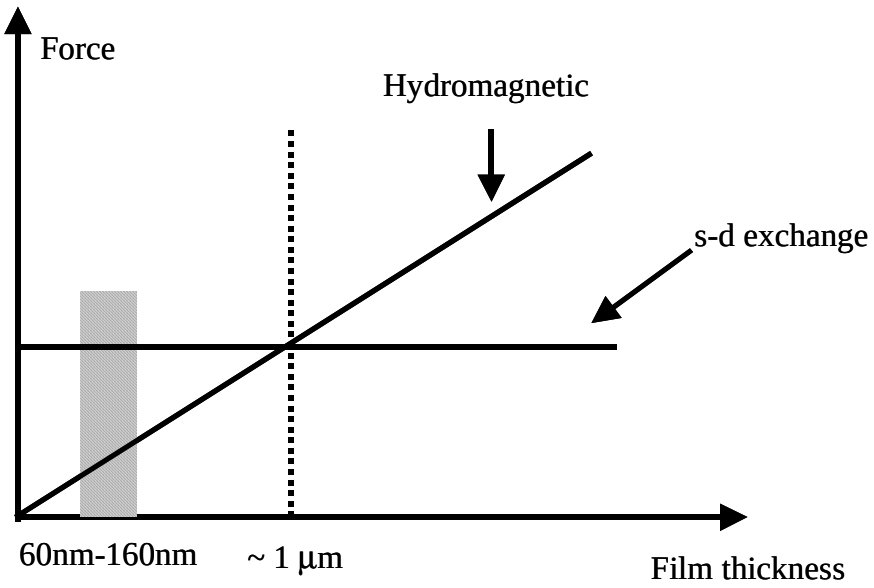

Figure 55 Thickness dependence of the interaction forces between domain walls and current pulses. Our samples are at the thickness ranging from 60nm to 160nm. When film thickness is smaller than 1μm, s-d exchange force is the dominant force.

From the domain wall motion, we can say that the motion of the domain wall is rather complex and does not have a simple relationship with the number of pulses. To illustrate this point, we plot in Fig. 56 and Fig. 57 the positions of domain walls of #1111 with respect to the defects D1 and D2. The two curves show the walls are nominally translated the same direction with an average displacement of 0.85 μm per pulse. However, the domain propagation is non-linear. This is evidenced in Fig. 56, where walls move faster and more coherently in 2nd to 5th pulses and are somewhat retarded in the latter pulses. Similarly, we also observed that there are specific cases when segments of

the walls do move in the same direction as current. An example is the movement of wall W5 after pulse 1 where the displacement measured relative to the left defect (D1) is negative while the motion relative to D2 is positive. Similar events can be seen for W4 at pulse 6 and W5 at pulse 8. These nonlinear phenomena are perhaps a manifestation of the hysteretic effects of wall motion, along with domain wall pinning attributable to local variations in the chemistry.

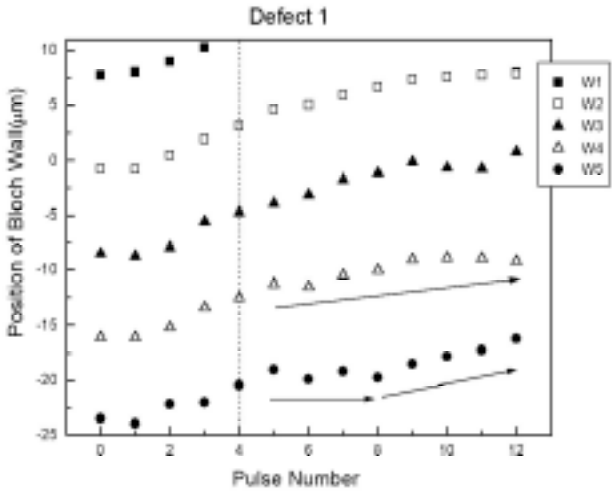

Figure 56 The domain wall positions with respect to the left defect when applying current pulse current pulses through the sample shown in Fig 54. The top wall in the Fig. 54 is noted as W1, The second top wall as W2, so on.

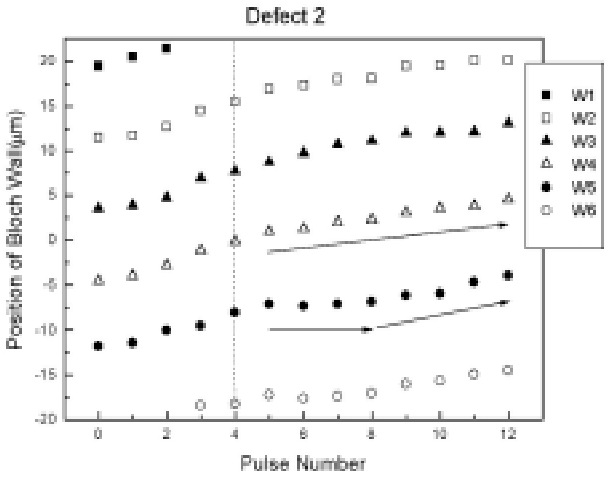

Figure 57 The domain wall positions with respect to the right defect when applying current pulses through the sample shown in Fig. 54.

3.4 Current-pulse induced domain switching [75]

In the previous chapter we observed the domain wall motion can be implemented in a long NiFe strip line. The length of the pattern is much larger than the width so that many possible configurations can exist. However, as was studied by my predecessors, H. Koo, in the case of a low aspect ratio sample, the number of stable domain configurations is also limited. It was also discovered that with judicious choice of pattern geometry, two bi-stable states can set by current pulses with opposite polarity.

The domain configuration of permalloy mainly depends on a lateral aspect ratio of pattern. In a small rectangular NiFe thin film island, the number of possible domain configurations at remanence is finite. When the aspect ratio is near two, the remanent states predominantly are the seven or four domain configuration. Figure 58 shows the two

possible stable states i.e. 7D and 4D configurations using a NIST micromagnetic simulator when the aspect ratio is two. The micromagnetic simulators are notorious for being highly sensitive to the starting conditions. However, we observed after repeated calculations involving different initial configurations that the total energy reaches a local minimum at both states. When the aspect ratio is increased slightly higher than two, the 7D structure appears to be energetically more favorable. Similarly, owing to limitations in lithography, the shape of real structures contains round corners. The net effect is the creation of vortex-like patterns at the edges, but the stable states are still a 4D or 7D configuration.

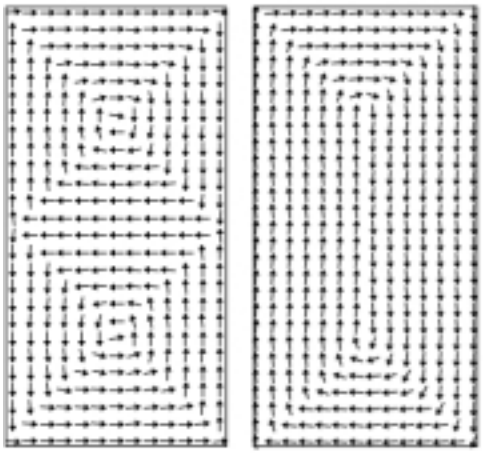

Figure 58 Micromagnetic modeling of two low energy states. This pattern has either 4 or 7 domain configuration.

The experiment is shown in Figure 59, where (a) shows the geometry of the patterns. MFM images were obtained after applying single-shot current pulses through the material. Figures 59 (b) and (c) are the two observed configurations of the islands at a zero-applied field. The 7D configuration shown in Figure 59 (b) was observed prior to

application of any external stimuli. This state changed into the 4-domain configuration shown in Figure 59 (c) after applying a single pulse of current density -4.25×10^{11} A/m^2 for 10 ns. The minus sign means the current is applied upward. More importantly, the four domain structure reverted back into the seven domain configuration in Figure 59 (d) after applying a single current pulse of density 3.65×10^{11} A/m^2 but with opposite polarity. Note that Figures 59 (b) and (d) are essentially identical with each other. Many experiments on several islands have shown following general characteristics:

1) A critical current density is required to change state, below which no reorientation can be achieved regardless of the number of pulses applied.
2) Once reoriented, succeeding current pulses of the same polarity and magnitude have no further effect.
3) The critical current density is nearly the same for all islands of similar geometry, but increases with aspect ratio.
4) There are only two states observed, with specific chirality of the closure pattern.

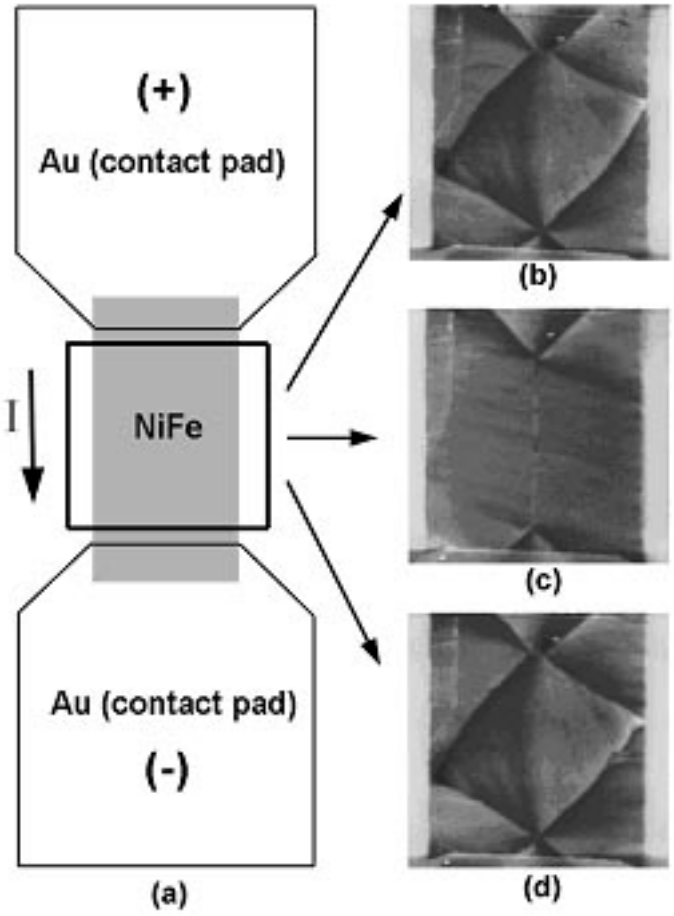

Figure 59 Bi-stable domain configurations of 8.3 μm × 17 μm × 100 nm NiFe pattern (a) Schematic diagram of pattern with contact pads and MFM image (b) of the as-prepared, 7 domain closure, (c) after current application of a 10 ns pulse with density – 4.25 × 10^7 A/cm^2, forming a 4-domain closure, and (d) after current application of a 10 ns pulse of density + 3.65 × 10^7 A/cm^2.

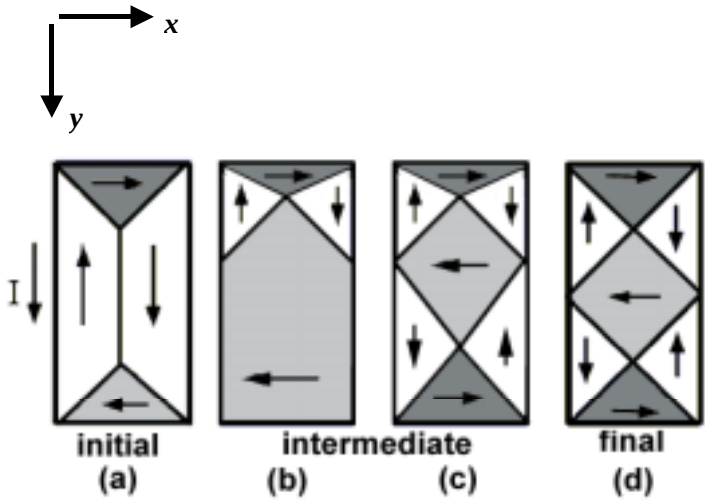

Figure 60 Schematic diagram of the dynamics of domain wall motion for the 4D to 7D transition.

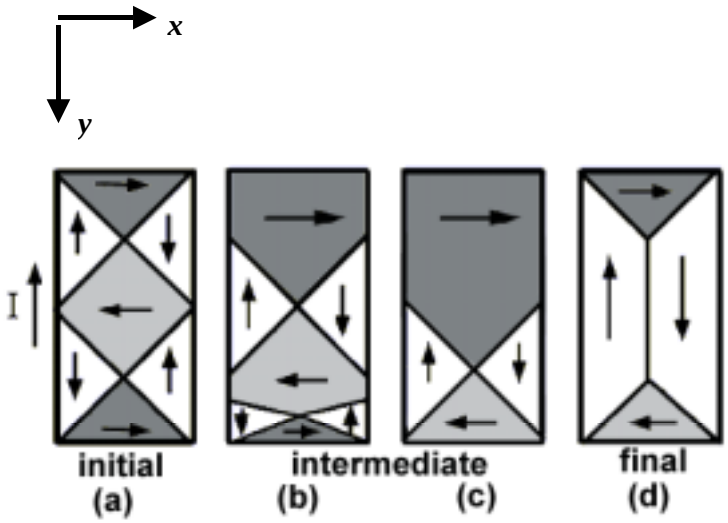

Figure 61 Schematic diagrams of the dynamics of domain wall motion for the 7D to 4D transition.

This process can be explained by using s-d exchange force model, which predicts a current moving the domain wall in the opposite direction. During the application of the pulse in the direction shown in Figure 60, the 90^{o} walls experience an upward force. The

intermediate state during the pulse is similar to the schematic of Figure 60 (b), where the bottom domain expands at the expense of the upper domain. Since the magnetostatic energy increases with domain size, the system has to relax into an energetically favorable configuration. As illustrated in Figure 60(c), this causes a breakup of the large domain via the formation of new near 90^o closure structures at the bottom edge such that the magnetization of the bottom domain is along the induced uniaxial anisotropy (+*x*) direction. The final configuration is attained upon relaxation to ensure that the domains are commensurate with the 90^o wall boundary. On the other hand, a 4D configuration can be achieved by a current pulse of opposite polarity with a similar density. The process is illustrated in Figure 61. Downward forces act on all walls and cause the central domain to be displaced towards the bottom and eventually annihilate the original closure structure. This leaves behind a large upper domain, which is oriented parallel to the induced anisotropy. In contrast to the previous case, it does not subdivide into smaller domains because of the higher energy cost to create domains antiparallel to the induced anisotropy.

3.5 Domain wall resistance and an 8-bit memory cell

3.5.1 Observation of two resistance states in bi-stable magnetic domain configuration

The starting point is the design of a single cell using Permalloy structures and monitoring the magnetic images and corresponding resistances after applying current pulses. A schematic of the experiment set up for a single element is shown in Fig. 62.

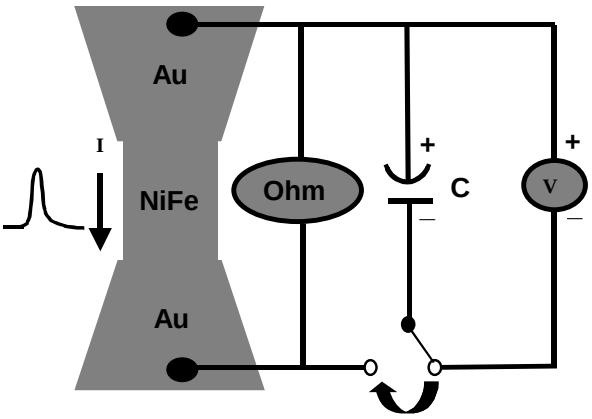

Figure 62 Schematic of pulse-current induced domain reconfguration experiment set-up.

We fabricated rectangular $Ni_{81}Fe_{19}$ patterns on Si substrate (with native SiO_2) through lift-off process. The $Ni_{81}Fe_{19}$ islands have thickness of ~ 100nm and lateral dimensions of 8μm x 16μm. Gold contact pads were deposited on the two ends of the $Ni_{81}Fe_{19}$ patterns that were wire bonded to gold pads to provide electrical connection to the pulse generator. A 7-digit multimeter was connected across the islands. MFM images were taken after every pulse applied through the pattern and were correlated with the simultaneously measured resistance.

Fig. 63 shows three MFM images of the domain structure at the initial state and after applying two current pulses. The initial state shows 10 domains that comprise a 13-domain closure state. The other domains are invisible since they are buried by the gold contact pads. After applying a current pulse in *upward* direction, the resulting pattern is shown in the middle image. It consists of a 7D state, which presumably formed as the central domains consolidated into a larger "spade" domain. This pattern is stable against successive pulses in the same polarity. More importantly, the configuration is reversible.

The domain pattern after applying a current pulse in *downward* direction of same density, shown on the right, is essentially the same as the original state.

The fact that the transition in these patterns are different from the 7D-4D patterns obtained by Koo is not surprising since the dimensions, method of preparation and contact pad alignments are somewhat different in the present case. Nevertheless despite this difference, the bi-stability characteristics are identical.

As in the earlier treatment, we assume that s-d exchange is the dominant force responsible for domain wall motion opposite to the current direction. This effect and the requirement of energy minimization we offer an account of the switching dynamics illustrated in Fig. 63.

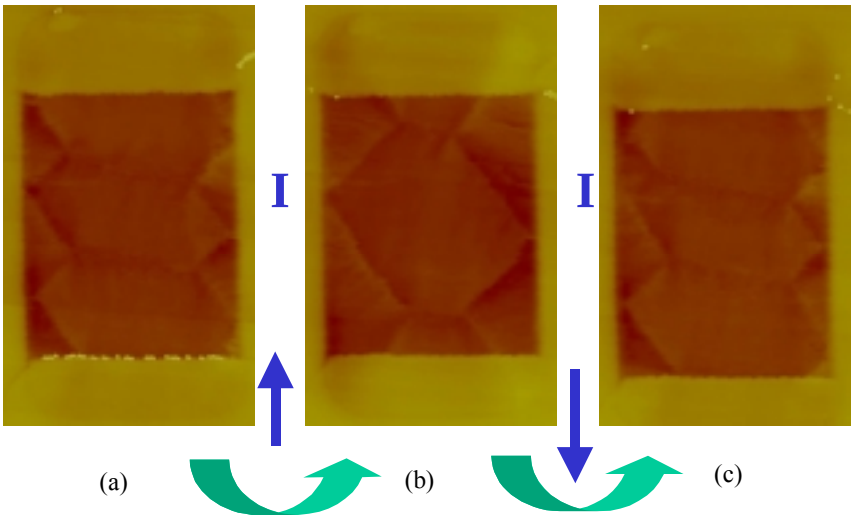

Figure 63 MFM images of the NiFe one 8μm by16μm pattern. (a) is the Initial domain configuration. After applied one upward current pulse, the domain structure switched to (b). Applied another current in downward direction, the domain structure switched to (c) that is same as state (a).

Consider scenario I, the transition from 7D state to 13D state with downward pulse. When the current pulse is in the direction from top to bottom, domain walls move upward. This causes domain 2 in the initial 7D state to expand, which subsequently breaks into new domains 2 and 3. Domain 3 itself further divides into domains 3 and to reduce the magnetostatic energy. The postulated intermediate states are drawn in Fig. 64. These are of course meta-stable states lasting no more than a few tens of nanoseconds during the pulse and thus could not be imaged using the MFM. Only the final 13D state is directly observed by MFM. In the reverse scenario (13D state to 7D state with upward pulse), the domains 3 and 4 are presumably annihilated, thus leaving domains 1 and 2. An interesting point is that when the domains have undergone a transition, further pulses in the same direction do not cause further transition. This is initially surprising since symmetry arguments would predict that further pulses on the same direction would simply alternate the configurations. The fact that this is not observed suggests that there is an effective unidirectional anisotropy that the breaks the symmetry. In other words, the system favors domains oriented along a specific direction. We believe that this extra term is provided by the global force created by the gold contacts on top of the patterns. In the case of the 7D pattern, application of an *upward* current will induce a field parallel to the magnetization of the end domains. This will thus help in stabilizing the end domains against annihilation or the breakup into multiple domains. By contrast, in the 13D case, a *downward* current produces a field that opposes the end domain magnetization, which consequently favors the formation of multiple interior domains.

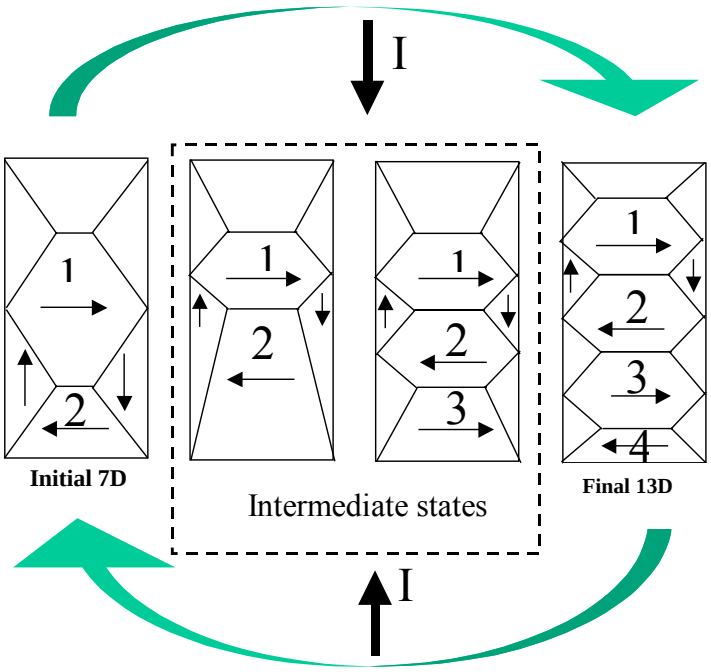

Figure 64 Schematic of domain evolution by applying a current pulse.

In addition to MFM images, we also monitor the resistances of the samples and look for the relationship between domain structures and resistances. The resistances of two domain states are listed in the Table 2. While the resistance difference is about 0.02Ω over 10Ω, it is clear that the final (13 D) state has smaller resistance than the initial (7 D) state in each sample. A typical spread of resistance fluctuations is shown in Fig. 65 as we oscillated between the two states (domain configurations) using alternating current pulses.

Table 2 Resistance states of NiFe patterns

Pattern No.	R (Initial)	R (Final)
1	15.539Ω	15.523Ω
2	14.325Ω	14.314Ω
3	14.291Ω	14.283Ω
4	14.261Ω	14.252Ω
5	13.273Ω	13.266Ω
6	13.265Ω	13.257Ω
7	13.247Ω	13.240Ω
8	10.492Ω	10.501Ω
9	9.868Ω	9.855Ω
10	9.853Ω	9.848Ω

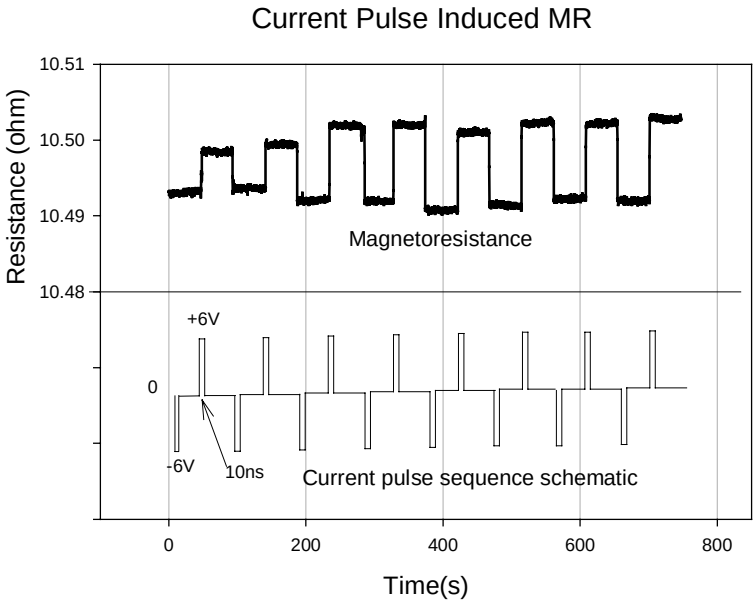

Figure 65 Resistance bi-states changing by applying current pulses in alternate directions.

By comparing the MFM and resistance measurements in several samples, we conclude that:

- Two clear states of resistance are observed after applying current pulses in different directions.
- The bi-stable magnetic domain configuration corresponds to the current pulses in different direction and is associated with the two resistance states.
- The lower resistive state is always associated with the domain structure with more transverse domain walls.
- The domain configuration switching between two states only occurs when the current pulse density exceeds a certain threshold value, here it is ~10^{11}A/m^2.
- Additional current pulses in the same direction does not change the domain structure and resistance.

3.5.2 Theory of domain and domain wall resistance

Let us now examine the theories that could lead to measurable resistance changes in our samples. The origin of resistance difference between two configurations is rather complex, may come from both domain wall resistance and domain resistance [77]. As we discussed in previous chapters, domain walls (DWs) are interfaces between uniformly magnetized regions (domains) with different magnetization directions. Early experiments started from using a small field to erase DWs in a multidomain state and produced large changes in resistivity at low temperatures (a reduction of the resistivity by an order of magnitude at 4 K) [78]. In contrast, within a DW, the material is (1) chemically homogeneous and (2) magnetization varies on a larger length scale—the domain wall

width. These two factors distinguish the physics of electron transport through a DW interface from that of a magnetic interface in a metallic multilayer. Nevertheless, there is a common thread: the electron spin direction changes on crossing a magnetic interface. Thus, as in GMR, spin dependent electron transport effects are expected to be important to understanding the scattering of electrons by DWs.

3.5.2.1 Domain wall resistivity

At present, the exact nature of domain wall resistance is highly controversial, and there is hardly any agreement in the magnitude and sign of the effect. However, for the purposes of completeness, we briefly review the important theories that predict positive and negative effects. The three widely cited models that predict a positive domain wall resistance are those of Cabrera and Falicov (CF)[79], Levy and Zhang (LZ) [80] and Brataas et al. (B) [81]**.**

The CF model of DW scattering considers the reflection of incoming electrons by the effective potential created by the rotating magnetization (and hence internal exchange field) within the wall [79]. The reflection probability was found to depend on the ratio of the DW width δ to the Fermi wavelength λ, and is exponentially small for large ratios ($\sim e^{-\delta/\lambda}$). Thus, for DWs in the 10 nanometer range and metals with λ_f = 0.1 nm, the carrier reflection, and hence the DW resistivity, is entirely negligible.

The second model of DW scattering considers spin-dependent potentials and scattering rates, namely potentials and electron relaxation times that are different for spin up and spin down (majority and minority) electrons in the ferromagnet. This is critical to our present understanding of GMR. It also significantly amplifies the effect of DWs on

conductivity from that expected from electron reflection by a DW. The basic idea is as follows. In a uniformly magnetized ferromagnetic metal a large fraction of the total current is carried by one spin channel, either the majority or minority spins. Due to a small, non-adiabatic traversing of the electron spin in the wall, there is mixing of the spin channels within the DW [80]. This mixing partially eliminates the "short circuit" provided by the lower resistivity spin channel and increases the resistivity of the DW region. In a semi-classical Boltzmann calculation, Levy and Zhang found that the MR for current parallel to the DW (CIW-current in wall) is given by:

$$R_{CIW} = \frac{\rho_{CIW} - \rho_O}{\rho_O} = \frac{\xi^2}{5} \frac{(\rho_O{}^{\uparrow} - \rho_O{}^{\downarrow})}{\rho_O{}^{\uparrow} \rho_O{}^{\downarrow}} \qquad (3\text{-}4)$$

where the $\xi = \hbar \upsilon_f / (J\delta)$ is a measure of the non-adiabaticity (=0 is an adiabatic crossing), J is the internal exchange energy, υ_f is the Fermi velocity, δ is the DW width, and $\rho_O{}^{\uparrow(\downarrow)}$ is the resitivity of the spin up (down) channel. Physically, ξ is the ratio of the precession time of an electron in the exchange field to the time the electron takes to ballistically traverse the DW. In terms of length scales, this is the ratio of a "spin precession length" to the DW width. The "spin precession length" is the scale over which an electron at the Fermi energy completes a precession in the exchange field. Semi-classically, ξ is the angle a conduction electron spin makes with the local exchange field. Clearly, as the wall region is narrowed, the DW-MR is predicted to increase. It is also important to note that this is a perturbative result in ξ and thus the formula is not valid in the limit of very narrow DW, such as an atomic scale DW. In this case, the electron reflection would indeed be significant and MR effects greatly amplified. Levy and Zhang

further found that DWs cause larger MR when aligned perpendicular to the current flow. (CPW – current perpendicular to the wall)

$$R_{CPW} = \frac{\rho_{CPW} - \rho_O}{\rho_O} = \frac{\xi^2}{5} \frac{(\rho_O{}^{\uparrow} - \rho_O{}^{\downarrow})}{\rho_O{}^{\uparrow}\rho_O{}^{\downarrow}} \left(3 + \frac{10\sqrt{\rho_O{}^{\uparrow}\rho_O{}^{\downarrow}}}{\rho_O{}^{\uparrow} + \rho_O{}^{\downarrow}} \right) \quad (3\text{-}5)$$

Since the intrinsic reflection is assumed to be small (in contrast to CPP-GMR structures), spin accumulation effects can be neglected.

The third model, proposed by Brataas, Tatara, and Bauer, considers both ballistic and diffusive transport through a DW [81]. For typical parameters for Co, k_f =10 nm^{-1}, J =0 5 eV, $\rho_O^{\uparrow} / \rho_O^{\downarrow}$ = 5, and δ =15 nm, one calculates a CPW-MR of 2%. Note that this is the MR of the DW material itself, and domains in a sample 'dilute' this MR contribution by the ratio of DW width to the domain size.

There are also models that predict an intrinsic negative DW contribution to sample resistivity. Tatara and Fukuyama considered the effect of DWs on weak localization [82]. Weak localization is pronounced in low dimension disordered systems and arises due to quantum interference, which enhances electron backscattering and resistivity. Tatara and Fukuyama found that DWs destroy the electron coherence necessary for weak localization at low temperatures. As a consequence, in their model erasing DWs with a magnetic field restores weak localization and leads to an increase in the resistivity. Another second model by Gorkom, Brataas, and Bauer found that DWs can be regions of enhanced conductivity, when the electronic structure of the DW is taken into account semi-classically [83]. The essential idea is that the effective exchange field within a DW is weakened due to the non-colinear spin alignment (J(θ)= Jcosθ), where θ is the angle between neighboring spins). As a result, within a two band Stoner

model of the ferromagnet, there will be a redistribution of charge among the majority and minority spin bands (i.e., a change in the sample magnetization within the DW). Depending on the relative relaxation times of the bands, this can produce a positive or negative DW contribution to the resistivity. They found that the magnitude of this effect could be the same order as those treated by Levy and Zhang. And finally, Kent and Ruediger have proposed a mechanism by which the interplay between the surface scattering and the electron orbital motion within domains may reduce the resistivity [84]. They considered a geometry in which the magnetization is in the film plane, as illustrated in Figure 66(a). When diffuse electron scattering at the film top and bottom surface is important, the internal field acting on electron trajectories near walls will deflect charge from the film interfaces, reducing the amount of this scattering and decreasing the film resistivity.

3.5.2.2 Domain resistance

To further complicate matters, the contribution of DW's to MR can be 'masked' by extrinsic MR associated with ferromagnetic domain configurations. There are three such effects we discuss below: ferromagnetic resistivity anisotropy, a Hall effect mechanism, and diamagnetic effects.

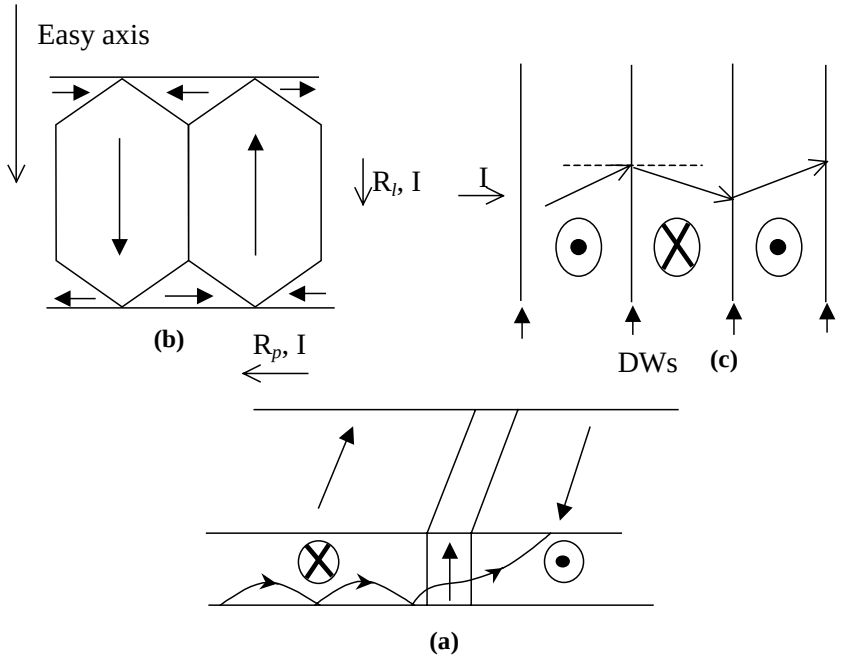

Figure 66 Stripe domain resistivity due to (a) the orbital motion of charge near and in DWs. (b) ferromagnetic resistivity anisotropy, and (c) a macroscopic Hall effect mechanism (view in the z =0 plane).

Ferromagnetic resistivity anisotropy. It is well known that the resistivity of a ferromagnetic material depends on the angle between the sample magnetization and the current [85]. Additionally, in a crystalline material the resistivity depends on the angle between the sample magnetization and the crystal axis. At low temperature (well below Tc) there are two factors that contribute to this anisotropy; (1) anisotropic MR (AMR), which is due to spin–orbit coupling and (2) the Lorentz MR which depends on the angle between the current and the internal field, B. These contributions will be discussed in more detail in the following sections. In a multi-domain sample, in which the magnetization is along more than one axis (Figure 66),

saturating the magnetization with an applied field will produce changes in the angle of the current and magnetization in some parts of the sample, and hence a MR due to ferromagnetic resistivity anisotropy. For a uniaxial material in the limit of small Q ($Q = K / 2\pi M_S^2$), domains at the border of the sample are parallel to the surface and perpendicular to the uniaxial axis, as illustrated schematically in Figure 66(b). Saturating this type of sample will produce an MR which reflects the difference in resistivity between perpendicular and longitudinally oriented domains. We can estimate this MR by using an appropriate medium model [77].

Hall effect Berger showed that there is another extrinsic mechanism by which a multidomain sample may have a higher resistivity than a saturated sample. The mechanism is based on the Hall effect [86]. The Hall effect leads to an angle between the current and the electric field, and in a ferromagnetic material the Hall angle can be large even in zero applied field due to the anomalous Hall effect, which is associated with spin–orbit effects. For a perpendicularly magnetized stripe domain material in the CPW geometry, when the domain subdivision is smaller than the sample width the Hall effect leads to current deflection near the DWs. In this geometry, the electric field will be normal to the DWs, except in a narrow region (within about a domain width) of the sample boundaries. As the Hall angle changes sign in alternating magnetization domains, the current will zig-zag through the sample, as illustrated in Figure 66(c). Berger found that this zig-zaging current leads to a resistivity increase of order $(\rho_{xy} / \rho_{xx})^2$, the Hall angle squared [87]. Also note that there is no such effect in CIW geometry, since in this case there is no current deflection. This means that there is a difference between CPW and CIW resistivities that goes as

$(\rho_{xy}/\rho_{xx})^2$. In the CPW geometry, this also produces 'domain drag', a force that an electric current exerts on a DW. This force is due to the magnetic field generated by the zigzagging current acting back on the domain structure. This effect has been discussed in previous chapter, where domain wall motion mechanisms were investigated.

Diamagnetic effects. The orbital motion of charge near a DW has also been considered from a microscopic point of view, originally by Cabrera and Falicov [79]. They found enhanced resistivity due to the "convoluted zig-zag trajectories of charge near a wall". This was also studied by Mankov, who found that the trajectories of charge near a wall can also lead to a decrease in the resistivity [88]. In both cases, these effects are of order $(\omega_c\tau)^2$, which can be large in very pure single crystals at low temperature but is generally small in metallic thin films.

3.5.2.3 Discussion of NiFe microstructure results in our experiment

The observation of resistance difference between two domain configurations shows that the "initial state" has higher resistance and fewer domains and domain walls, and the "final state" has lower resistance with more domains and domain walls. We can exclude the contributions from AMR because the two states have similar total area of domains in same magnetization direction. The negative DW contribution to the MR has been confirmed in experiments by other research groups on Fe microstructure [77, 89]. As discussed before there are three models of DW resistivity that predict a reduction in resistivity. The first model, from Tatara and Fukuyama, is based on weak localization (WL) phenomena. They find that DWs contribute to the

decoherence of conduction electrons which destroys WL. Essential to this model is the absence of other decoherence mechanisms, such as inelastic scattering. Kent found the maximum temperature for WL phenomena is about 7 K [90]. On this basis, the suppression of WL due to DWs cannot explain our observations of enhanced conductivity at room temperature. The second model, from Gorkom, Brataas, and Bauer, states that the impurities produce different asymmetries in the spin dependent scattering rates. This cannot be excluded as an explanation for our results. The third model, from Kent, indicates that the reduction in resistivity may not be intrinsic to the DWs. An extrinsic mechanism by which the alternating magnetization within the domains would increase the conductivity, this is illustrated in Figure 66(a). The internal fields acting on charge near the DWs deflect charge away from the surface and reduce the amount of diffuse surface scattering. Changing the nature of interface scattering, making it either more diffuse or specular, can test this model. For instance, thin over and underlayers have been shown to affect surface scattering in GMR structures [91].

As a conclusion, from existing models although we could not derive a clear mechanism in our results, the contribution from the negative DW resistivity is probably the major factor. The rather complex nature of the domain wall resistivity also prevents us from forming a single physical picture to explain the phenomena. Instead we use a combination of both surface scattering near domain wall model and impurity enhanced spin scattering asymmetry mode. There is a large amount of work need to be done in order to fully understand domain wall resistivity in ferromagnetic microstructures.

3.5.3 A prototype 8-bit magnetic memory cell

The use of current pulses to reliably store binary data in a magnetic state, and the ability to distinguish a state from based on resistance are the critical elements for a new type of magnetic random access memory. Guided by previous studies [75, 76], we propose to build an 8-bit memory cell. Compared with traditional MRAM schemes, this structure does not require external magnetic field sources, pinning layers or GMR/TMR multi-layers, resulting in a much simpler configuration and easier fabrication.

Based on the 8μm x 16μm $Ni_{81}Fe_{19}$ islands, we fabricated a memory chip with 1x8 bits by integrating eight individual cells with different bias leads and the same ground lead. The control circuit is made of relays shown in Fig. 67, each of which is operated by the 5V output from a digital I/O board. Fig. 68 is the driving circuit of the relays. Pulse generation is accomplished by charging a 4pF capacitor and discharging through the element. Switch S1 is used to set the current pulse polarity. Each bit uses two relays for reading and writing functions. For example switch S2 either charges the capacitor or to creates a pulse through the element 1. Switch S3 opens or closes the connection to the resistance measurement instrument, which in this case is a Keithley Multimeter. The others have similar functions on various bits. Fig. 69 is a photo of the circuit board, and the block schematic of 8-bit memory system including the measurement and control instruments is shown in Fig. 70.

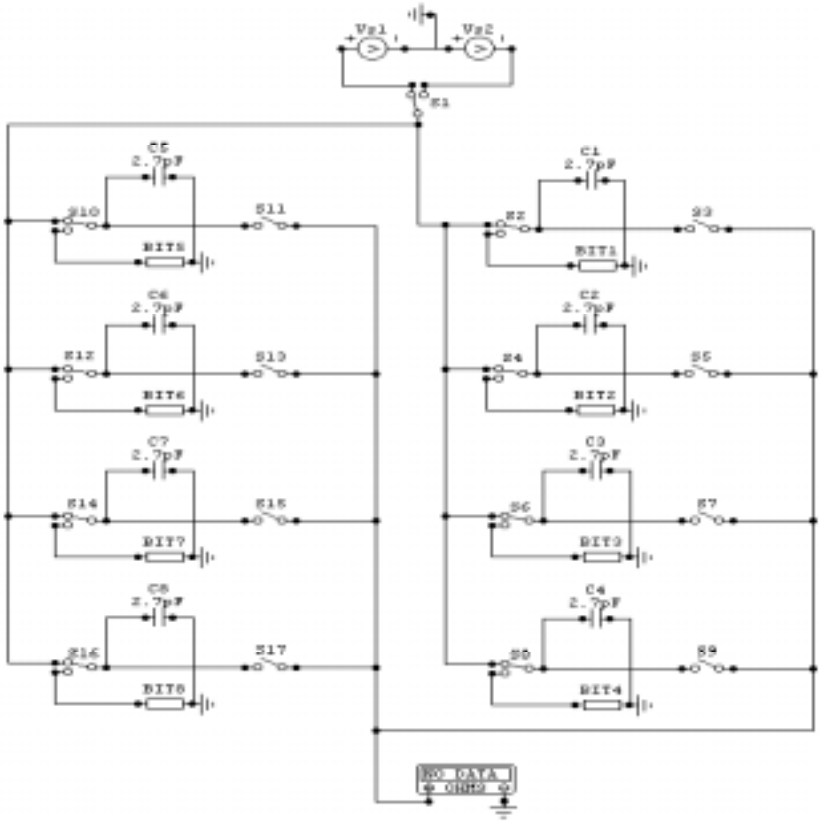

Figure 67 The circuit schematic of the 8-bit memory cell.

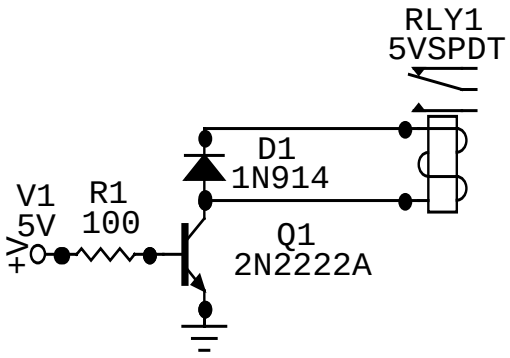

Figure 68 Switching function circuit, includes a relay, a transistor, a diode and a resistor.

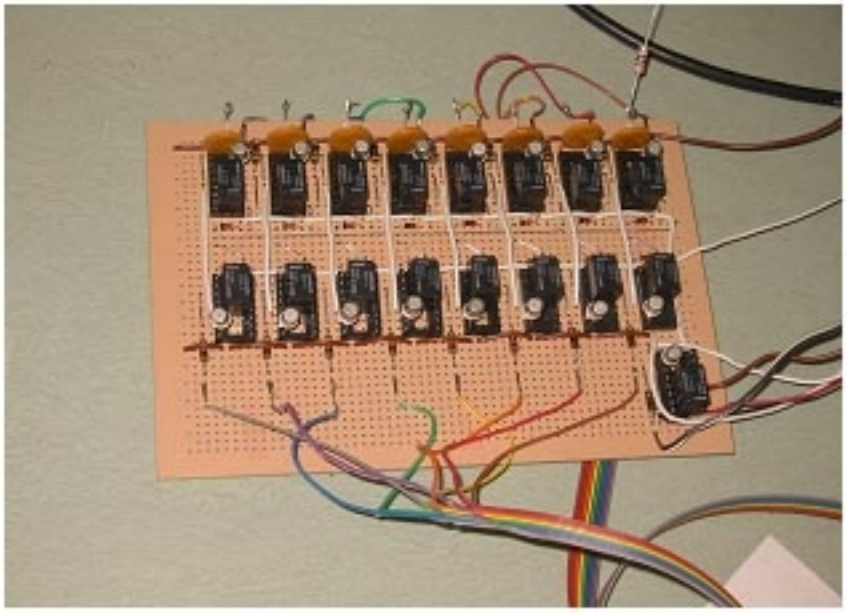

Figure 69 A photo of the circuit board.

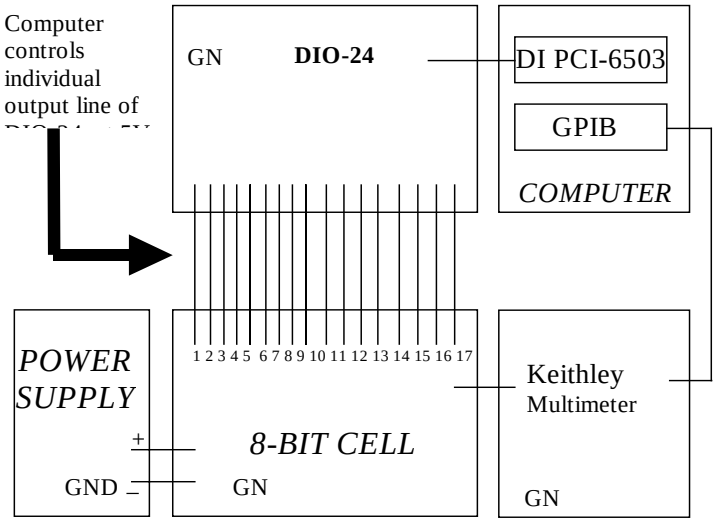

Figure 70 Schematic of the 8-bit cell and control, measurement set-up.

The resistances of each bit are shown in Fig. 71. By applying current with different polarities, we can control the domain configurations and resistance states of each bit. This represents a writing process that addresses each bit individually. By measuring the resistance of each bit, we can generate a binary sequence from which the written information was retrieved. This represents a reading process by defining higher resistance as logic “1” and lower resistance as logic “0”.

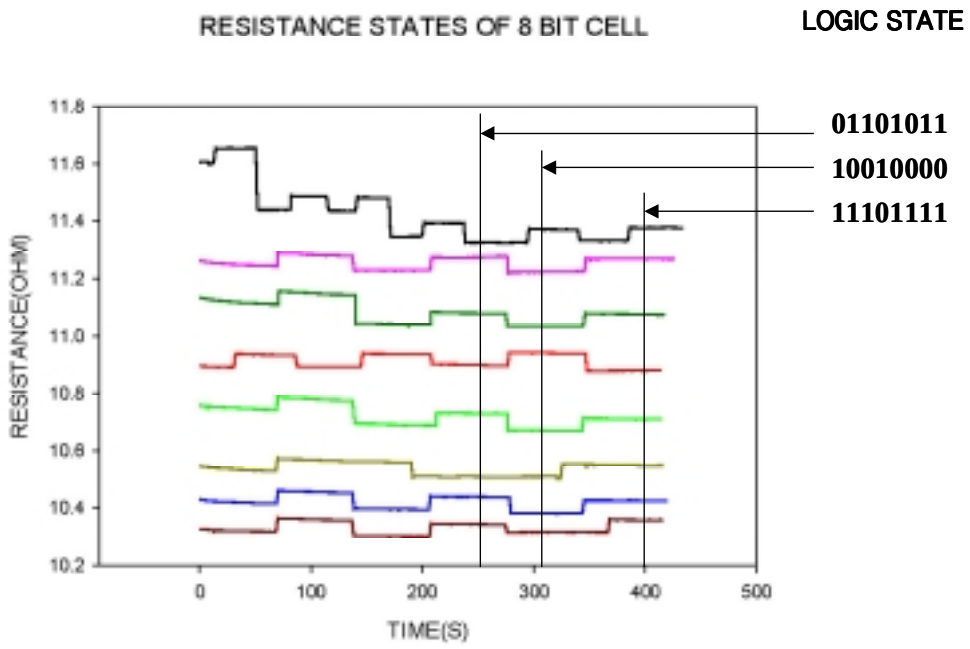

Figure 71 The resistance states of each bit in the 8-bit memory cell, arbitrarily set by current pulses. The high and low states were set by current pulse with different polarities. And the logic state of the cell is represented by a binary sequence that consists the resistance states of each bit by defining higher resistance as “1” and lower resistance as “0”.

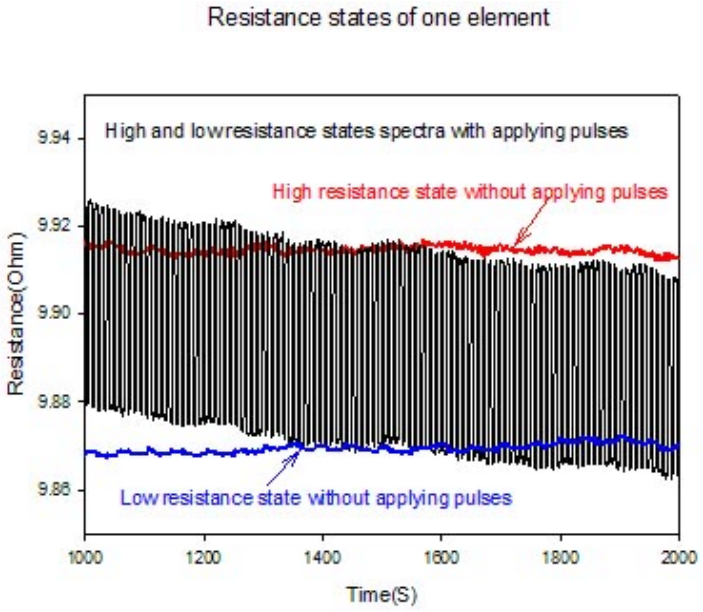

Figure 72 The resistance states of one element of the 8-bit memory cell. The black square spectra is showing the element has been written “1” and “0” alternatively 200 times. The blue line and red line are showing the stability of two logic states of this element

In addition to the evaluation of single islands in previous sections, we further investigated the performance of this memory cell and obtained the following performance parameters.

- Each element was cycled at a frequency of 0.2 Hz to establish reliability. The choice of 0.2 Hz is limited by the control circuitry, multimeter response and computer data acquisition. A typical data for one element is shown in Fig. 72. Even after 200 cycles, the element was shown to respond error free to the current input, and remains operational with very little signal to noise degradation. A monotonic overall decrease in the resistance was observed as a

function of the number of cycles, but appears to stabilize after a hundred pulses. This effect may be attributed may be attributed to annealing effects that improve the film quality and reduce the intrinsic resistivity. Note however, that the resistance variation (~0.1%) is maintained despite the resistance reduction.

- Each element was measured at high and low resistance states without switching to establish the stability of the states at room temperature. The data in Fig. 72, which shows the signal for a given 1000 seconds interval, establishes that thermal fluctuations account for roughly 0.001Ω variations corresponding to approximately 40dB SNR. No overall resistance reduction trend was observed.

Chapter 4: Summary and future work

Summary

In the past twenty years, research in solid-state magnetism has moved from bulk materials towards thin film structures. Fabrication techniques have not only significantly improved to make defect free films only a few atomic layers thick, but also to laterally pattern down to nanometer size features. The study of these nanomagnetic structure has uncovered exciting physical phenomena occurring with reduced dimensions, such as giant magnetoresistance, tunneling magnetoresistance, ballistic magnetoresistance, magnetic domain dynamics, domain wall motion and current induced magnetization switching. Some of these properties are already being used in applications in magnetic read/write heads, magnetic sensors, and MRAM's, while some are still awaiting novel usage pending clear fundamental understanding.

This thesis is the study of these physical properties in a number of magnetic structures. Attention was paid to both magnetoresistive thin film fabrication, characterizations and magnetic domain dynamics. This work resulted from a unique collaboration between NIST Magnetic Materials Group and the UMD Nanomagnetics group.

The most significant results contributions that we offer to the magnetics community are:

1. Understanding pinhole coupling. When two magnetic films are separated by a nonmagnetic film, pinholes in the nonmagnetic film can allow direct contact and thereby allow direct magnetic exchange coupling between the two magnetic films. This coupling, while extremely important in technology, is heretofore explored

because it is masked by exchange or magnetostatic interactions from surface roughness. We studied this by using a multilayer film with having one of the magnetic films pinned and the other free to switch at low field. Since the pinning strength increases sharply at low temperatures, but orange-peel coupling does not, low-temperature (77 K) measurements can distinguish if the coupling arises primarily from pinholes or from orange-peel roughness by comparing with the results from room temperature. Our measurements indicate that the observed coupling arises primarily from magnetic coupling through pinholes for Cu films less than 2.1 nm thick and for Al_2O_3 films less than 0.6 nm thick, and primarily from roughness-induced (orange-peel) magnetostatic coupling for larger thicknesses. This research has therefore given a useful tool monitoring the pinholes between fabrications and insights on critical film thicknessis.

2. Aluminum oxide as oxidation barrier. We have investigated the role of aluminum oxide films as barriers to thermal oxidation of Co, Ni, Fe, NiFe, Mn, Ta, Cu Al and Cr in air. The oxidation of the film was monitored by measuring the electrical resistances following a brief anneal in air. We found that Al films between 0.3 nm-1 nm of Al provides remarkable protection of the underlying metal film against thermal oxidation in air. Oxidation of protected films occur at temperatures a few hundred degrees higher than unprotected metal. These findings suggested that, in the production of magnetic tunnel junction, samples should be annealed in air after the oxidation of Al. The expected benefits of annealing in air would include the oxidation of any remaining of metallic Al, a more uniform Al_2O_3 thickness, and a

sharper metal/Al_2O_3 interface. Not surprising, annealing process have recently become standardized in industrial TMR fabrications [94].

3. Coating layer for Co protection. We have investigated the effectiveness of Al, Au, Cu, and Ta films with thickness up to 4 nm for protecting a Co surface from oxidation in air at room temperature. The distinct change in the Co $2p_{3/2}$ core-level lineshape observed by x-ray photoelectron spectroscopy upon the oxidation of Co makes it a simple matter to identify the fraction of the Co that is in the metallic state and oxidized state. We find that the best choices for protecting Co from oxidation are Al and Ta. We found that Au, which is one of the most popular choices, is not particularly effective for protecting Co.

4. BMR Measurements. We carried out extensive experiments to fabricate planar geometry nanocontacts by using electrodeposition techniques. We found the previous reported large BMR effects electrodeposited nanocontacts have been subject to various artifacts that can mimic BMR effect. For planar experiments with both in-plane and perpendicular electrodeposited nanocontacts, we only found small MR responses compare to BMR. This is due to the contact sizes in these experiments that are not small enough to produce atomic contact as achieved in break junction experiments. It requires significant technology advancement to fabricate stable atomic junctions with conductance at a few quanta.

5. Pulse-induced Magnetization Reversal. We have demonstrated that current pulses induce magnetic reconfiguration and discovered that bi-stable domain states can have distinguishable resistances. The mechanism for wall motion appears to be governed by s-d exchange interaction, and the symmetry is broken by the effects of

the global field. The resistance was found to decrease with the increase in the number of domain walls, indicating the reduction of resistivity within a domain wall.

6. MRAM 1-byte Prototype. A 1x8 memory cell was built based on the discoveries outlined in 5. It is a potentially valuable MRAM design because of the clear advantages over conventional design: no need of external field elements and single layer magnetic islands. This results in a much simpler configuration and a much easier fabrication process. Considering recent publications on current pulse induced domain wall motion in a spin valve [95] and current induced domain wall propagations in a nanometer size ferromagnetic element [96], we are optimistic that our experiments have provided an excellent addition in the subject of alternative magnetic switch methods for the application of magnetic recording and memory devices.

Future work

Several research directions could extend the scope of this dissertation. In the development of current-pulse controlled magnetic memory, there are three areas one could focus on, namely:

1. Scaling down the magnetic island size to reduce current requirement and increase areal density. When the sample size, specifically the cross-sectional area is reduced, the current and power consumption will be proportionately lower. Table 3 gives the calculations of the power consumption for different sizes elements.

2. Using multi-layer GMR/TMR structure to improve the magneto-resistance ratio between two logic states. In present configuration, the MR ratio is ~0.1% which

limits the sensitivity of the device. If we can fabricate a perpendicular GMR or TMR structure based on the current induced magnetization switching, we may easily achieve 10% MR ratio.

3. Fabricating a monolithic chip to integrate the pulse generator and read/write switch circuits together with the memory cell. The prototype memory cell we built in this work was based on an external control circuit board. The same addressing scheme can be implemented using transistors instead of relays, and could be integrated in a single MRAM chip with built-in switching relays and charging capacitors. The sub-micron size thin film patterns can be incorporated as a top layer of a silicon chip, through a thick oxide which hosts the magnetic islands.

Table 3 Power consumption

Lateral size	Thickness	Threshold current density	I	R	Power
4 μm × 8 μm	65 nm	6.42×10^{11} A/m^2	167 mA	4.62 Ω	129 mW
2 μm × 4 μm	65 nm	5.15×10^{11} A/m^2	67 mA	4.62 Ω	20.7 mW
1 μm × 2 μm	65 nm	8.31×10^{11} A/m^2	54 mA	4.62 Ω	13.5 mW

For the ultra-thin film pinhole detection and control, one can investigate the critical thickness for pinhole closure by monitoring resistance sudden decrease while thin films are growing. A large resistance drop at this case indicates the thin film surface covers the substrate completely and all pinhole are closed. This could be

correlated with the onset pinhole formation. For the TMR annealing effect study, it will be interesting to grow oxide barrier in an elevating temperature. A more uniform and stable barrier is always a potential improvement of the TMR device performance. We have noticed that in the XPS scans, for example in Fig. 25, the oxidized Co not only has shifted peak but also has wider line shape. It is therefore essential to investigate the lineshape profiles to establish of oxidization is occurring at the interface.

The work in this dissertation has established a solid ground for further studies in some of the most important aspects of magnetic thin film devices. With new developments in magnetic and process technology, I hope that the above proposed directions based on our present knowledge can serve as the starting points for new discoveries to be made.

Appendix I: Thin film fabrication and characterization methods

1. Deposition techniques [97]

Sputtering

Magnetron sputtering is achieved by bombarding a target with energetic ions, typically Argon. Atoms at the surface of the target are knocked loose and transported to the substrate, where deposition occurs. Electrically conductive materials such as Al, W, and Ti can use a dc power source, in which the target acts as the cathode in a diode system. Dielectrics such as SiO_2 or Al_2O_3 require an RF power source to supply energy to the argon atoms. Generally, better film properties are achieved by higher substrate temperature and lower argon pressure. The advantages of sputtering are: high deposition rate, the capability to deposit and maintain complex alloy composition, the capability to deposit high-temperature and refractory metals, in multi-chamber systems to clean the contact before deposition, and to maintain well-controlled, uniform deposition on large wafers. These make sputtering the preferred choice in today's physical vapor deposition.

MBE

Molecular Beam Epitaxy (MBE) is a sophisticated deposition technique performed in ultra high vacuum to grow compound semiconductors. In MBE, atoms of an element or compound are delivered to a substrate through an ultra-pure, ultra-high vacuum atmosphere. The UHV atmosphere provided by the MBE chamber

allows the atoms to arrive on the substrate without colliding with other atoms or molecules. This keeps the growth free of other contaminants. The heated substrate surface allows the arriving atoms to distribute themselves evenly across the surface to form an almost perfect crystal structure. In MBE the substrate is placed in an UHV chamber with direct line of sight to several elemental species, each of which is in an evaporation furnace commonly referred to as an effusion cell. Through use of shutters and precise control of the effusion cell temperatures almost any material composition and doping can be achieved. Our MBE apparatus is equipped with two e-beam evaporators and six Knudsen cells.

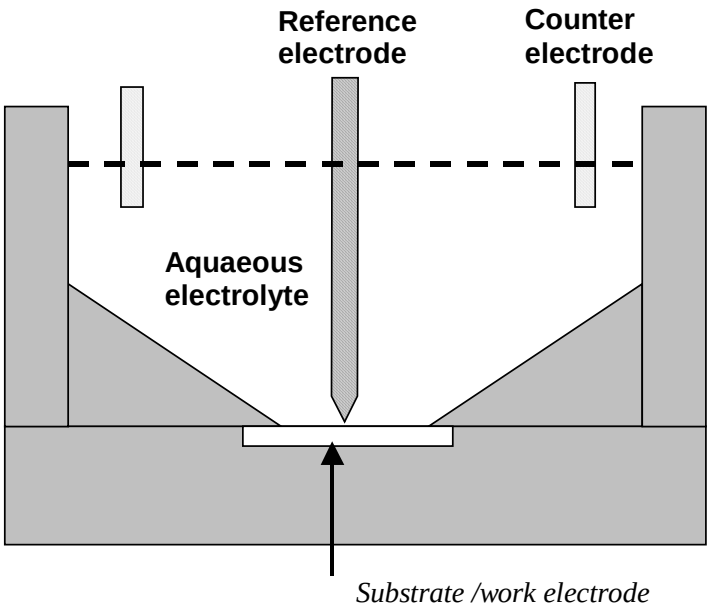

Figure 73 An illustration of an electro-deposition cell.

Electrodeposition

Electrodeposition, also called electroplating, has been used for a long time in various applications, such as protective coating and Permalloy thin film recording

heads. The deposition of metals takes place at ambient temperatures and pressures in an electrochemical cell containing the metal ions in an aquaeous solution, as shown in Figure 73. By applying a voltage between the substrate (work electrode/cathode), and the counter electrode (anode), the metal ions from metal are deposited on the substrate.

2 Pattern Transfer Techniques

Photolithography [98, 99]

In modern semiconductor integrated circuit fabrication, thin film of various materials are deposited on the silicon substrate, holes and windows are cut through these thin films wherever contact are desired. Masks contain the patterns of windows, which are transferred to the surface of the silicon wafer using several methods. One of these processes called photolithograpy, which makes use of a highly refined version of photoengraving process. The patterns are transferred from mask to a light-sensitive material called photoresist.

A liquid photoresist is applied on the metalized silicon substrate and then held on a vacuum chuck. It is spun at a rate of 1000 to 5000 rpm for 30 to 60 seconds to produce thin uniform layer, ranging from 2.5 um to 0.5 um in thickness. The actual thickness of the resist depends on its viscosity and its inversely proportional to the square root of the spin speed. Next, a photomask - a square glass plate with a patterned metal film on one side - is placed over the wafer. A manual mask aligner is used for this purpose, and the wafer is carefully moved into position below the mask. The photoresist is exposed through the mask with high-intensity ultraviolet light. Any

positive photoresist which has been exposed can be washed away by using a developer, leaving a pattern of the unexposed area. There are three printing technologies: contact, proximity and projection. Contact printing has been largely replaced by proximity and projection printing system in order to prevent damage to the mask when wafer come in contact with the mask. In general, the basic photolithographic process can be summarized below: clean sample wafers-deposit metal layer-coat with photoresist-soft bake-align mask-expose pattern-develop photoresist-hard bake-etch windows in metal layer-remove photoresist. Shown in Fig. 74.

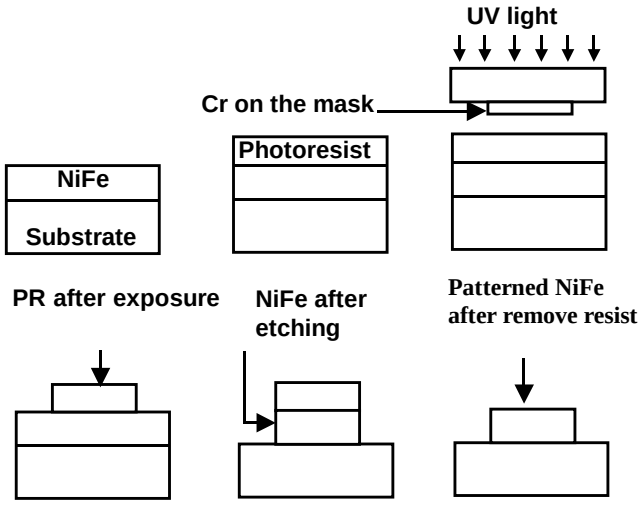

Figure 74 Procedures for basic photolithography patterning using etching technique.

Etching

There are basically two methods possible used in the etching process, dry etching and wet chemical etching. Dry etching uses small amounts of gases and is capable of producing either isotropic or anisotropic profiles, depending on the gas

chemistry used and the configuration of the etching system. A few examples of dry etching include reactive ion etching (RIE) and sputter etching. Wet etching relies heavily on chemicals and can either be an isotropic process or anisotropic process depending on the crystallography of the substrate and type of etching solution used. The wet etching of NiFe has been suggested by recipe HCl, 25°c, 500Å/3 min [100], and dry etching by using CH_4/H_2, SF_6/Ar, Cl_2/Ar [101].

Lift-off procedure [102]

Lift-off is the process to directly pattern the metal by using a solvent to dissolve the remaining photoresist underneath the metal. The process sequence is little different than the normal photolithography process. The procedure is summarized in Fig. 75.

For positive photoresist, after the wafer has been exposed, another step is performed to produce the desired overhanging profile required by liftoff. The wafer is placed in a chlorobenzene soak for several minutes. The chlorobenzene diffuses into the photoresist causing it to swell. A gel is formed to the depth of the diffusion, which has a different development rate than the rest of the resist. This will cause the developer to undercut the photoresist structures and produce the desire profile. Then the wafer is dried with nitrogen and developed using some developer. Next, metal is deposited onto the wafer. Once the photoresist is removed, the metal covering the photoresist is also removed (lifted off). Sometimes, ultrasonic bath and/or slight mechanical scrubbing with a clean room swab is needed to assist in the liftoff process. In general, mechanical scrubbing is not recommended because it can damage

the deposited film. In most cases, negative photoresist are used by controlling the exposure time to achieve the overcut profile of photoresist. For good lift-off processing, two limitations are: thickness of metal layer is less than 1/10 of the photoresist thickness, the substrate temperature in deposition is below 300°c where resist begins to degrade.

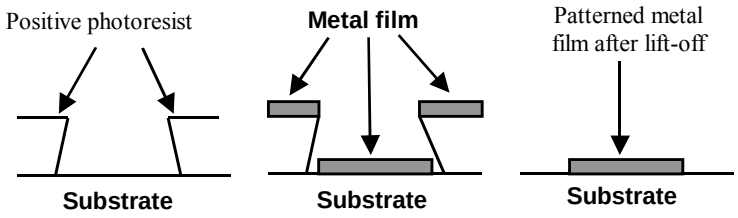

Figure 75 The procedures of lift-off. The desired undercut profile of photoresist is seen in the second picture.

3 Thin film analysis and characterization tools

XPS [103]

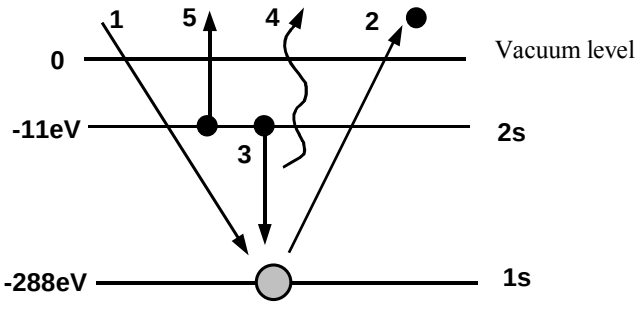

Figure 76 Illustration of XPS principles.

X-ray photoelectron spectroscopy (XPS) is a surface diagnostic tool to determine the composition of several layers of the surface. An energetic probe beam of electrons or photons eject an electron out of an inner shell of a near-surface atom into vacuum, as shown for an atom of carbon in Fig. 76. The escaping electron (2) is known as the secondary photoelectron. The inner shell vacancy is then filled by an electron dropped down from a higher shell of that atom (3). The potential energy difference between the two shells is thereby released either into a photon (4), or into the kinetic energy of an escaping outer shell electron, Auger electron (5). The chemical elements then can be identified by peaks in the energy spectrum of the escaping photons or electrons, since the positions of these peaks are determined by the energy levels of the electron shell of the probed atoms. The escape energy also tells something about chemical bonding state of the atom. For example, an atom stripped of valence electrons by bonding to an electronegative element such as O will have a higher binding energy to make the core peaks shift. In these techniques, if the probe is an electron beam, it is Auger-electron spectroscopy (AES), and if photon probes are used, the technique is referred as XPS. It is called ESCA (electron spectroscopy for chemical analysis) if electrons are used as probe and photons are detected. XPS is generally used for film analysis after deposition. XPS typically uses the Al (Kα) x-ray line at 1487 eV as a probe. The probe area is large ~ 100um and probe depth is ~ 1um, but these 100-1000 eV electrons can only escape from a few nm of the sample surface.

Magnetic Force Microscopy (MFM)[104]

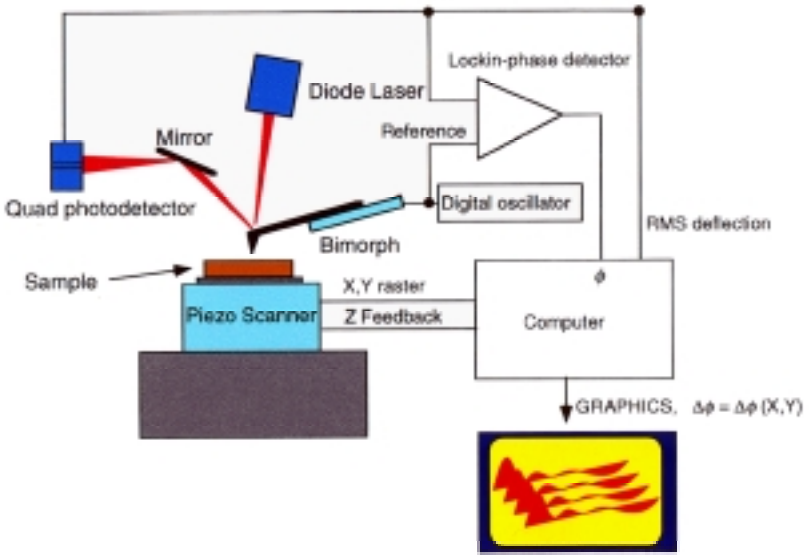

Figure 77 A schematic of MFM components and operation.

Magnetic force microscopy (MFM) is one of the most widely used methods of magnetic imaging because its convenience and high spatial resolution. The MFM used in our UM/LPS lab is a Multi-Mode MFM with a Nanoscope III controller, both from Digital Instruments. External magnetic field and current pulses can be applied on the sample during the MFM operation by our customized external design. Our probes consist of a magnetic material (cobalt-chromium) deposited on the very end of the Si tips to provide the magnetic interaction. During operation, the cantilever is forced to oscillate at its resonant frequency by a set of piezoelectric bimorphs. The resonant frequency is determined by a tuning process controlled by the Digital Instruments software. Other piezoelectrics move the sample beneath the tip to allow the tip to raster over a rectangular area of the sample. As the tip moves over the sample surface, the oscillations change depending on the magnetic interactions

between the tip and the sample. The change in oscillations is detected by a photodetector located in the scanning head of the MFM. A light beam is bounced off the back of cantilever and is captured by a photodetector. This deflection is then digitally processed to produce the images. See Fig. 77.

STM

The Scan Tunneling Microscopy is able to probe surface structure down to an atomic scale. The STM tip is a sharp conducting needle, controlled by a piezo-electric tube. When the tip is brought to 0.1 – 1 nm from the sample's conducting surface, a tunneling current can be observed by applied a bias voltage. By scanning along the surface and monitoring the tunneling current as function of position (or by adjusting the distance from surface to keep constant tunneling current), a topographic map of the surface structure cab be obtained with atomic resolution. Strictly speaking, STM probes local density of states that may or may not correspond to the location of ionic cores.

4 The thin film engineering facility at NIST

One of the most elaborately instrumented magnetic thin film deposition facilities, allows samples to be investigated at every step of fabrication: Modern surface / interface / Magnetic diagnostics / Elemental composition / thickness / atomic structure / roughness Improve devices related materials structure and properties. See Fig. 78.

1. Different deposition methods: MBE / Sputtering / E-beam evaporation

2. Numerous in situ surface characterization techniques: STM / XPS / AES / LEED / Mass spectrometry / Real-time 4-wire resistivity
3. In situ magnetic measurements: MR (Super-conducting magnet / electromagnet Magneto-optical Kerr effect

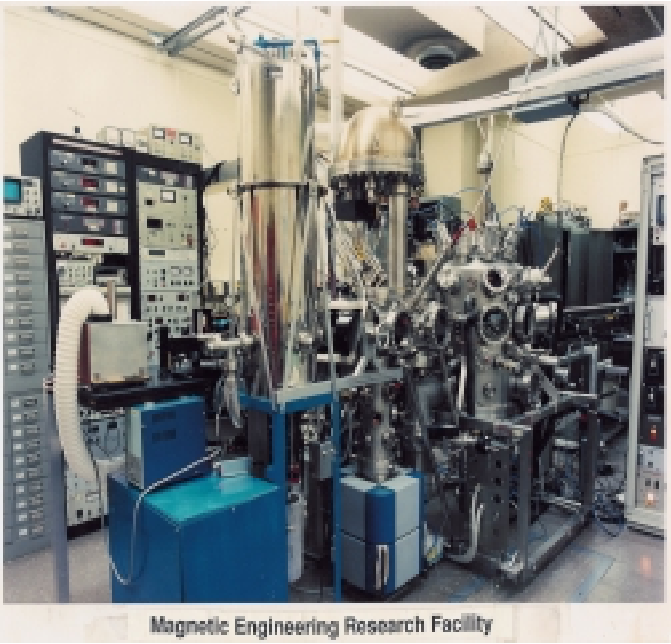

Figure 78 Facility of NIST magnetic thin film fabrication and characterizations.

Appendix II: A Visual-Basic program was written to control the write/read process and follows the flowchart below:

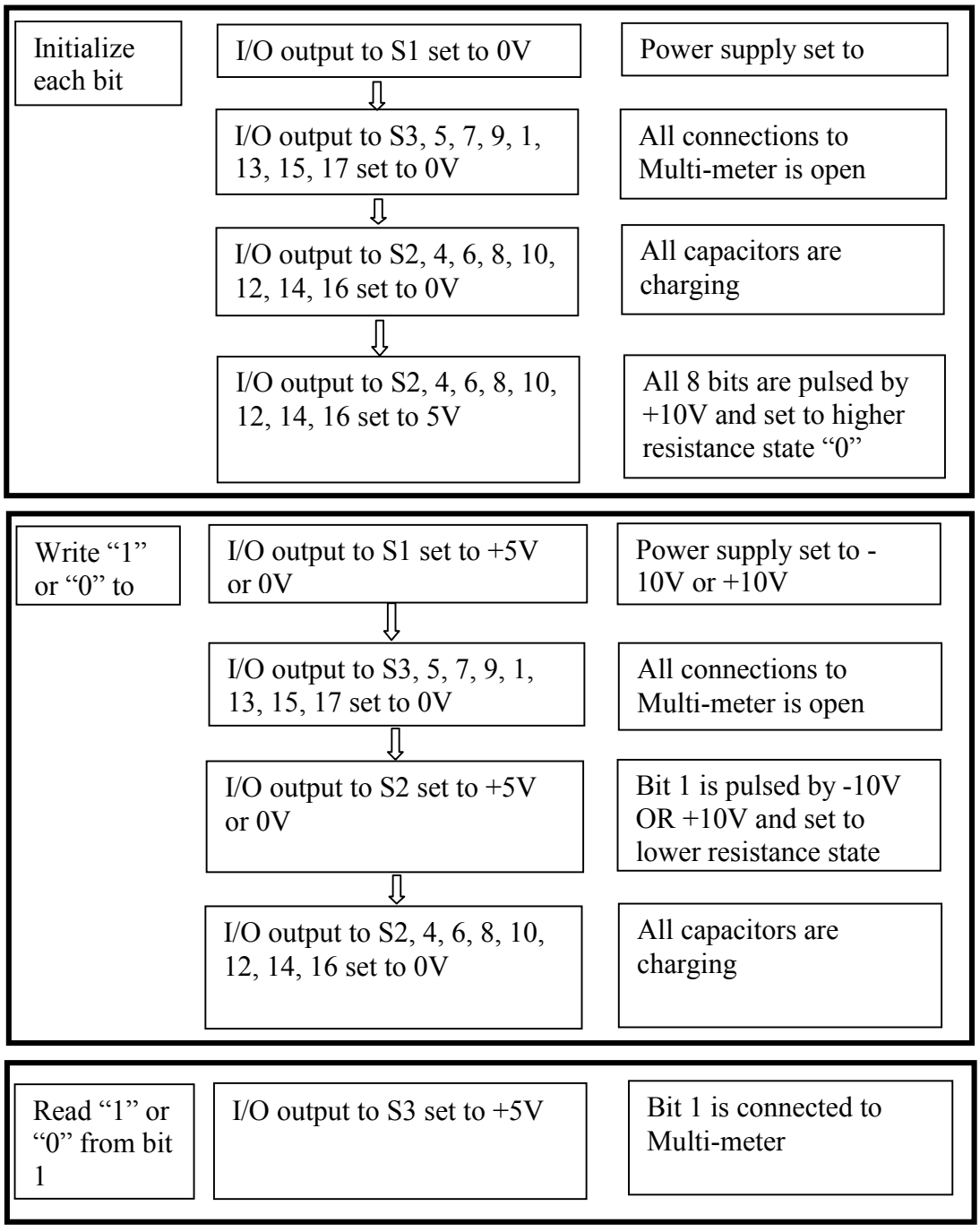

References

1. Http://www.research.ibm.com
2. G. A. Prinz and K. B. Hathaway, Physics Today, April 1995, pp. 24-63.
3. J. M. Daughton, J. Appl. Phys. 81, 8 (1997).
4. M. N. Barbich, J. M. Broto, A. Fert, F. Nguyen Van Dau, F. Petroff, P.Etienne, G. Creuzet, A. Friederich, and J. Chazelas, Phys. Rev. Lett. 61, 2472 (1988).
5. J. S. Moodera, L. S. Kinder, T. M. Wong, and R. Meservey, Phys. Rev. Lett. 74, 3273 (1995).
6. N. García, M. Muñoz, and Y.-W. Zhao, Phys. Rev. Lett. 82, 2923 (1999).
7. B. Heinrich, J. Brand (Eds), Ultrathin Magnetic Structures I & II, 1994, Springer-Verlag.
8. J. Julliere, Phys. Rev. Lett., 54A, 225 (1975).
9. J. M. De Teresa, A. Barthélémy, A. Fert, J. P. Contour, R. Lyonnet, F. Montaigne, P. Seneor, and A. Vaurès Phys. Rev. Lett. 82, 4451(1999).
10. K. Shimazawa, O. Redon, N. Kasahara, J. Sun, H. Korita, and M. Matsuzaki, Digest of Intermag 2000 FA-01 (2000).
11. E. Y. Chen, R. Whig, J. M. Slaughter, D. Cronk, J. Goggin, G. Steiner, and S. Tehrani, J. Appl. Phys. 87, 6061(2000). J. S. Moodera and L. R. Kinider, J. Appl. Phys., 73, 4724(1996), H. Boeve, Appl. Phys. Lett. 76, 1048(2000). J. M. Slaughter, E. Y. Chen, R. Whig, B. N. Engel, J. Janesky and S. Tehrani, JOM-e 6, 52(2000).

12. G. Tatara, Y.-W. Zhao, M. Muñoz, and N. García, Phys. Rev. Lett. 83, 2030 (1999).
13. S. H. Chung, M. Munoz, N. Garcia, W. F. Egelhoff, and R. D. Gomez, Phys. Rev. Lett., 89, 287203 (2002).
14. W. P. Meiklejohn and C. P. Bean, Phys. Rev. 102, 1413 (1956).
15. B. Dieny, Phys. Rev. B43, 1297 (1991).
16. W. P. Meiklejohn, J. Appl. Phys., 33 1328 (1962).
17. L. Neel, Ann. Phys. Paris 2, 61 (1967).
18. P. Malozemoff, Phys. Rev. B35, 2679 (1987); Phys. Rev. B37, 7673 (1988).
19. N. C. Koon, Phys. Rev. Lett. 78, 4865 (1997).
20. T. C. Schulthess, W.H Bultler, Phys. Rev. Lett. 81, 4516 (1998).
21. M. Kiwi, Europhys. Lett. 48, 573 (1999); M. D. Stiles, R. D. McMichael, Phys. Rev. B 59, 3722 (1999).
22. S. Parkin, Annu. Rev. Mater. Sci., 25, 357 (1995).
23. J. Kools, IEEE Trans. On Mag. 32, 3165 (1996)
24. J. F. Bobo, M. Piecuch, and E. Snoeck, J. Magn. Magn. Mater. 126, 440 (1993); S. K. J. Lenczowski, C. Schonenberger, M. A. M. Gijs, and W. J. M. DeJonge, J. Magn. Magn. Mater. 148, 455 (1995); M. T. Kief, J. Bresowa, and Q. Leng, J. Appl. Phys. 79, 4766 (1996); H. Kikuchi, J. F. Bobo, and R. L. White, IEEE Trans. Mag. 33, 3583 (1997); F. Stobiecki, T. Lucinski, R. Gontarz, and M. Urbaniak, Mater. Sci. For. 287, 513 (1998); J. F. Bobo, H. Kikuchi, O. Redon, E. Snoeck, M. Piecuch, and R. L. White, Phys. Rev. B 60, 4131 (1999); B. J. Jönsson-Åkerman, R. Escudero, C. Leighton, S. Kim, I. K.

Schuller, and D. A. Rabson, Appl. Phys. Lett. 77, 1870 (2000); D. Allen, R. Schad, G. Zangari, I. Zana, D. Yang, M. C. Tondra, and D. Wang, Appl. Phys. Lett. 76, 607 (2000); M. F. Gillies and A. E. T. Kuiper, J. Appl. Phys. 88, 5894 (2000); H. Boeve, J. De Boeck, and G. Borghs, J. Appl. Phys. 89, 482 (2001)

25. T. Luciński, S. Czerkas, H. Brückl, and G. Reiss, J. Mag. Mat. Mat. 222, 327 (2000).
26. W. F. Egelhoff, Jr., T. Ha, R.D.K. Misra, Y. Kadmon, J. Nir, C. J. Powell, M. D. Stiles, R. D. McMichael, C.-L. Lin, J. M. Sivertsen, J. H. Judy, K. Takano, A. E. Berkowitz, T. C. Anthony, and J. A. Brug, J. Appl. Phys., 78, 273 (1995); W. F. Egelhoff, Jr., P. J. Chen, C. J. Powell, M. D. Stiles, R. D. McMichael, C.-L. Lin, J. M. Sivertsen, J. H. Judy, K. Takano and A. E. Berkowitz, J. Appl. Phys. 80, 5183 (1996); W. F. Egelhoff, Jr., P. J. Chen, C. J. Powell, M. D. Stiles, R. D. McMichael, J. H. Judy, K. Takano, and A. E. Berkowitz, J. Appl. Phys., 82, 6142 (1997)
27. J. C. S. Kools, W. Kula, D. Mauri, T. Lin, J. Appl. Phys. 85, 4466 (1999); B. D. Schrag, A. Anguelouch, S. Ingvarsson, G. Xiao, Y. Lu, P. L. Trouilloud, A. Gupta, R. A. Wagner, W. J. Gallagher, P. M. Rice, and S. S. P. Parkin, Appl. Phys. Lett. 77, 2373 (2000).
28. J. S. Moodera, T. H. Kim, C. Tanaka, and C. H. de Groot, Phil. Mag. B 80, 195 (2000).
29. W. F. Egelhoff, Jr., P. J. Chen, C. J. Powell, M. D. Stiles, R. D. McMichael, J. H. Judy, K. Takano, and A. E. Berkowitz, J. Appl. Phys., 82, 6142 (1997)

30. T. Mitsuzuka, K. Matsuda, A. Kamijo, and H. Tsuge, J. Appl. Phys. 85, 5807 (1999); L. Thomas, A. J. Kellock, and S. S. P. Parkin, J. Appl. Phys. 87, 5061 (2000); R. Jansen and J. S. Moodera, Phys. Rev. B 61, 9047 (2000); and J. S. Moodera, J. Nassar, and G. Mathon, Ann. Rev. Mat. Sci. 29, 381 (1999).
31. H. Boeve, J. De Boeck and G. Borghs, J. of Appl. Phys. 89, 482 (2001); H. Tsuge, T. Mitsuzuka, A. Kamijo and K. Matsuda, Mater. Res. Soc. Symp. Proc. 517, 87 (1998); T. Mitsuzuka, K. Matsuda, A. Kamijo, and H. Tsuge, J. Appl. Phys. 85, 5807 (1999); K. Matsuda, A. Kamijo, T. Mitsuzuka and H. Tsuge, J. Appl. Phys. 85, 5261 (1999)
32. S. V. Kumari, M. Natarajan, V. K. Vaidyan and P. Koshy, J. of Mater. Sci. Lett. 11, 761 (1992); R. V. Anavekar, N. Devaraj and J. Ramakrishna, Phys. & Chem. of Glasses 32, 103 (1991); Y. Sun, O. Ehrmann, J. Wolf and H. Reichi, Rev. Sci. Instrum. 63, 3752 (1992); S. X. Wang,, K. Yamada, and W. E. Bailey, IEEE Trans. Mag. 36, 2841 (2000); T. Lucinski, S. Czerkas, H. Bruckl, and G. Reiss, J. Mag. Magn. Mat. 222,327 (2000). N. Birks, G. H. Meier and F. S. Pettit, J. of Metals 39, 28 (1987); C. J. Rosa, Corrosion Science 22, 1081 (1982); D. E. Larsen Jr, Scripta Metallurgica, 1379 (1987).
33. J.G. Simmons, J. Appl. Phys. 34, 1793 (1963).
34. S. V. Kumari, M. Natarajan, V. K. Vaidyan and P. Koshy, J. of Mater. Sci. Lett. 11, 761 (1992); R. V. Anavekar, N. Devaraj and J. Ramakrishna, Phys. & Chem. of Glasses 32, 103 (1991); Y. Sun, O. Ehrmann, J. Wolf and H. Reichi, Rev. Sci. Instrum. 63, 3752 (1992); S. X. Wang,, K. Yamada, and W.

E. Bailey, IEEE Trans. Mag. 36, 2841 (2000); T. Lucinski, S. Czerkas, H. Bruckl, and G. Reiss, J. Mag. Magn. Mat. 222,327 (2000).

35. N. Birks, G. H. Meier and F. S. Pettit, J. of Metals 39, 28 (1987); C. J. Rosa, Corrosion Science 22, 1081 (1982); D. E. Larsen Jr, Scripta Metallurgica, 1379 (1987)
36. W. F. Egelhoff Jr., P. J. Chen, R. D. McMichael, C. J. Powell, R. D., Deslattes, F. G. Serpa, R. D. Gomez, J. Appl. Phys. 89, 5209 (2001)
37. V. Shutthanandan, A. A. Saleh, R. J. Smith, J. Vac. Sci. Technol. A 11, 1780 (1993)
38. A. V. Mijiritskii and D. O. Boerma, J. Magn. Magn. Mater. 232, 9 (2001).
39. T. Lin and D. Mauri, Appl. Phys. Lett. 78, 2181 (2001).
40. A. Stierle, T. Muhge and H. Zabel, J. Mater. Res. 9, 884 (1994).
41. A. L. Cabrera, J. F. Kirner and J. N. Armor, J. Mater. Res. 6, 71 (1991).
42. S. X. Wang, K. Yamada, W. E. Bailey, IEEE Trans. Mag. 36, 2841 (2000).
43. W. F. Egelhoff Jr., P. J. Chen, R. D. McMichael, C. J. Powell, and L. Gan, unpublished results.
44. N. García, H. Rohrer, I.G. Saveliev, and Y.-W. Zhao, Phys. Rev. Lett. 85, 3053 (2000).
45. N. Garcia, M. Munoz, G. G. Quan, H. Rohrer, I. G. Savelief, and Y.-W. Zhou, Appl. Phys. Lett. 79, 4550 (2001)
46. N. Garcia, M. Munoz, and Y.-W. Zhao, Appl. Phys. Lett. 76, 2586 (2002)
47. N. Garcia, G. G. Qian, and I. G. Savelief, Appl. Phys. Lett. 80, 1785 (2002).

48. N. Garcia, H. Wang, H. Cheng, and N. D. Nikolic, IEEE Trans. Mag. 39, 2776 (2003).

49. Harsh Deep Chopra and Susan Z. Hua, Phys. Rev. B 66, art. no. 020403 (2002). Susan Z. Hua and Harsh Deep Chopra, Phys. Rev. B 67, art. no. 060401 (2003)

50. J. J. Versluijs, M. A. Bari, and J. M. D. Coey, Phys. Rev. Lett. 87, art. no. 0266011 (2001).

51. J. M. D. Coey, J. J. Versluijs, M. Venkatesan, J. Phys. D 35, 2457 (2002).

52. M. Viret, S. Berger, M. Gabureac, F. Ott, D. Olligs, I. Petej, J. F. Gregg, C. Fermon, G. Francinet, and G. Le Goff, Phys. Rev. B 66 art. no. 220401 (2002).

53. J. Baszynski, T. Tolinski, W. Kowalski, A. Kowalczyk, Czech. J. Phys. 52, A13, Suppl. A (2002).

54. J.-E. Wegrowe, T. Wade, X. Hoffer, L. Gravier, J.-M. Bonard, and J.-Ph. Ansermet, Phys. Rev. B 67, art. no. 104418 (2003).

55. H. Pandana, L. Gan, M. Dreyer, C. Krafft and R. D. Gomez, IEEE Trans. Mag., 2004, in press.

56. J. J. Mallett , E. B. Svedberg, H. Ettedgui, T. P. Moffat and W. F. Egelhoff, Jr., Appl. Phys. Lett., in press.

57. E. B. Svedberg, J. J. Mallett , H. Ettedgui, L. Gan, P. J. Chen, A. J. Shapiro, T. P. Moffat, and W. F. Egelhoff, Jr., Appl. Phys. Lett., in press.

58. R. Schad, D. Allen, G. Zangari, I. Zana, D. Yang, M. C. Tondra, and D. Wang, Appl. Phys. Lett. 76, 607 (2000)

59. C. L. Platt, M. R. McCartney, F. T. Parker, and A. E. Berkowitz, Phys. Rev. B 61, 9633 (2000).

60. L. H. Yu and D. Natelson, Appl. Phys. Lett. 82, 2332-2334 (2003).

61. M. Daughton, Thin Solid Films 216, 162(1992).

62. E. Hirota, H. Sakakma, and K. Inomata, Giant Magneto-Resistance Devices, Springer, 2001.

63. C. Y. You and S. D. Bader, J. Magn. Magn. Mater. 185, 488 (1999).

64. J. Slonczewski, J. Magn. Magn. Mater. 159, 1 (1996).

65. L. Berger, Phys. Rev. B 54, 9353 (1996).

66. E. B. Myers, D. C. Ralph, J. A. Katine, R. N. Louie, and R. A. Buhrman, Science 285, 867 (1999).

67. L. Berger, J. Appl. Phys. 55, 1954 (1984).

68. E. Salhi and L. Berger, J. Appl. Phys. 76, 4787 (1994).

69. W. J. Carr, J. Appl. Phys. 45, pp. 394, 1974. S.H. Charap, J. Appl. Phys. 45, 397 (1974).

70. S. Foss, E. D. Dahlberg, R. Proksch, and B. M. Moskowitz, J. Appl. Phys 81, 5032 (1997).

71. U. Hartmann, Physical Review B 40, 7471 (1989).

72. C.-Y. Hung, and L. Berger, J. Appl. Phys. 63, 4276 (1988).

73. J. Smit, Physica, 21, 877 (1955); W. Jellinghaus and M.P. DeAndres, Ann. Physik 5, 187 (1960).

74. P. P. Freitas and L. Berger, J. Appl. Phys. 57, 1266 (1985).

75. H. Koo, C. Krafft, and R. D. Gomez, Appl. Phys. Lett. 81, 862 (2002).

76. L. Gan, S.H. Chung, K. Aschenbach, M.Dreyer and R.D. Gomez, IEEE Trans. Magn. 36, 3047-3049 (2000)

77. A. D. Kent, J. Yu, U. Ruediger, and S. S. P. Parkin, J. Phys.: Condens. Matter 13, 461 (2001).

78. G. R. Taylor, A. Isin, and R. V. Coleman, Phys. Rev. vol. 165, 621 (1968).

79. G. G. Cabrera and L. M. Falicov, Phys. Status Solidi (b) 61, 59 (1974). G. G. Cabrera and L. M. Falicov, Phys. Status Solidi (b) 62, 217 (1974).

80. P. M. Levy and S. Zhang, Phys. Rev. Lett. 79, 5110 (1997).

81. A. Brataas, G. Tatara and G. E. W. Bauer, Phys. Rev. B 60, 3406 (1999).

82. G. Tatara and H. Fukuyama, Phys. Rev. Lett. Vol. 78, 3773 (1997).

83. van R. P. Gorkom, A. Brataas, and G. E. W. Bauer, Phys. Rev. Lett.vol. 83, 4401 (1999).

84. A. D. Kent, U. Ruediger, J. Yu, S. Zhang, P. M. Levy and S. S. P. Parkin, IEEE Trans. Magn. 34, 900 (1996).

85. L. A. Campell and A. Fert, Ferromagnetic Materials, E P WOHLFARTH, Vol. 2, 1992.

86. L. Berger, J. Appl. Phys. 49, 2156 (1978).

87. L. Berger, Phys. Rev. B 2, 4559 (1970).

88. Y. L. Mankov, Sov. Phys.- Solid State 14, 62 (1972).

89. S. G. Kim, Y. OtanI, K. Fukamichi, and T. Katayama, J. Magn. Magn. Mater. 198-199, 200 (1999).

90. U. Ruediger, J. Yu, A. D. Kent, and S. S. P. Parkin, Phys. Rev. Lett., 80, 5639 (1998).

91. W. F. Egelhoff, Jr., IEEE Trans. Magn. 33, 3580 (1997).

92. T. T. Miyazaki, S. Kumagai, and T. Yaoi, J. Appl. Phys 81, 3753 (1997).

93. R. P. Cowburn, Science 287, 1466 (2000).

94. W. Karr and M. T. Kief, GP-12, MMM conference 2002.

95. J. Grollier, D. Lacour, V. Cros, A. Vaures, and A. Fert, J. Appl. Phys. 92, 4825 (2002).

96. M. Tsoi, R. E. Fontana, and S. S. P. Parlin, Appl. Phys. Lett., 83, 2617 (2003).

97. D. Smith, Thin Film Deposition: Principles and Practice, McGraw-Hill, Inc. 1995

98. Richard C. Jaeger, Introduction to Microelectronic Fabrication, Addison-Wesley, 1998.

99. C. Y. Chang, S. M. Sze, ULSI Technology, pp. 371, McGraw-Hill, 1996.

100. X. A. Cao, et al., Solid-state Electronics 9, 1705 (1998).

101. K. B. Jung, et al., J. of Vacuum Science & Tech A 2, 535(1999).

102. Marc J. Madou, Fundamental of Microfabrication, CRC Press, 1997.

103. W. F. Egelhoff, Jr., Solid State & Mater. Sci. 16, 213 (1990).

104. R. D. Gomez, Exp. Methods in the Phys. Sci. 36, 69 (2001).